Playing Legos with Nanocubes

Harshal Agrawal

Ph. D. Thesis, University of Amsterdam, January 2021
Playing Legos with Nanocubes
Harshal Agrawal

ISBN: 978-94-92323-46-0
Front cover: Cubes assembled in a PDMS template from solution.
Back cover: An optical illusion of cubes arranged in a spiral while they are arranged in a circle.

The work described in this thesis was performed at AMOLF,
Science Park 104, 1098 XG Amsterdam, The Netherlands.

This work is part of the Dutch Research Council (NWO).

A digital version of this thesis is available at:
https://ir.amolf.nl/

Playing Legos with Nanocubes

ACADEMISCH PROEFSCHRIFT

ter verkrijging van de graad van doctor
aan de Universiteit van Amsterdam
op gezag van de Rector Magnificus
prof. dr. ir. K.I.J. Maex
ten overstaan van een door het College voor Promoties ingestelde commissie,
in het openbaar te verdedigen in de Agnietenkapel
op woensdag 27 januari 2021, te 16.00 uur

door

Harshal Agrawal

geboren te Amravati

Promotiecommissie

Promotores:	prof. dr. E. C. Garnett	AMOLF
	prof. dr. A. Polman	Universiteit van Amsterdam
Overige leden:	prof. dr. P. Schall	Universiteit van Amsterdam
	prof. dr. A. van Blaaderen	Universiteit Utrecht
	prof. dr. T. Kraus	Saarland University
	prof. dr. N. F. Shahidzadeh	Universiteit van Amsterdam
	dr. H. Wolf	IBM

Faculteit der Natuurwetenschappen, Wiskunde en Informatica

To all my teachers

CONTENTS

1

INTRODUCTION

"The expert at anything was once a beginner."

-Helen Hayes

1

1.1. Self-assembly

The term "assembly" is commonly used in a variety of fields. For example, it is used in organizations to describe a formal gathering or meeting for a shared purpose and open discussion. In materials science, it relates to bottom-up fabrication. For the discipline of computer programming, it is an adjective for languages. In manufacturing, an assembly line is used to fit together machine parts in a sequential manner to raise a functional (self-contained) unit. In general, assembly conjures up an image of bringing individual entities or components together for diverse objectives.

Self-assembly is the autonomous organization of matter into ordered structures without any external stimulus. The assembly proceeds as a result of local interactions among the system's components [1]; the system puts itself together to evolve into higher-order structures. The shaping of nanocrystals from individual atoms in solution or the formation of self-assembled monolayers on a substrate are two fantastic examples of self-assembly. Self-assembly has made profound contributions to humanity and is still one of the most enthralling concepts in science. It can be observed at all scales ranging from the atomic level to all the way up to planetary-scale [2].

Nature is one of the most skilled, experienced, and best-known users of self-assembly [4–8]. For example, living organisms are by far the greatest, most complex, and sophisticated outcome of self-assembly. Molecules can organize themselves to create cells, which in turn organize at a larger scale to form hierarchical structures. A few other wonders worked with tiny intricate details by the natural master-builder

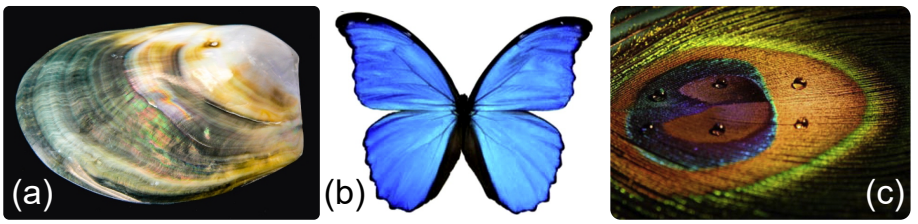

Figure 1.1: (a) Nacre. Image courtesy [3]. (b) The Morpho butterfly and (c) Peacock feather with superhydrophobicity [4].

include nacre – assembly of calcium carbonate (aragonite) platelets in an organic matrix analogous to brick-and-mortar scheme, butterfly wings, and bird feathers [5, 9] as shown in Figure 1.1. Evolution for billions of years has resulted in nearly perfect architectures found in nature. As a result, these multiscale structures flaunt multifunctional properties. For instance, interference of light with thin-film architectures or periodic structures self-assembled into nacre, butterfly wings, peacock feathers, and rose petals [5, 6, 10] give rise to brilliant, iridescent and extremely attractive structural colours. In addition, butterfly wings, peacock feathers, rose petals, lotus leaves, and Gecko feet are also superhydrophobic with self-cleaning properties. At the same time, nacre is notable for its high mechanical strength and toughness despite its light weight [4, 9, 11]. One can also find organisms in nature that showcase dynamic optical properties [6]. For example, Damselfish can change their body surface colour by tuning the guanine nanoplatelet separation in their iridophore as a part of the defense and survival mechanism in their habitat [12]. Needless to say, the earth is replete with many more materials and organisms for admiration.

The aforementioned examples clearly demonstrate the level of expertise and finesse nature possesses over self-assembly. The fascinating properties are a manifestation of micro and nano features cleverly and meticulously integrated over time into the natural three-dimensional (3D) structures [4]. Observing the remarkable properties and effects listed above, scientists undoubtedly want to emulate nature and understand the underlying science. This has given birth to research directions at the interface of various disciplines like materials science, biology, physics, chemistry, optics, and engineering. One strategy to mimic nature and achieve a comparable level of complexity is to use tiny building blocks (colloidal nanocrystals) and find ways to control the accurate placement of these tiny blocks on-demand (bottom-up assembly on a surface) to design synthetic materials with multifunctional properties.

In nanoscience and technology, assembly, especially bottom-up assembly, has proven to be a powerful strategy for making nanostructures and subsequently ensembles of nanostructures [1]. The broad idea of bottom-up fabrication is quite simple. It

is an additive process, analogous to constructing a brick house, that incorporates building blocks (nanocrystals) one by one to shape the desired nanostructure. Thus, the successful execution of the process hinges on being able to synthesize the nanocrystals (with desired size, shape, functionality), assemble them into the desired structure, and bind them together. Below, these three fundamental steps are discussed in more detail.

1.2. Collidal nanocrystal synthesis

Advances in colloidal chemistry have enabled the synthesis of a large variety of nanocrystals from solution [15]. In a typical synthesis, a salt precursor with an appropriate reducing agent reacts to form atomic species in a suitable solvent. These species can further evolve into near-spherical nuclei. A nucleus is nothing but a polyhedral core with a combination of different planes like (100), (111) and has a nearly spherical profile [16]. Nanocrystals are subsequently formed by continuous deposition of atomic species onto the surface of the nuclei [17]. The surface of a nanocrystal roughly contains a few hundred to thousand atoms (Figure 1.2a) and have unsatisfied chemical bonds leading to a high surface energy. Thus, ligands are required which can be thought of as electron donors to the electron-hungry surface of the nanocrystals. These ligands (Figure 1.2b) play a key role by satiating the dangling bonds and bringing the desired stability to the nanocrystal [14, 18]. The size of the

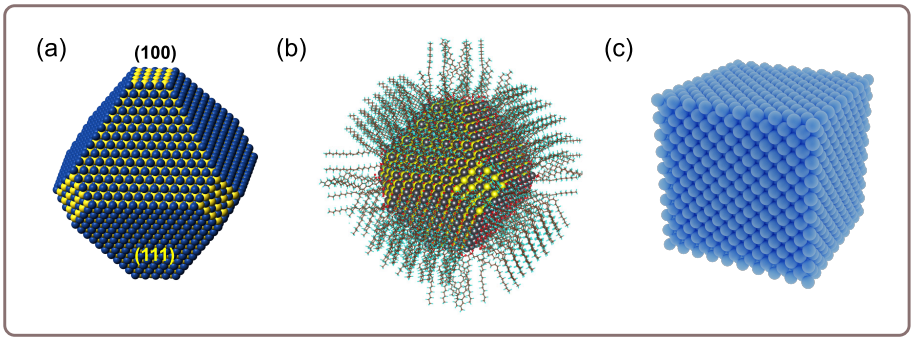

Figure 1.2: Schematic illustrations of a (a) nanocrystal [13], (b) passivated nanocrystal with ligands [14], and (c) nanocube.

crystals can be controlled by the salt precursor and surfactants introduced in solution as well as the reaction time during synthesis [19, 20]. In addition to size, the surface energy of the facets of the nuclei allows for shape control. For example, the free energy of the facets of an ideal face-centered cubic (FCC) nanocrystal, in vacuum, follows the order as {110}>{100}>{111} [17]. The surfactants can selectively adsorb to certain crystallographic domains and reduce the surface energy of the respective facets with respect to others. This in turn, alters the stability hierarchy of the exposed planes (thermodynamics) and growth rate along the different crystallographic axis (kinetics) of the nuclei [21]. This strategy has been used in literature to synthesize nanocrystals with shapes like rods [22], platelets [23], and cubes [24] in solution, as shown in Figure 1.3.

Apart from shape control and post-nucleation passivation of the surface, ligands also shield the crystal from its environment. In other words, they prevent the aggregation or clustering of crystals in solution. Also denoted as surfactants in literature, they help to preserve individual nanocrystals in the solution by providing steric or electrostatic stability [14]. The strength of ligand-nanocrystal binding governs the long-term colloidal stability of the nanocrystals in solution as well as retaining their morphology in various environments.

The “organic armor” around nanocrystals acts as an interface between the

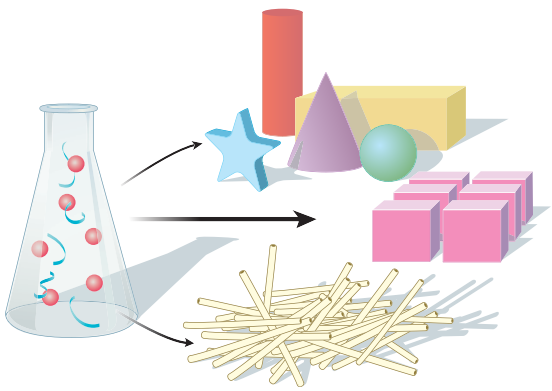

Figure 1.3: Schematic of various shapes of nanocrystals possible by the colloidal synthesis in solution. Image source [20]. Reprinted with permission from AAAS.

nanocrystal and the solvent [25]. It arms the user with the ability to disperse the nanocrystals in a variety of polar solvents like water, ethanol, and dimethylformamide (DMF) or non-polar solvents like toluene, hexane, and chloroform. This provides a handle over the processing of nanocrystals. The ability to tune the wettability of a substrate by changing the solvent enables the deposition of compact films of crystals. It opens a plethora of opportunities for solution processing of nanocrystal based optoelectronic devices [26–28].

The simplest way of integrating nanocrystals into devices is by relying on self-assembled films [1, 29], but even more complex structures can be imagined. The idea of an autonomous organization – the promise of self-assembly – becomes especially appealing when the building blocks fall in the size range of a few nanometers to micrometers. For example, it is easy to assemble machinery when the individual building blocks are big enough to be handheld by humans or positioned with robots in their respective places. However, the same cannot be said for tiny colloidal blocks with dimensions from a few nanometers to microns. These dimensions fall in the size range that can be guided by chemistry [30]. Local interactions between nanocrystals through shape, surface ligands and charge pave the way for ordering (self-organization).

Self-assembly of nanocrystals from solution can lead to aesthetically pleasing ordered domains, as shown in Figure 1.4. Nevertheless, more often than not, the ordering is short-ranged if not controlled precisely [33]. Additionally, large scale tailored complex 2D patterns or 3D architectures are very difficult to fabricate with self-assembly alone. It is reasonable to say that researchers simply do not command the

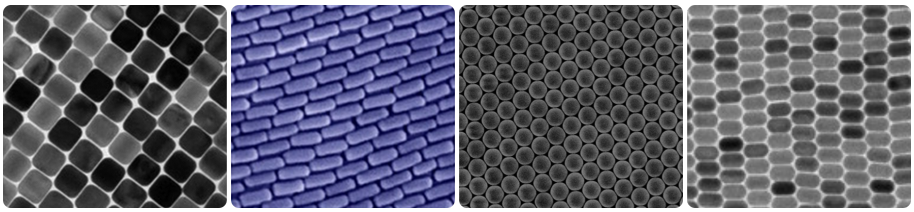

Figure 1.4: Examples of self-assembled nanocrystals from literature [1, 31, 32]. The individual building blocks, i.e. spheres, are 1000 nm in diameter while the rest are less than 100 nm in dimensions.

same level of control over self-assembly as nature. For us, standalone self-assembly strategies are less than reliable and not one hundred percent effective in organizing colloidal particles in the envisioned structural pattern on the surface. However, if there were a way of controlling and guiding the local interactions, it could improve the scenario remarkably.

1.3. Directed-assembly

The fabrication of high-performance optoelectronic devices requires deterministic spatial placement of a wide range of nanocrystals at the micro and nanoscale. The functionalities and capabilities of the devices are governed not only by the optical, electrical, and magnetic properties of crystals but also by their arrangement [34, 35]. While it is reasonably easy to deposit thin films with nanocrystals using techniques like dropcasting, convective assembly, spin coating, doctor blading, dip coating, or Mayer rod coating, it is not straightforward to form user-defined patterned films of nanocrystals. Therefore, it is both a challenge and an opportunity for researchers to design methods to address these individual units and precisely position them at preferred locations with high-resolution.

Directed-assembly is the idea of achieving spatial positioning on the surface with more accurate control via the application of an external force to direct the crystals into intended patterns. Best results are achieved via a combination of both top-down and bottom-up approaches. The envisioned patterns are predefined on a resist layer (commonly polymethylmethacrylate (PMMA)) coated on a substrate via top-down lithography (predominantly electron beam lithography (EBL)). Depending on the application, the patterns can be retained in the resist or transferred to the substrate or a template. Polydimethylsiloxane (PDMS) is a famous material for casting flexible and reusable templates [36]. Patterning is a synergistic effect of the directing force and the confinement imposed by the topographic patterns on the template. Some necessary attributes of the external force are: (a) It must be strong enough to overcome the Brownian motion of particles, particle-substrate as well as particle-particle interactions. (b)

It must be possible to produce substantial contrast of the directing force, sometimes from negligible to a maximum, from the surface of the template to the bottom of the wells of patterns in the template. The choice of the directing force will determine the assembly method.

One of the most studied forces for directed assembly is the capillary force [37]. The working principle is highlighted in Figure 1.5. A drop of colloidal solvent is dragged onto a patterned PMMA or PDMS template. During this process, the colloidal particles experience a capillary force exerted from the solvent. When the particles encounter a topographic depression on the template, they are trapped in the template by the virtue of the vertical component of the capillary force and the geometrical confinement. Excellent work has been reported for 60 nm Au particles, 100 nm Ag particles, and 110 nm Au nanorods and in a few cases with almost 100% assembly yield [38–40]. It has been successfully applied to orient particles on a substrate and also to fabricate samples suitable for plasmonics [41, 42]; however, it comes with stringent tolerances. Clean filling of the template is achieved with a narrow window of 40° - 45° contact angle which makes the choice of the solvent and the template very critical. Several reports illustrate the use of water as solvent and PDMS as the template, but, hardly any exist with the use of non-polar solvent for capillary assembly

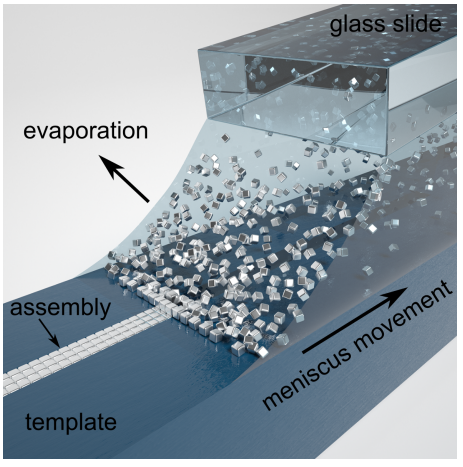

Figure 1.5: Schematic illustrating the concept of capillary assembly.

because of the swelling problem [43]. Careful processing to make the nanoparticle stock is required to ensure the right interfacial tension for reproducible results as residual surfactants after synthesis can alter the surface tension of the solvent. Also, the contact line pinning is a major concern in this process. Any topographical inhomogeneity on the template surface will disturb the receding three-phase contact line, and the problem is exacerbated if there are impurities on the surface or air currents in the atmosphere. It is vital to work in a clean and regulated atmosphere to achieve well-controlled dewetting. Lastly, the typical drag speeds used are 1-100 $\mu m.s^{-1}$, so scaling up with high-throughput is a challenge.

Apart from capillary force, the electrostatic force has been studied for quite some time now. The law of electrostatic charges states that opposite charges attract each other. Hence, it is only logical to assume that researchers must have tried to exploit this force to pattern charged particles. The idea is to pattern electrostatic charges on a substrate and then print the oppositely charged particles to bring the patterns to life (Figure 1.6a). Local surface charge contrast can be created on insulating substrates including PMMA, sapphire crystals, SiO_2 layer on Si, and polytetrafluoroethylene (PTFE) via a conducting atomic force microscopy (AFM) tip [45, 46] or soft imprint lithography [47]. 290 nm silica beads have been patterned on a PTFE film by dumping surface charges with voltage pulses applied to an AFM probe [48]. Charge contrast can also be achieved by first patterning resist by EBL and then planting silanes in the patterned areas to attract the particles. For example, 70 nm Au and Ag nanospheres functionalized

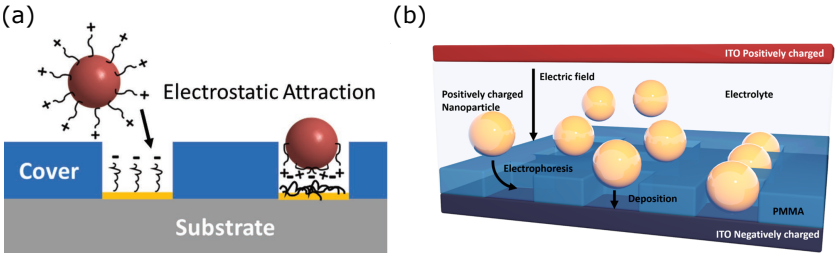

Figure 1.6: Schematic illustrating the concept of (a) electrostatic [35] and (b) electrophoretic assembly. Reprinted (b) with permission from [44]. Copyright 2018, American Chemical Society.

with negatively charged bis(p-sulfonatophenyl)phenylphosphine (BSPP) or tris(2- carboxyethyl)phosphine (TCEP; 2 mM) were captured on a template grafted with an amine-terminated silane (N-[3-(Trimethoxysilyl)propyl]ethylenediamine) [49]. Defined periodic nanoparticle cluster arrays were fabricated using citrate stabilized 40 nm Au particles, which exhibited multiscale enhancement of the Raman signal [50]. Another variation of the process uses electric fields to direct the particles in traps and is commonly known as electrophoretic deposition (EPD, see Figure 1.6b). Under the influence of the applied electric field generated by 3 V DC bias between two conducting electrodes, 110 nm Au spheres and 100 nm by 40 nm rods were printed on a PMMA-ITO electrode in an aqueous electrolyte with single-particle resolution [44]. It is even possible to obtain ordered colloid monolayers by EPD [51]. However, these methods require numerous steps for patterning, particles must be charged, and the surface charge has to be patterned on substrates with high accuracy. Additionally, the technique requires a high volume of nanoparticle ink and is sensitive to the choice of solvent, pH, salt concentration, applied potential and sometimes requires high voltages (+70 V [52]).

Guiding particles by creating a chemical contrast on a substrate instead of charge contrast is also very promising. Thus, using chemical distinction to pin down particles on-demand in desired patterns via specialized functionalization like DNA [53–57],

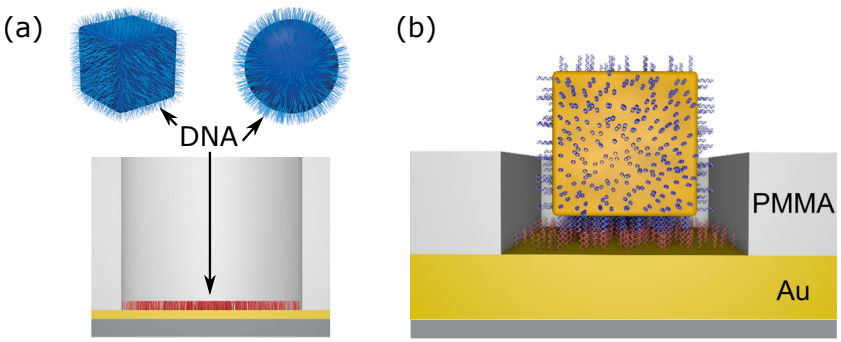

Figure 1.7: (a) DNA functionalized nanoparticles and the template with conjugate pairs. (b) Nanocube attached to the template via DNA binding. Image source [53, 54].

thiolated monolayers or other organic molecules is explored extensively [58, 59]. The idea, for example, is to functionalize the nanocrystal with DNA and the lithographically defined areas (with EBL, dip-pen lithography [60] or microcontact printing [61]) on the template with the complementary strands of DNA which act as binding sites for the particles (Figure 1.7). 3D superlattices of nanoplates, cubes, and spheres had been demonstrated with DNA engineering [54]. This strategy involves higher costs of synthesis, multiple steps, requires long (12-24 hour) time, and needs extensive work to apply to various materials.

Patterning without defining specific pinning sites (via topography, charge, or chemical difference) on a substrate, unlike described in the preceding text, has also been demonstrated. The idea is termed optical printing, as shown in Figure 1.8. It utilizes optical force (from a tightly focused laser) and van der Waals interaction to capture and incorporate colloidal particles on a substrate [63]. The substrate is functionalized with the same sign (positive or negative) of charge as the particles to trigger electrostatic repulsion and prevent unwanted deposition of particles. The optical force from the laser directs the particle to the substrate. When the particle is close enough to the substrate, van der Waals forces dominate over electrostatic repulsion and irreversibly trap the particle on the substrate. The application of optical force has been demonstrated to fabricate custom patterns and lattices of 80 nm Au

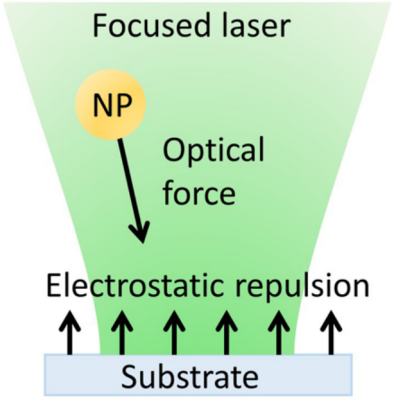

Figure 1.8: Schematic illustrating the idea of optical printing. Image source [62].

particles capped with CTAB or 60 nm Au and Ag particles capped with citrate [62, 64]. The method has much potential as it can print patterns without the need for a mask and on almost any substrate. Going in the direction of scaling-up with high throughput can be very promising. It is a serial printing technique which requires careful selection and manipulation of optics as well as laser and the substrate should bear the same sign of charge as the colloidal particles.

Most of the techniques described above are restricted in terms of resolution or scalability, involve multiple complicated steps, long processing times or work only with a narrow range of materials. An ideal directed-assembly technique should be easy to implement, scalable, fast, offer no deposition of particles outside the targeted patterns (negligible residual layer), and have general applicability for (all) materials. With this aim in mind, the thesis reintroduces imprint lithography, but, with the capability of direct on-chip patterning of colloidal particles, control over positioning (comparable to top-down), that also works independent of the particle capping ligands. The technique can print micro and nanostructured designs in arbitrary patterns and on a large scale in a single step. Overall, it has immense potential to succeed as a generic and low-cost approach for fabricating patterned thin-films of colloidal crystals and subsequently optoelectronic devices.

1.4. Epitaxy

While assembled nanocrystals can be readily used in optical applications, sometimes it is highly desirable to connect the adjacent nanocrystals (epitaxy/welding), especially for solid-state devices that require high electrical conductivity [14, 65]. The organic ligands at the interface of nanoparticles inhibit the formation of a continuous percolation pathway for electrons from one end to the other of the assembled crystals [66]. Thus, plasma or solution dissolution techniques are used to eliminate the ligands [67, 68]. The absence of ligands leaves a free space of a few nanometers between nanocrystals. One way to bridge the individual entities into a continuous crystal and decrease the contact resistance is to locally rearrange the atoms (diffusion) via

thermal, plasma, optical activation, or mechanical pressing [66, 67, 69–71]. This can yield connected networks but, at the same time can cause strain, void formation, or shrinkage of materials. If not controlled properly, it can also lead to evaporation or recrystallization of material with partial loss of patterning [72, 73]. Another way would be to locally deposit extra material in the nanogaps [74, 75]. This opens up the exciting possibility of making patterned epitaxial films or epitaxial core-shell superstructures.

The term 'epitaxy' refers to a type of growth mode of crystals. In epitaxial growth, new (single) crystalline material is deposited onto a monocrystalline substrate or seed. The crystallographic orientation of atoms forming the epitaxial layers of the growing crystal is governed by the exposed facets on the surface of the underlying substrate. If the growing crystal and substrate are of the same material, it is classified as 'homoepitaxy'. In this case, the atoms in the nucleated layers extend the registry of the seed atoms along the growth direction. If the growing crystal is of a different material than the guiding substrate, it is classified as 'heteroepitaxy', as shown in Figure 1.9.

The lattice mismatch between the growing and guiding material is a crucial parameter for selecting candidates for epitaxy. Good agreement among lattice constants is highly desirable to minimize the interfacial stress and subsequent formation of dislocations. When the fresh material starts to grow on the underlying substrate, the lattice mismatch will lead to some residual strain at the epitaxial interface. The lattice

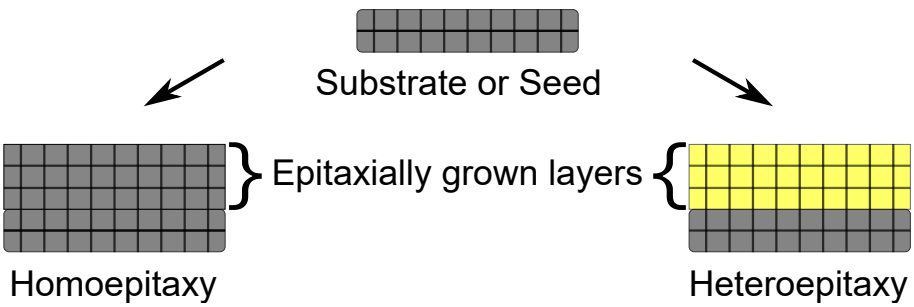

Figure 1.9: Schematic illustration of homo and heteroepitaxy.

misfit strain energy builds up with the increasing layer thickness. The strain alters the material's lattice and hence the crystal and electronic structure, which, in fact, can be utilized to engineer beneficial functional properties. For example, enhancing the carrier mobility in strained channels of Si and Ge or bandgap modulation of ZnO nanowires [76, 77]. However, beyond a critical layer thickness, the strain energy is released by nucleating a structural defect in the form of dislocations at the interface [78, 79].

Dislocations serve as active nonradiative recombination sites for charge carriers and can lead to lower photoluminescence intensity [80, 81]. They also reduce the carrier mobility, yield and lifetime of the devices as well as can cause leakage current pathways in light-emitting diodes (LEDs), laser diodes, and photodetectors [82–84]. Another study indicates that large dislocation density (>10^8 cm^{-2}) can rapidly reduce the thermoelectric figure of merit, for example, in the Si/SiGe system. It happens because of a sharp decrease in electrical conductivity with an increase in the number of dislocations [79]. While strain engineering can be employed toward one's advantage, the resulting dislocations from the strain relaxation can prove detrimental to the device performance. Crystal growth and defects are like two sides of the same coin. While post-growth high-temperature annealing can be a means to reduce dislocation density (defects) [85], scientists are always researching ways to grow superior materials with inherently low imperfections.

Epitaxial growth of materials finds applications in nanotechnology to fabricate high-quality crystals. Conventional growth techniques are molecular beam epitaxy, chemical vapor deposition or Czochralski method. In these techniques, growth is achieved by deposition of highly pure gaseous precursor or crystallization from the hot melt on a pre-existing monocrystalline guiding substrate. Additionally, they are slow as well as expensive. Recently, the formation of epitaxial films only by spin coating has been demonstrated [86]. Much literature also exists for local nanocrystal epitaxy (core-shell growth of free particles in solution). It includes both homoepitaxy and heteroepitaxy [87, 88]. Homoepitaxy involves first making nanocrystal seeds and

then doing overgrowth to make them larger or change their shape [16, 89]. Heteroepitaxy involves growing hybrids of metals, semiconductors, or dielectrics, e.g., metal-semiconductor heterojunctions [87]. Control down to almost single monolayer has been reached in certain systems. This could be a cheaper alternative, even then, all these processes are heavily dependent on the underlying substrate or seed and offer limited scope for patterned growth of epitaxial films.

1.5. Coda: Nanocube assembly and epitaxy

Monocrystalline materials are the key building blocks to reach the ultimate performance in a host of applications including solar cells and LEDs. The fundamental approach to crystal growth has not changed in 100 years: one starts with a monocrystalline seed or a monocrystalline substrate (with the same crystal lattice parameter), then grows epitaxial layers from this single nucleation center to obtain an ingot or a thin film. Given that, there is hardly any technique that allows bottom-up patterning (rather than etching) and is simple to implement as well as inexpensive to grow high-quality materials (smooth surface and without grain boundaries).

The last few decades have witnessed great feats in the synthesis of core-shell colloidal nanocrystals from solution. These (hybrid) particles are made via depositing an epitaxial shell, hetero [88] or homo [90], around the pre-synthesized core in solution. Amongst the various reported morphologies - sphere, rod, sheet, and wire [88], in the premise of this thesis, the simple cubic shape is particularly interesting. It has six crystallographically well defined and chemically equivalent faces (Figure 1.10-a,b). As a result, the inception of an entirely new substrate-independent strategy is possible that builds monocrystalline materials from many single-crystalline nanocubes [75]. Solution synthesized nanocubes have atomically flat faces, which is imperative and appealing as they serve a threefold purpose. First, they can enable void-free and complex structures via directed assembly. Second, the flat surfaces offer the desired stability to build robust 3D geometries. Third, they play a pivotal role in connecting these individual nanoscale building blocks into future functional devices:

1

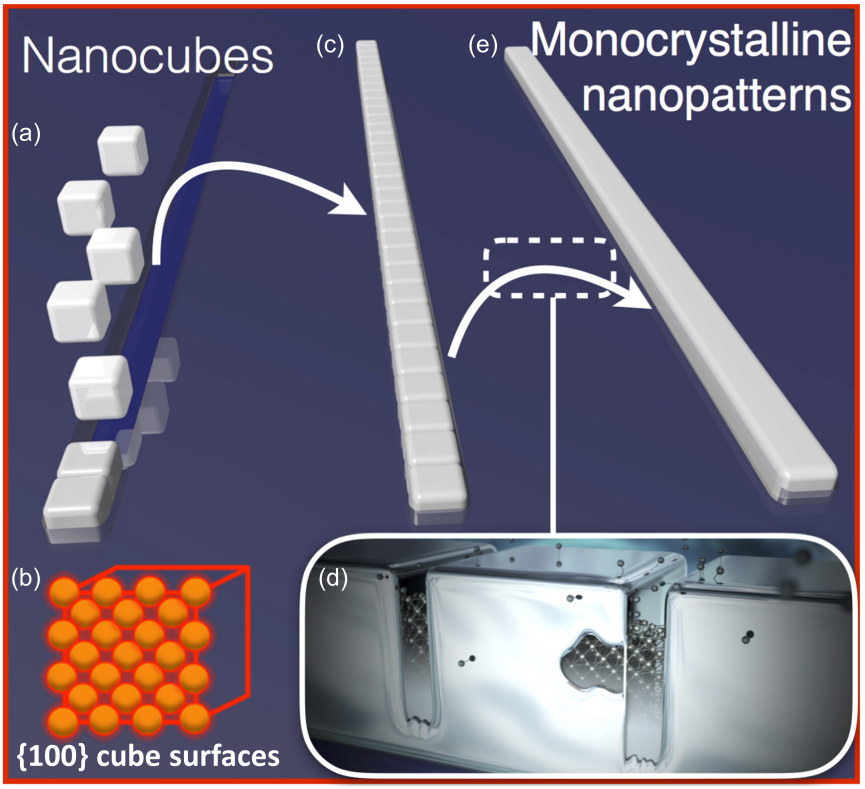

Figure 1.10: Many nanocube seeds, aligned crystallographically, connected epitaxially. Image source [75].

after aligning cubes along a same crystallographic axis (Figure 1.10c), six similar faces will ensure that the (100) face of one cube is always sitting against the (100) of another cube. This geometry enables the right crystallographic orientation for epitaxial overgrowth (Figure 1.10d). Thus, directed assembly of nanocubes and subsequent epitaxial overgrowth paves the way for patterned monocrystalline materials (Figure 1.10e) without the requirement for a lattice-matched substrate. Moreover, it has the potential to enable devices constructed exclusively from solution and at low temperature. In conclusion, as the nanocube synthesis has already been reported for many different metals, semiconductors and insulators, the preceding extraordinarily simple and novel approach for epitaxy drastically expands the list of materials that

can be grown as monocrystalline 1D, 2D or even 3D optoelectronic devices.

1.6. Outline of the thesis

In chapter 2 [91], highly reproducible, nanoimprint lithography using a film of monocrystalline 75 nm Ag cubes as the resist and PDMS as the stamp to directly form the final pattern is discussed. By re-wetting the resist layer with solvent and subsequent imprinting with a patterned stamp, it is possible to produce patterns such as straight lines, curves and complex junctions over an area of several square millimeters with a width of only a few nanocubes (even single-particle width) with high accuracy and contrast. It has been demonstrated that – for the used Ag nanocubes and patterns – only very few particles are left in the areas between patterns. It is also possible to print three-dimensional (3D) nanopatterns with an aspect ratio up to 5 in the vertical direction. The concept developed using Ag cubes as a model system also works for other materials with different shapes, sizes, and surface capping.

In chapter 3 [92], we interrogate the quality of the interface formed after connecting a pair of assembled nanocubes. Dropcast 7 nm Pd cubes capped with PVP are treated with aqueous $NaBH_4$ solution, where the cubes travel several microns on the substrate to form epitaxial connections. It is demonstrated that it is possible to make dislocation- and strain-free single crystals by nanocube assembly and epitaxy in cases where perfect angular alignment is achieved. Notably, aberration-corrected high-resolution STEM was used to give a clear picture of dislocations formed in the Pd nanodimers and identify the effects of lateral and angular misorientations on the formation of dislocations and strain.

In chapter 4, monocrystalline aligned cubes in different patterns are overgrown in solution to make connected larger crystals. We make curved crystals by homoepitaxial growth of Ag or heteroepitaxial growth of Au down to a radius of curvature of 300 nm. AFM and energy-dispersive spectroscopy are used to characterize the curves. Local overgrowth of Ag is also performed on the bidirectional assembly of Ag cubes in lines to convert into connected networks of nanowires. It is further proved that

these crystals can be used as optically transparent conductors. The chapter also offers teasers for nanocube assembly and overgrowth in terms of fundamental and practical opportunities in nanotechnology.

In chapter 5 [93], the concept of ligand exchange is applied to tune the assembly of nanocubes. High-quality self-assembly of luminescent 10 nm $CsPbBr_3$ perovskite nanocubes into close-packed monolayers via controlled evaporation is reported. It is achieved by partially replacing long-chain oleyl groups (18 carbon chain) with a shorter thiocyanate (SCN^-) moiety. SEM and AFM images show the formation of monolayer thin films with RMS roughness of 4 Å. The monolayer films could also act as seed layers to create halide perovskite single-crystalline thin films for better performance in optoelectronic devices [94, 95].

2

NANOCUBE IMPRINT LITHOGRAPHY

In recent years, imprint lithography has emerged as a promising patterning technique capable of high-speed and volume production. In this work, we report highly reproducible one-step printing of metal nanocubes. A dried film of monocrystalline silver cubes serves as the resist and a soft polydimethylsiloxane (PDMS) stamp directly imprints the final pattern. The use of atomically smooth and sharp faceted nanocubes facilitates the printing of high-resolution and well-defined patterns with face-to-face alignment between adjacent cubes. It also permits digital control over the linewidth of patterns such as straight lines, curves and complex junctions over an area of several square millimeters. Single-particle lattices as well as three-dimensional (3D) nanopatterns are also demonstrated with an aspect ratio up to 5 in the vertical direction. The high fidelity nanocube patterning combined with the previously demonstrated epitaxial overgrowth can enable curved (single) crystals from solution at room temperature or highly efficient transparent conductors.

2.1. Introduction

Micro and nanolithography have been employed for decades to realize patterned electronic and photonic devices [26, 96, 97]. Electron beam lithography (EBL) provides excellent fidelity and precise positioning on the substrate, however, it is expensive, with multiple steps, and scalability is a major deterring factor. Successive etching steps used for pattern transfer can also roughen the surface and degrade the material quality by introducing defects. Other patterning techniques have been developed to avoid the etching step including micro-contact printing [58, 61, 98], dip-pen lithography [60], inkjet printing [99], scanning probe lithography [100, 101], and template-directed assembly [37–39], but these all suffer from either problems with resolution or scalability. Imprint lithography has the potential to simultaneously deliver surface patterning with sub 10 nm feature size while delivering high-throughput over large areas [102–110]. Additionally, it is relatively cheap, material-efficient, free of vacuum-based high-end equipment, and holds the promise of bringing patterned 3D nano-architectures to life [111–114].

Soft imprint lithography utilizes an elastomeric stamp having trenches or ridges in the desired dimensions and shape for pattern transfer to the underlying film [36, 112, 115, 116]. This simple yet powerful embossing concept has enabled efficient plasmonic back-reflectors for solar cells [117], periodic arrays as antireflection coating [118], template confined growth of crystals [119, 120], surface-enhanced Raman spectroscopy substrates [121], transparent conductors [122–125], nanobatteries [114], and other nanoelectronic devices like organic field-effect transistors [126]. Polycrystalline spherical nanoparticles of Ag, Au, TiO_2 and indium tin oxide (ITO) have been used as the ink for patterning and are subsequently sintered at high temperatures to form a crystal [114]. The thermal fusing step combined with the gaps inherent in close-packed spheres can lead to porosity, shrinkage and even cracking. The sintering temperatures are also often high (450 °C) [114, 117, 127, 128], which is still an impeding factor for true integration of imprint lithography of nanoparticle-based devices on heat-sensitive flexible polymeric substrates essential for high-throughput roll to roll

processing.

In this chapter, we show the printing of complex nanopatterns using monocrystalline Ag nanocubes capped with polyvinylpyrrolidone (PVP) directly as an imprint resist. The use of atomically smooth and single-crystalline nanocubes as ink facilitates alignment between adjacent particles and enables high-precision patterns with a smooth surface as well as sharp, well-defined edges and essentially no void space. PDMS is used as the stamp to pattern and print the cubes over an area of up to a few mm^2, which is only limited by the setup used. The technique proposed is highly reproducible and enables directed assembly of colloidal particles in profiles like curves and lines on rigid as well as flexible substrates. We show that it is possible to control the line width of patterns with digital accuracy (1, 2, 3,..., *n* particles wide) and print patterns with an aspect ratio up to 5 in the vertical direction. The patterning is largely independent of the material properties of the nanocubes and thus broadly applicable to a variety of materials. Finally, the crystallographic alignment inherent to nanocube assembly combined with the patterning demonstrated here is promising for printing strain- and dislocation-free single crystals with arbitrary nanopatterns at room temperature [75, 92].

2.2. Results and discussion

The process flow of nanocube imprint lithography is illustrated in Figure 2.1. The process requires 3 key components. First is the substrate on which the pattern needs to be printed. It can be any rigid material like silicon (Si), glass, quartz or any flexible material like cellulose acetate (projector transparency), polyimide film (Kapton tape) or a polyethylene terephthalate (PET) foil. Second is the nanocube ink of the desired material dispersed in a solvent. Colloidal nanocube synthesis has been reported in the literature for a variety of materials. For example, in the class of metals - Ag, Au, Cu, Ni, Pd, Pt, Rh [129–133]; semiconductors – PbS, Cu_2O, FeS_2, Fe_2O_3, $CsPbBr_3$, $CsPbI_3$, $CsPbCl_3$ [134–138]; and dielectrics – $BiFeO_3$, $SrTiO_3$, CeO_2 [139–142]. We have used Ag nanocubes with an edge length of 75 nm and dispersed in ethanol as the

colloidal ink, as shown in Figure 2.5. The third component is an elastomeric stamp (also called a template) which has the desired patterns in the form of nanotrenches. These trenches are made by casting the polymer on the Si master (Figures 2.6 and 2.7) which has the inverse pattern made by EBL and plasma etching (refer to supporting information for the fabrication details of the master and the stamp). The PDMS stamps (Figure 2.8) have trenches forming different patterns: circles with various radius of curvature, gratings and grids, all with various linewidth, pitch and depth (see table 2.1 for all parameters).

In a typical imprinting process, the surface of the substrate (Si, Figure 2.9) is first activated with UV-Ozone treatment to ensure even wetting over the entire substrate surface. Then nanocube ink (Ag nanocubes dispersed in ethanol) is dispensed onto the substrate at room temperature. The solvent is allowed to dry completely leaving a film of nanocubes which is referred to as a nanocube resist (Figure 2.10). Subsequently, pure solvent (ethanol) is dispensed onto the same spot over the dried film of cubes and before the solvent evaporates, the elastomeric stamp is pressed onto the substrate. The temperature of the substrate is raised to 40 °C and held for 20 min to ensure complete solvent evaporation. Lastly, the stamp is withdrawn with a motorized control (200 µm/min). This leaves behind nanocube patterns on the substrate. The setup used for the nanocube imprint lithography is shown in Figure 2.11.

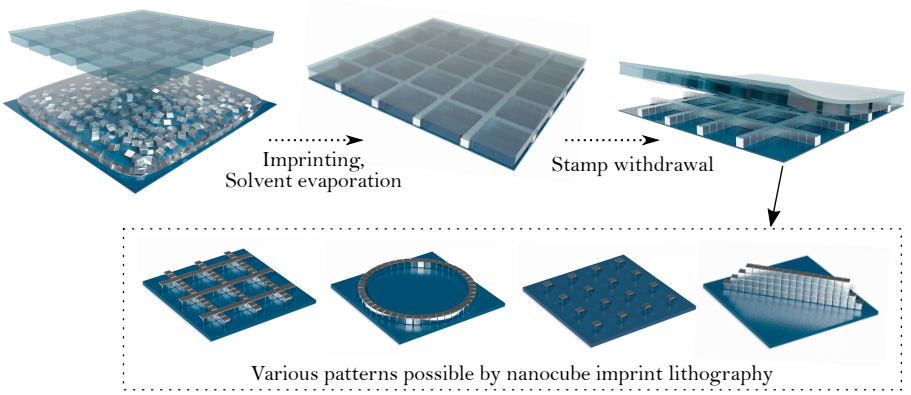

Figure 2.1: Schematic of the imprint lithography process.

The complete drying to form a nanocube resist layer followed by rewetting with pure solvent was found to be essential for reproducible, high-fidelity patterning. Direct printing of the colloidal solution before drying led to highly non-uniform patterns, with many trenches missing particles even when very high colloidal concentrations were used (Figure 2.12). On the other hand, imprinting on the dry nanocube resist (without rewetting) led to many particles remaining on the substrate in areas outside the targetted pattern (Figure 2.13). It therefore appears that the drying step binds the particles to the substrate in order to drastically increase the effective concentration, while the addition of solvent afterwards allows for lateral mobility on the substrate surface without complete redispersion. PDMS is known to be permeable to a variety of solvents including ethanol and hence the solvent can evaporate through PDMS during the heating step [43]. Excess cubes stuck to the surface of the stamp after printing can be easily removed by a piece of office tape. Alternatively, the cubes can also be retrieved and reused by ultrasonicating the stamp for 5 min in the very same solvent in which the cubes were dispersed. After these steps, the stamp is very clean and can be reused. It is critical to make highly uniform stamps in terms of thickness. Uniform thickness ensures even distribution of pressure on the entire area and in turn high quality of the printed patterns.

Figure 2.2 shows a variety of nanopatterns formed using the imprinting process with a Ag nanocube resist. We can direct the cubes from the disordered state in the resist (Figure 2.10) to assembled curved profiles with nearly full circles and almost perfect face to face stacking along the circumference as shown in Figure 2.2-a,b. It is also possible to print curves with different radius of curvature (ϕ). We were able to print curves with ϕ = 4 μm, all the way down to 300 nm, as shown in Figure 2.2-a,b and 2.14-a,b,c,d. Additionally, it is possible to control the linewidth of the printed patterns with digital accuracy, for example, from 1 to 4 cubes as shown in Figure 2.2-c,d,e,f. The number of cubes forming the width of the patterns can be simply controlled by tuning the trench width in the PDMS stamp. We also observed that even for the same trench width, different printed linewidths could be obtained by

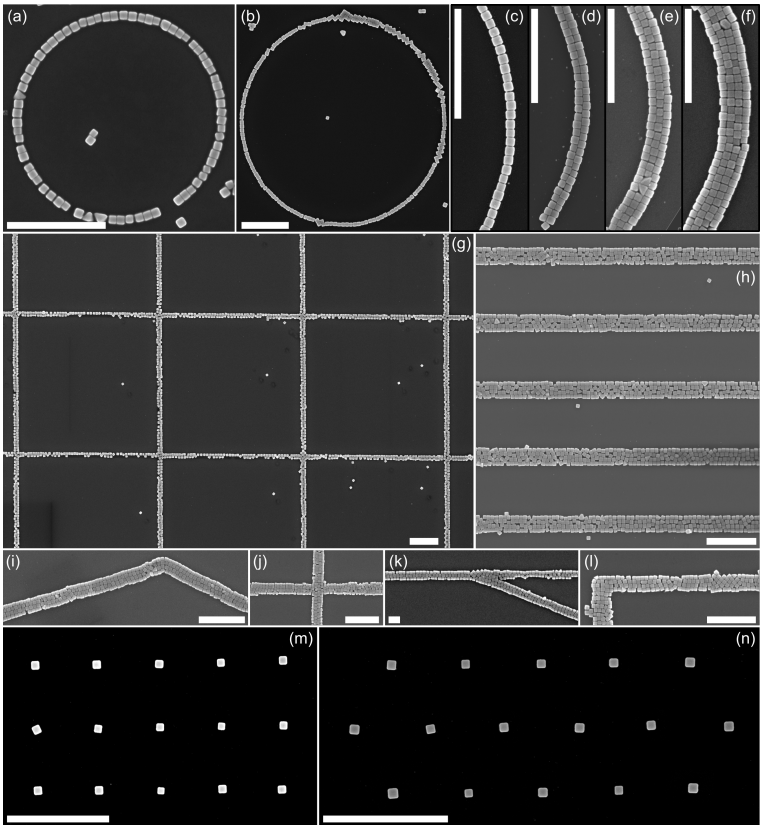

Figure 2.2: A variety of printed patterns of Ag nanocubes demonstrating the potential of the imprinting process. (a-b) Circles of 1 μm and 2 μm radii of curvature respectively. (c-f) Arcs of 2 μm radius of curvature with a line width of 1, 2, 3, and 4 cubes respectively. (g) Cubes printed in a grid pattern with a pitch of 5 μm. (h) Gratings of cubes with a pitch of 1.4 μm. (i) An acute angle turn. (j) A 4-way junction. (k) A 3-way junction. (l) Sharp 90° turn (corner). (m) Cubic and (n) hexagonal superlattices of Ag cubes. All scale bars are 1 μm in length.

adjusting the applied pressure, although this was not explored systematically. Apart from curved profiles, it is also possible to print straight lines with this technique, for example, grids and gratings as shown in Figure 2.2-g,h and 2.14-e,f. In order to print assemblies of arbitrary 2D patterns, along with curves and lines, it is equally important to be able to print complex nodes and junctions. For demonstration, we have printed 2-way, 4-way, and 3-way junctions as well as a sharp 90° turn as shown in Figure 2.2-i,j,k,l respectively (more examples in Figure 2.15). Finally, arrays of

isolated nanocubes were printed with good orientational alignment (Figure 2.2-m,n), which can be interesting for applications using surface lattice resonances [40, 143].

The residual number of cubes in and around the desired patterns shown in Figure 2.2 and the corresponding supporting figures is really low. This is a significant result given that we have a few hundred million cubes (2.1 x 10^{11} cubes/mL for Ag nanocubes) to begin with at the resist stage before patterning. Such clean printing (98.7% of nanocubes in the desired pattern) is possible because of two main reasons: First, a thin layer of solvent is present during printing which provides sufficient in-plane motion for the cubes. Second, the flexible nature of the PDMS permits conformal and complete flat contact with the underlying substrate pushing the excess cubes into the trenches [112].

Nanocube imprint lithography can be easily implemented on a large scale. We have successfully printed patterns like arrays of circles, gratings, and grids in areas on the order of mm^2 on a Si substrate as shown in Figure 2.3 and Figure 2.16. The printing area in this work is limited to mm^2 only because of the Si master that was used to make the PDMS template. In principle, the process should be able to yield patterns at the wafer-scale or beyond in a single print. The inset of Figure 2.3c shows the Si substrate from which the optical image was acquired. The uniform bright colors arising from diffraction over the 2 mm^2 square confirms the presence of the printed grid over the entire printed area.

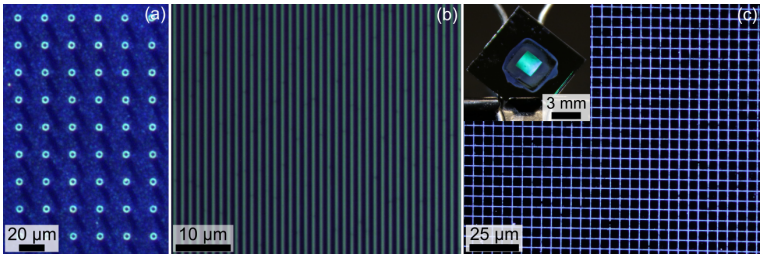

Figure 2.3: Potential for large scale imprinting. (a) Optical micrograph of arrays of circles of Ag cubes. (b) Optical micrograph of gratings of commercially available 50 nm silica spheres. (c) Optical image of the printed grid of Ag nanocubes. The inset depicts the Si substrate from which the optical image was taken and the center of the substrate is reflecting the bright colors because of the diffraction of light due to the printed grid.

The Ag nanocube ink contains excess PVP to preserve the colloidal stability of the particles. During the drying step, as the solvent evaporates, this excess PVP concentrates and packs around the cubes. After drying, it is retained on the substrate along with the cubes forming a fairly even film (resist) owing to surface activation of the substrate. The Ag nanocube resist is essentially a composite of Ag cubes embedded in the matrix of PVP. The PVP cushion prevents the irreversible binding of the cubes to the substrate irrespective of the high surface energy of the substrate. This is the key to nanocube imprint lithography. The thin layer of solvent (ethanol) available due to rewetting can partially redisperse the PVP to allow for enhanced surface mobility. For rewetting, it is critical to choose a solvent that is good for PVP. For example, we rewetted the resist layer with dimethylformamide (DMF) which is another excellent solvent for PVP and it also led to good patterning results (Figure 2.17-a,b). In contrast, rewetting with a bad solvent for PVP like toluene or hexane didn't lead to any patterning (Figure 2.17-c,d and e,f respectively). Thus, during stamping, the viscous drag provided by the PVP/good solvent duo can move the cubes over substantial distances. Our results suggest that the Ag cubes can travel at least 10 μm (see diagonally located circles of Figure 2.16-d,e) and even up to 25 μm (Figure 2.15e) in some cases.

Fundamentally, the patterning and packing are both governed by the confinement that is imposed by the trenches carved in PDMS. Patterning is the direct result of nanoparticles being driven to the trenches while pressing the stamp on the substrate and the density of particles along with interparticle attraction determines the packing. The temporary binding and release of particles from the substrate as well as the displacement of particles on the substrate is facilitated by the PVP/ethanol combination (component forming the matrix and solvent compatible with it). Thus, if the native ink solution doesn't contain PVP, patterning can still be achieved by adsorbing a layer of PVP on the substrate before dispensing the desired nanoparticle ink. As a result, the process is not restricted to metallic Ag or cubic shape only. It can also nicely print other classes of materials as well as nanoparticles with different shapes, sizes, surface

ligand capping and dispersed in various solvents. For example, the gratings shown in the optical image of Figure 2.3b and Figure 2.18 were printed with commercially available 50 nm silica spheres. The areas outside the lines are exceptionally clean with no residual layer. The spheres were originally dispersed in ethanol with silanol as the surface functional group. Before dropping the ink, the substrate was adsorbed with 2 μL of 1 mM PVP in ethanol and allowed to dry completely. We also tried 0.5, 1, 2, and 4 μL of PVP solution with constant area of the substrate and beyond 1 μL there was no perceivable difference in the printing results. The technique was also tested with other materials including 100 nm polystyrene spheres with carboxylate capping, 50 nm Au cubes with citrate capping and 20 nm Pd cubes with PVP capping. The results are shown in Figure 2.19 and it proves that the concept of nanocube imprint lithography can be translated to colloidal inks with different materials, shapes, sizes and surface chemistry. Since the technique requires very little ink (few μL per print), it makes the process efficient and economical from a technological standpoint, while the broad applicability is appealing for the field of nanopatterning.

Another interesting aspect of imprint lithography explored in this work was the ability to print high aspect ratio shapes. We were able to print curves and lines of a

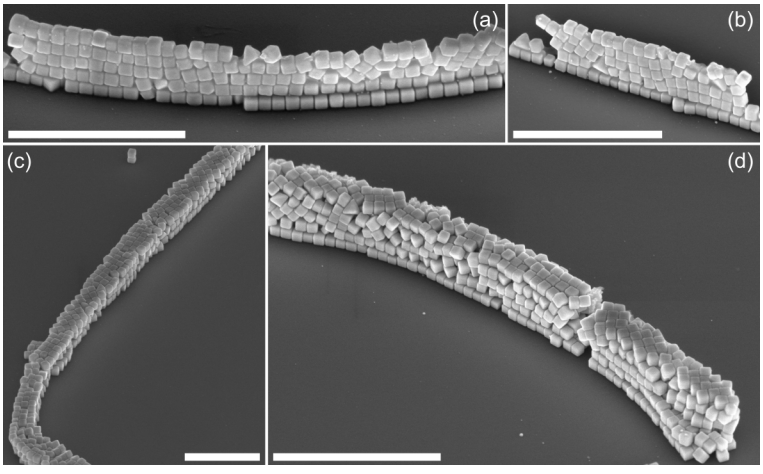

Figure 2.4: Patterns, (a) curve and (b) line, with a maximum aspect ratio 5 in the z-direction. (c), (d) are the 3D patterns assembled out of Ag cubes. All scale bars are 1 μm in length.

maximum aspect ratio 5 as shown in Figure 2.4-a,b and Figure 2.20. The cubes are nicely sitting on top of each other and glued together with the interparticle force of attraction. The flat faces of the cubes lend the desired stability and allow for printing of single-particle wide yet 5 cubes tall free-standing walls. Such high aspect ratios are nearly impossible to attain with spherical or irregular particles which is the most common shape found in colloidal inks. A previous report showed excellent layer-by-layer assembled 3 particle tall superlattices, however, it was achieved with top-down lithography on a specially engineered substrate using nanocrystals and DNA [54]. As with the 2D patterns, the packing among the cubes in 3D is reasonably good, except where an irregular shaped particle disturbs the flow. However, the process appears to be tolerant of particles of different shapes and sizes, for example, a tetrahedron appears in the 2^{nd} row from the bottom in both the patterns in Figure 2.4-a,b but the packing as a whole is robust (also see Figure 2.2-a,e,f). The digital linewidth control seen with 2D patterns also can be extended to 3D patterns, as shown in Figure 2.4-c,d. Finally, the pattern quality can almost certainly be improved with further optimization of the imprinting press and process parameters.

2.3. Conclusions

We present a facile and reproducible technique that can print structures with nanoscale spatial resolution over large areas in a single step using nanocubes directly as an imprint resist. The technique was successfully applied to colloidally stable Ag nanocubes to print high-resolution curves, lines, grids and complex junctions. We have also demonstrated single particle lattices as well as 3D patterning, with tall patterns showing an aspect ratio up to 5, along with digital control over the linewidth. The topographically patterned PDMS stamps can be reused multiple times and elastic nature of the material facilitates clean printing of the patterns. Imprint lithography is a physical process and we have demonstrated that it can be applied to a variety of materials, particles of different shapes and sizes thus broadening the scope of the process. Additionally, it is inexpensive, fast, and has the potential of on-chip pat-

terning and device fabrication. We believe that flat printing can be easily translated to rolling with engineering optimizations. This work is a stepping stone for roll-to-roll integration that could prove very useful for industry and has ample potential for commercialization.

2.4. Supporting information

2.4.1. Chemicals

1H,1H,2H,2H-Perfluorooctyltriethoxysilane (98%) – 510.36 g/mol; Polyvinylpyrrolidone (PVP) – average mol. wt. 55000 g/mol and 29000 g/mol; Silver nitrate ($AgNO_3$) – 69.8 g/mol; Copper chloride ($CuCl_2$) – 170.48 g/mol; 1,5-Pentanediol – 104.15 g/mol; Ascorbic acid (AA) – 76.12 g/mol; Potassium bromide (KBr) – 119 g/mol; Sodium tetrachloropalladate (Na_2PdCl_4) – 294.21 g/mol; mili-Q water (resistivity – 18 MΩ.cm at 25 °C) taken from a commercial purifier from Merck named Simplicity Water Purification System. Acetone – 58.08 g/mol (VWR); 2-Propanol (IPA) – 60.10 g/mol (VWR); Ethanol – 46.07 g/mol (VWR); Tetramethylammonium hydroxide solution (TMAH) – 25 wt.% in water; Silica spheres 50 nm (LOT: MKCJ8723); Latex beads polystyrene (LOT: MKCJ1534); Gold nanocubes with citrate capping (50 nm, LOT: J6911) from nanopartz.com. All the chemicals were purchased from Sigma Aldrich unless stated otherwise and used as received. Elastosil RT 601 A/B (RTV-2 Silicone Rubber) PDMS was bought from Wacker Chemie.

2.4.2. Synthesis

Ag nanocubes

A 5 ml solution of 0.235 M $AgNO_3$ in pentanediol was mixed with 40 µL of 0.043 M $CuCl_2$ and ultrasonicated for about 30 min until the solution turned turbid yellow-orange. PVP (mol. wt. 55000 g/mol) with a concentration of 40 g/l was prepared in pentanediol in a separate vial (ultrasonicate for fast dissolution). A round bottom flask was suspended in a silicone oil bath at 195 °C with 10 ml of pentanediol. After 10 min

of preheating, 500 µL of $AgNO_3$ and $CuCl_2$ precursor mixture was added in one go immediately followed by 490 µL of dropwise injection of PVP. After 30 s of precursor injection, another 490 µL of PVP was injected dropwise in the reaction flask. This marks the end of the 1^{st} cycle. Exactly 60 s after 1^{st} precursor injection begin the 2^{nd} cycle of injections and complete 5 cycles in total to make well defined (100) faceted cubes of 75 nm. The reaction mixture goes through a sequence of color changes and eventually, it turns creamy light green. The solution was stirred at 300 RPM and the flask was open to the atmosphere for the entire time and finally, after the 5^{th} cycle, it was quenched in a normal water bath. A series of centrifugation along with coarse and fine filtration was performed to isolate cubes from the rest of the byproducts of the synthesis. The Ag cubes were synthesized by adopting a modified procedure reported previously [24]. A major part of the experiments in this work was done with Ag cubes bought from nanoComposix, INC. Website: nanocomposix.com.

Pd nanocubes

The cubes were synthesized according to a previous report [144]. 105 mg PVP (55k), 60 mg AA, 600 mg KBr, and 8 mL mili-Q water are taken in a 20 mL vial. A stir bar is also added. The vial is placed in a preheated oil bath at 80 °C and stirred at 300 RPM. The solution turns colourless in a few minutes. Meanwhile, dissolve 57 mg Na_2PdCl_4 in 3 mL mili-Q water in a separate vial and after 10 min, inject this solution in the main reaction vial rapidly. Cap the vial and also wrap parafilm and let the reaction run for 3 hours. The solution will turn dark brown eventually. Let the vial cool down by air convection and later the product can be collected by centrifugation. The Pd cubes were finally dispersed in ethanol for subsequent use.

2.4.3. Silicon master fabrication

Exposure

12 x 12 mm Si substrates were cut from 4" Boron doped <100> orientation single crystal wafer purchased from Siegert Wafer GmbH, Aachen, Germany. Electron beam

lithography (EBL) was used to make nanopatterns on the these Si substrates. The instrument used was eLINE from Raith Nanofabrication GmbH installed in an ISO 7 Class 10000 cleanroom at AMOLF. The complete fabrication of the Si master was carried out in the cleanroom at AMOLF.

The Si substrates was cleaned with acetone, IPA and plasma (O_2 descum recipe) for 10 s with 50 W forward power oxygen plasma in a Plasmalab 80+ from Oxford Instruments and then immediately spin coated (without spinning bowl on top) with hydrogen silsesquioxane (HSQ) resist in a Delta 80 spin coater from Suss MicroTec. The resist was dropped from a syringe until it completely covers the Si substrate and then spun at 3200 RPM, 800 RPM/s acceleration for 45 s that resulted in 110 nm thick HSQ coated Si substrate. Then it was baked at 180 °C for 120 s. Subsequently, this substrate is exposed with e-beam with a dose of 4000 μC/cm^2 with circles of varying radii (300 nm, 500 nm, 1 μm, 2 μm, and 4 μm) and widths (100 and 200 nm). The column mode used for exposure was LC_60 μm with the area and curved elements exposure mode and step size of 5 nm along with beam current of 0.5 nA. A similar procedure was followed to make Si master with patterned ridges in the form of grids or gratings for imprinting.

Development

After exposure, it was developed in TMAH at 50 °C for 60 s and then rinsed twice thoroughly with water. This step dissolves all the unexposed resist leaving behind the nanopatterns of HSQ in the form of ridges on the Si substrate (Si master) as shown in Figure 2.6.

Etching

In order to make deeper trenches in PDMS, the Si master was etched to the desired height (Figure 2.7). The patterned lines of HSQ are made taller by plasma etching the Si substrate using the remaining resist in the form of patterns as the mask in COBRA (Oxford Instruments). The Si substrate is attached to a carrier wafer (4" Si) by Fomblin oil. The oil is used to improve the thermal conductivity between the

interface of the substrate and the wafer. For etching, Cl_2 + HBr/O_2 recipe is used where the initial 11 s of Cl_2 is used to remove the oxide layer on the Si and then the virgin Si is etched deeper by HBr/O_2 for another 4 min. The etching is carried out at 60 °C with a Cl_2 flow rate of 50 sccm which yielded ridges of 550 nm in height. Masters that didn't require etching were straight moved to the silanization step. The etched ones, before silanization, were subjected to HF bath (2% concentration) for 15 min for removing the residual HSQ from top of the ridges on the Si substrate.

Silanization

After development, if not subjected to etching, the Si master is baked at 200 °C on a hot plate for 30 min. Followed by this, it is again plasma treated for 10 s and placed beside 20 µL of 1H,1H,2H,2H-Perfluorooctyltriethoxysilane in a teflon boat at 50 °C in a Vacucenter VC20 vacuum oven from Salvis LAB, Switzerland at 50 mbar for 30 min. This treatment forms a self-assembled monolayer of fluorinated silane chains on the surface of the Si master and renders it highly hydrophobic. This facilitates peeling off the cured PDMS from the Si master.

2.4.4. PDMS stamp preparation

The PDMS stamp is prepared by mixing monomer and polymerizing agent in the ratio of 9:1. After thorough mixing and degassing (to eliminate air bubbles), the liquid mixture is poured onto a patterned F-silanized Si master. It is backed by a UV-Ozone activated (45 min in a UV Ozone ProCleaner from BioForce Nanosciences) glass slide and then cured in an oven at 80 °C for 24 hours. A Viton gasket made by a laser cutter (Speedy 400 from Trotec Laser B.V.) is used as the spacer layer to define the dimensions of the PDMS. This exercise results in a PDMS stamp as shown in Figure 2.8. The PDMS slab is 4 x 4 x 1 mm in dimensions and has nanotrenches on one side and bonded covalently to the glass slide on the other side.

2.4.5. Printing

Preparation of the Si substrate for imprint lithography

A Si wafer was spin coated with MICROPOSIT S1813 positive resist at 4000 RPM at the rate of 1000 RPM/s acceleration for 45 s. This resulted in a 1.3 µm thick resist layer that was baked at 115 °C for 60 s. This wafer was then exposed with a dose of 140 mJ/cm^2 (25 mJ/cm^2 for 5.6 s) in the hard contact mode in MABA6 Mask Aligner from SUSS MicroTec SE (Germany) using the foil mask shown in Figure 2.9a. The mask was printed with a laser printer on a transparency and then manually overwritten with a permanent marker on the printed 5 mm spots. Then the transparency was stuck to a quartz plate with sticky tape and used as it is for exposure. After exposure, the wafer was developed in MICROPOSIT MF - 319 for 60 s and then rinsed with water. This results in a wafer as shown in Figure 2.9b. This Si wafer was further silanized and made hydrophobic as aforementioned in section Si master fabrication. This made the Si surface hydrophobic everywhere except the center 5 mm dot covered with resist. Subsequently, the wafer was diced along the straight lines to make 10 x 10 mm Si substrates used for imprinting.

Imprinting

The printing experiments were carried out with the help of a Universal Testing System model 5965 with 50 kN force capacity from INSTRON, Massachusetts, USA. A custom holder was made to mount the PDMS stamp and the Si substrate with the clamps of the machine as shown in Figure 2.11-a,b. The holder was also equipped with a Peltier element to heat or cool the sample stage as required. The stamp and the Si substrate were held in place on the respective holders via vacuum.

The 10 x 10 mm Si substrate was ultrasonicated in acetone and IPA for 60 s each to clean the resist. Subsequently, it was activated by UV-Ozone treatment for 30 min and then mounted on the holder. 1 µL of the colloidal Ag cubes (or the desired ink) dispersed in ethanol was dispensed on the activated substrate and let it dry to form a film of cubes on the substrate. After complete drying, 3 µL of pure ethanol was added to the same spot as the cubes (rewetting on the PDMS stamp instead of the sample works equally well) and the stamp was pressed on the substrate at the rate of 1

mm/min until the force of 10 - 30 N. The solvent was allowed to dry (either overnight or heating the substrate to 40 °C) before the stamp was retracted at the rate of 10 µm/min - 1 mm/min. Excess cubes stuck to the surface of the stamp or in the trenches after printing can be easily removed (or retrieved) by ultrasonicating the stamp for 5 min in the very same solvent in which the cubes were dispersed. After this step, the stamp is practically very clean and can be reused again and again by applying the same cleaning protocol. The concentration of the inks was adjusted to 1 mg/mL.

2.4.6. A few parameters to ensure good fidelity of the process

1. It is recommended to bond the template/PDMS to the glass support and not rely on the temporary physical bond. The PDMS can move during printing against the glass and tiny movements can disrupt the patterns.

2. The quality of patterns is greatly affected by the quality of the stamp. Thus, often neglected, it is highly advised to take the stamp fabrication process seriously.

3. Always clean the residual particles in/on PDMS as soon as possible after printing. The longer you wait, the lesser the chance to get rid of particles and retain a cleaner stamp. The stamps were always stored in ethanol. This also helps to eliminate the uncured monomers in the PDMS over time.

4. The solvent must evaporate completely before the withdrawal of the stamp so choose a solvent that can permeate through PDMS.

5. Smaller the trenches or tighter the clearance of trenches for the particles, longer it takes to evaporate all the solvent for a clean print.

6. There is a threshold pressure for Ag cubes for patterns to form and push out the residual cubes. It was found to be 0.375 MPa.

7. Fresh and clean Si is readily hydrophilic, however, activation via UV-Ozone will ensure even and complete wetting of the ink on the activated area on the

substrate. It is an important step during stamping.

8. Clamping the stamp and substrate to the respective holders via vacuum has been found as one of the best clamping methods. For this, use a very soft and flexible tubing for air suction as rigid tubing can introduce additional jitter/force in the system disrupting the patterns.

2.4.7. Supplementary figures

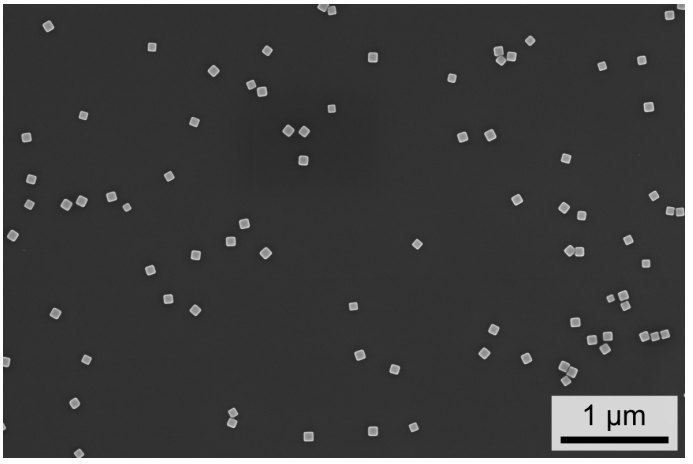

Figure 2.5: Scanning electron microscopy (SEM) image of 75 nm Ag nanocubes capped with PVP dropcast on a Si substrate.

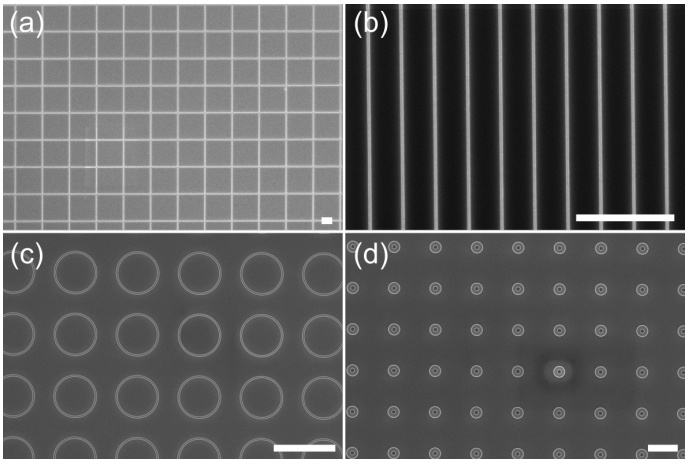

Figure 2.6: Representative images of the Si master used to make PDMS stamps. Pattered ridges in the shape of (a) grids, (b) gratings, and (c,d) circles of different width, pitch, and radius of curvatures made by EBL. The scale bars are 2 μm for (a), (b) and 12 μm for (c), (d) in length.

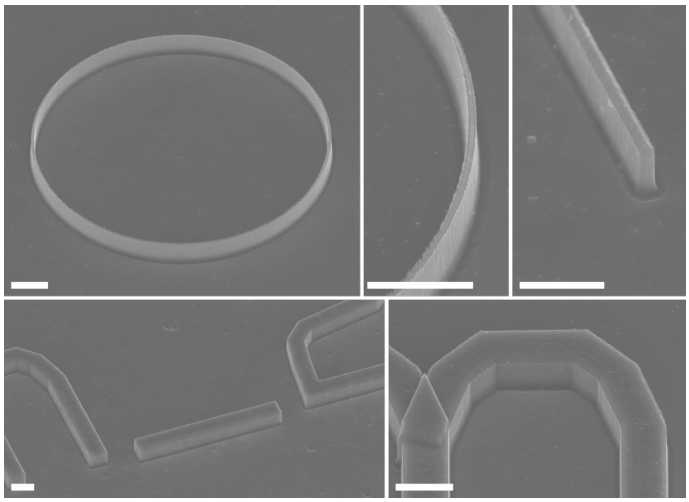

Figure 2.7: Representative images (acquired at 45° tilt) of the Si master used to make PDMS stamps. Pattered ridges of 550 nm height on Si made by EBL and subsequent etching. All scale bars are 1 µm in length.

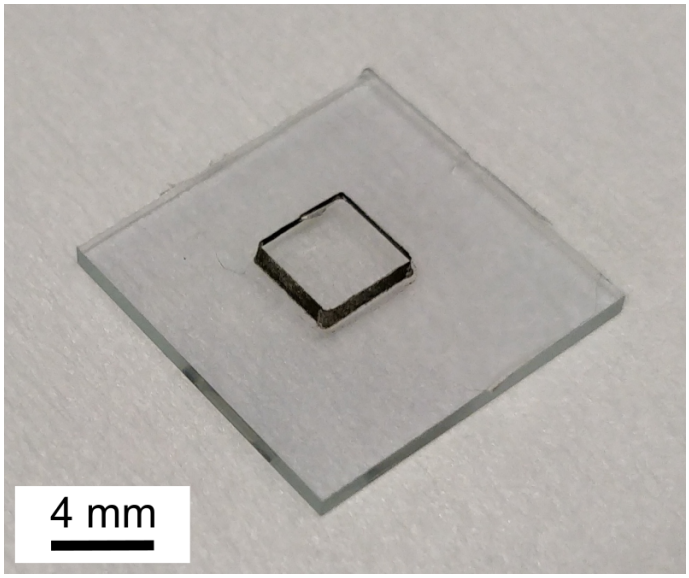

Figure 2.8: PDMS stamp used for imprinting. The square-shaped rubber slab in the center is 4 x 4 x 1 mm in dimensions and covalently bonded to a 15 x 15 x 1 mm glass slide.

Dimension (mm)	Pattern	Radius of curvature (μm)	Pitch (μm)	Trench width (nm)	Trench depth (nm)
4 x 4 x 1	Circular	4, 2, 1, 0.5, 0.3	12	100, 200	120
4 x 4 x 1	Circular	4	12	100, 200	550
			Pitch (μm)		
4 x 4 x 1	Gratings	1.4, 5		200, 400	120
4 x 4 x 1	Gratings	10		100, 200	550
4 x 4 x 1	Grids	5		100, 200	120
4 x 4 x 1	Cubic lattice	0.6		85	90
4 x 4 x 1	Rhombic lattice	0.6		85	90

Table 2.1: Parameters of the PDMS stamps used for imprinting.

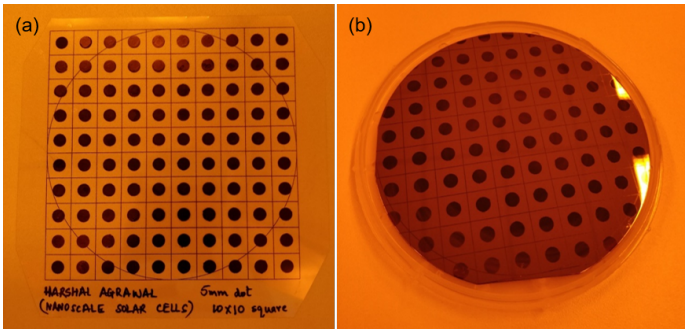

Figure 2.9: Foil mask which was prepared in-house on a projector transparency. (b) 4" Si wafer exposed with the mask shown on the left to selectively fluorosilanize the wafer.

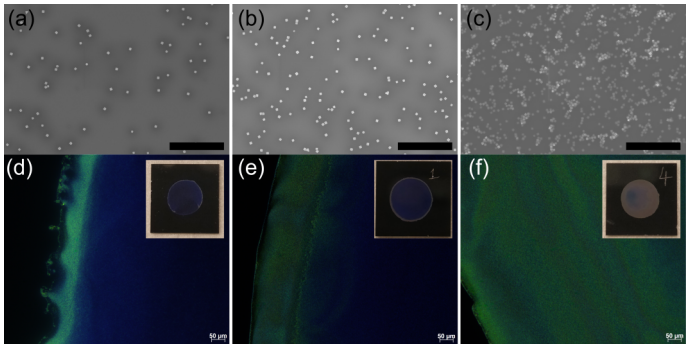

Figure 2.10: Ag nanocube resist images. (a), (b), and (c) are the SEM images of the nanocube resist formed by dropcasting 0.5 µL, 1 µL, and 4 µL Ag cube stock solution. The images were acquired from the center of the substrate shown in the inset of (d), (e), and (f) respectively. (d), (e), and (f) are the optical images at the edge of the resist showing a locally enhanced concentration. This enhanced concentration of cubes at the edge can also be seen in the camera image of the substrate in the inset. Besides the edge, the rest of the resist layer has a uniform concentration at length scales beyond 10 µm. The scale bars in (a), (b), and (c) are 2 µm in length.

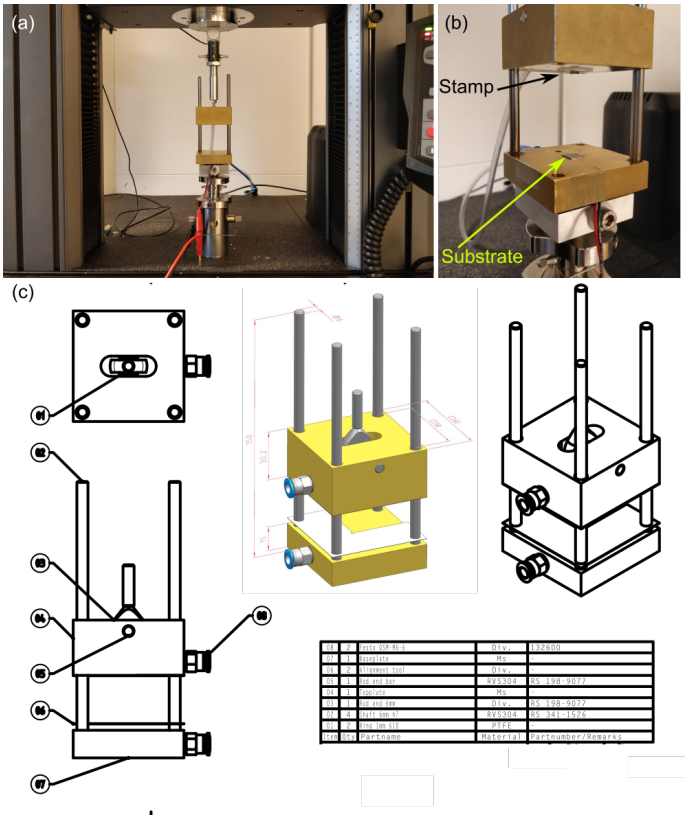

Figure 2.11: The INSTRON machine used for flat imprinting. (a) Custom made holder fitted on the machine. (b) A close-up view of the holder with a stamp and a substrate in the respective places. (c) Engineering drawing of the holder. The dimensions marked on the colored sketch are in mm.

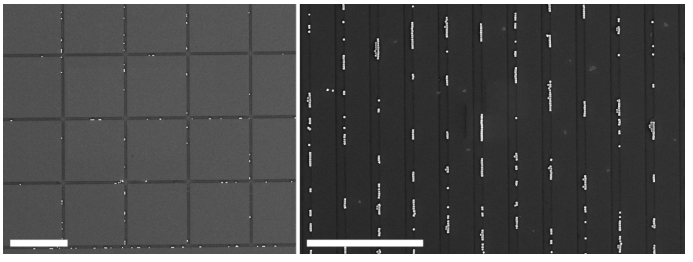

Figure 2.12: SEM images of patterns printed before drying the solution to form a resist film of Ag cubes. It leads to highly non-uniform patterns, with many trenches missing particles. The scale bars are 5 µm in length.

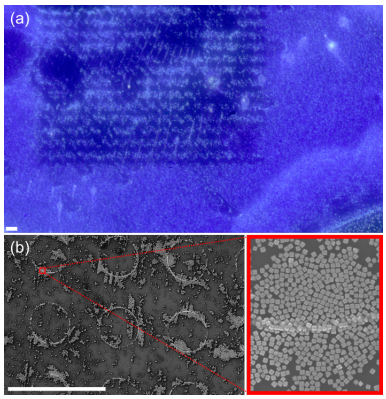

Figure 2.13: (a) Optical and (b) SEM images of imprinting on the dry nanocube resist of Ag cubes. It led to many particles remaining on the substrate in areas outside the targetted pattern. The scale bars are 10 µm in length.

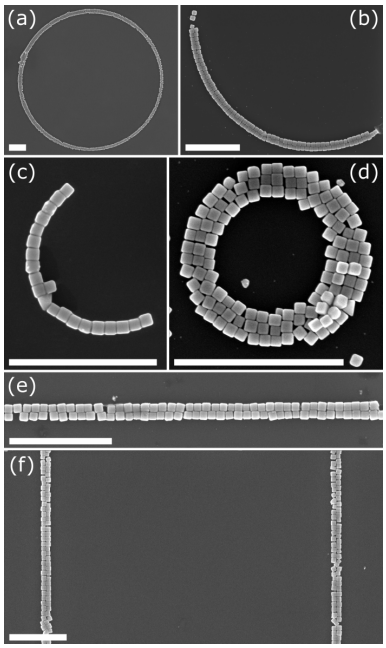

Figure 2.14: SEM images of printed curves of (a) 4 µm, (b) 2 µm, (c) 500 nm, and (d) 300 nm radius of curvature. (e-f) Straight line profiles printed with Ag cubes. The scale bars are 1 µm in length.

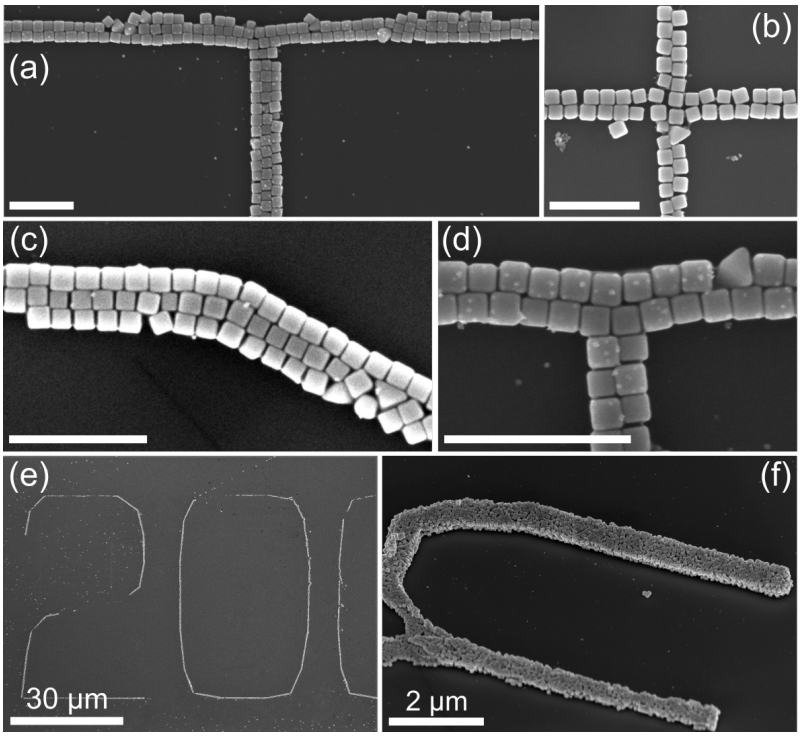

Figure 2.15: Various junctions and arbitrary patterns demonstrated with the imprinting process with Ag cubes. All the scale bars are 500 nm in length if not specified. The height of patterned 'zero' in (e) is 52 µm.

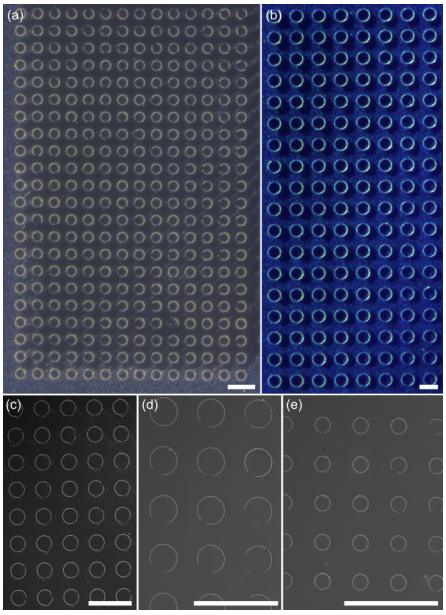

Figure 2.16: Large scale flat imprinting of Ag nanocubes in curved profiles. (a) and (b) are the optical images. (c), (d), and (e) are the SEM images. All scale bars are 25 μm in length.

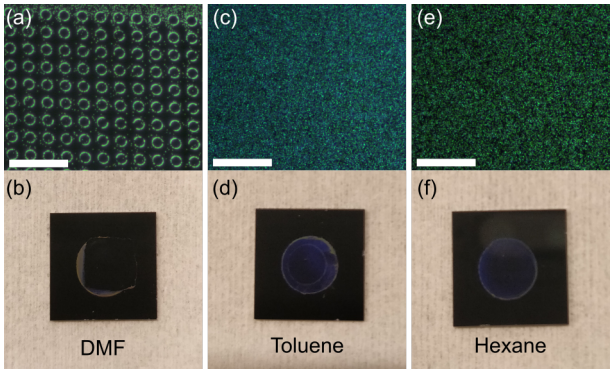

Figure 2.17: (a), (c) and (e) are optical image taken from the substrate shown in (b), (d) and (f) respectively. (b), (d) and (f) are the camera images of the substrates after imprinting when the nanocube resist was rewetted with dimethylformamide (DMF), toluene, and hexane respectively. All scale bars are 50 μm in length.

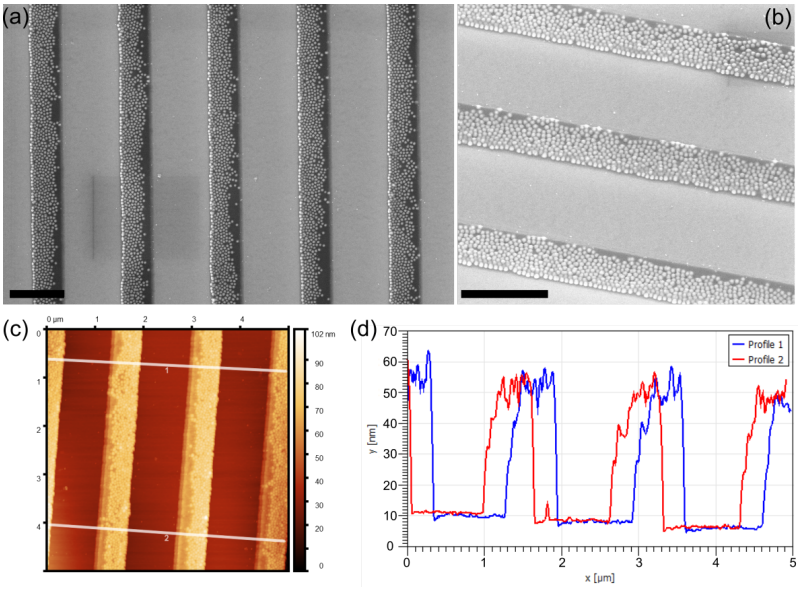

Figure 2.18: (a) Top and (b) titled view SEM images of gratings of 1.4 µm pitch printed with commercially available 50 nm silica spheres on a Si substrate. (c) AFM image and the corresponding (d) height profile of the gratings. All scale bars are 1 µm in length.

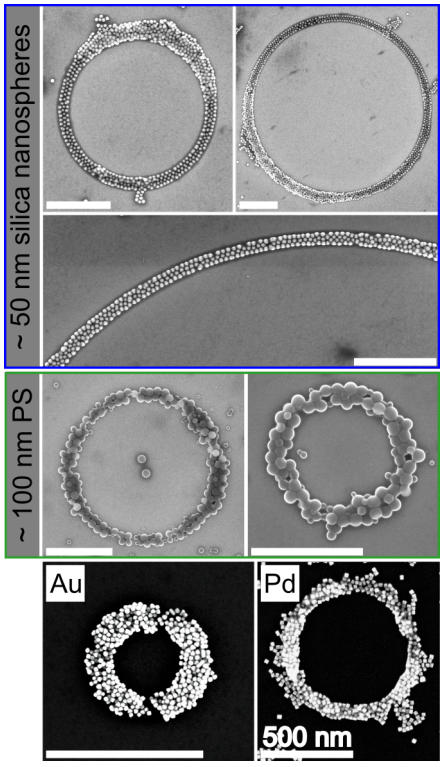

Figure 2.19: Imprint of different materials like 50 nm silica spheres in the blue square, 100 nm polystyrene (PS) beads in the green rectangle, 50 nm Au cubes, and 20 nm Pd cubes. All scale bars are 1 µm in length unless specified.

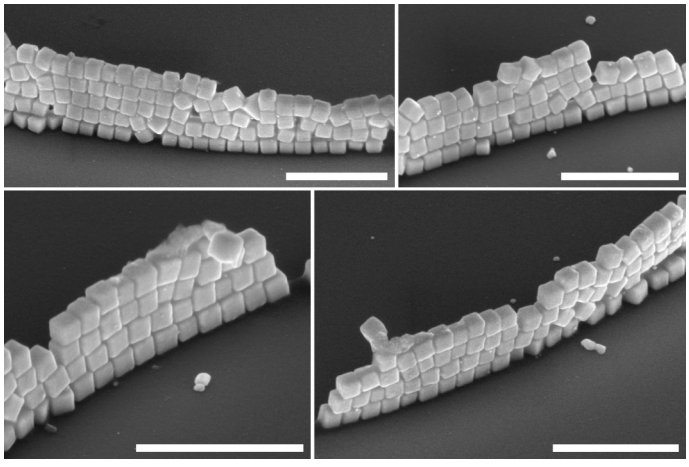

Figure 2.20: SEM images of high aspect ratio lines. All scale bars are 500 nm in length.

3

Quantifying Strain and Dislocation Density at Nanocube Interfaces after Assembly and Epitaxy

Nanoparticle self-assembly and epitaxy is utilized extensively to make 1D and 2D structures with complex shapes. High-resolution transmission electron microscopy (HRTEM) has shown that single crystalline interfaces can form, but little is known about the strain and dislocations at these interfaces. Such information is critically important for applications: drastically reducing dislocation density was the key breakthrough enabling widespread implementation of light-emitting diodes, while strain engineering has been fundamental to modern high-performance transistors. In this work, the interfacial defect and strain formation after self-assembly and room temperature epitaxy of 7 nm Pd nanocubes capped with polyvinylpyrrolidone (PVP) is examined. It is observed that during ligand removal, the cubes move over large distances on the substrate, leading to both spontaneous self-assembly and epitaxy to form single crystals. Subsequently, atomically resolved images are used to quantify the strain and dislocation density at the epitaxial interfaces between cubes with different lateral and angular misorientations. It is shown that dislocation- and strain-free interfaces form when the nanocubes align parallel to each other. Angular misalignment between adjacent cubes does not necessarily lead to grain boundaries but does cause dislocations, with higher densities associated with larger rotations.

3.1. Introduction

Self-assembly of nanocrystals and successive epitaxy by either dissolving the capping ligands in a suitable solvent or via a chemical trigger has emerged as a promising route to make single crystals with complex nanoscale geometries [75, 145–153].This approach is very flexible, including variants where particles are both assembled and epitaxially connected in solution – usually called oriented attachment [151, 153–158] – or where assembly first occurs at an interface (liquid-liquid, liquid-solid or liquid-vapor) [29, 34, 68, 75, 145, 153, 159–165] followed by the epitaxy step (thermal, chemical or optical) [71, 72, 75, 147, 148, 158, 166–168]. Interfacial assembly via aforementioned techniques can lead to 2D films with nanoscale patterns determined by the shape and surface energetics of the particle, such as a 2D honeycomb lattice, or to more complex nanopatterns formed by capillary assembly [38, 68, 145, 169, 170]. In all cases, the choice of materials is broad with a variety of metals, semiconductors, and dielectrics already demonstrated [39, 68, 75, 146, 150, 161, 169, 171–173]. Theoretical simulations and in situ observation of assembly using HR-TEM and x-ray scattering studies have helped provide insights into the mechanism of assembly and epitaxial connection [170, 174–180].

Despite this vast amount of work in the field of oriented attachment and growth, little is known about the interfacial strain and dislocations at the interfaces after epitaxy [181–184]. One study showed that PbSe truncated octahedral nanocrystals with large angular misalignment can have up to 7 edge dislocations after initial attachment that can so far only be removed with annealing at elevated (100 °C) temperatures [175]. Epitaxial particles with perfect angular alignment might be free from strain and dislocations, but this is yet to be probed experimentally. Even with perfect angular alignment, strain- and defect-free epitaxy would require either perfect atomic alignment (no lateral displacement) during assembly, or some particle mobility during epitaxy to provide atomic registry. Understanding the formation of strain and dislocations at these interfaces is critically important to assess suitability for applications. For example, removing dislocations from epitaxial GaN films was the key breakthrough

enabling widespread implementation of light-emitting diodes [82], while strain engineering is used extensively in modern transistors to improve the mobility of the channel [76]. Strain and dislocations also play a fundamentally important role in other devices including photovoltaics and thermoelectrics [79, 85, 185–187].

In this work, we use high angle annular dark-field scanning transmission electron microscopy (HAADF-STEM) to characterize dislocation and strain formation during nanocube self-assembly and epitaxy at room temperature. Nanocubes, sometimes showing slightly rounded edges or elongation in one direction, are chosen over octahedron, decahedron, icosahedron, and other morphologies as the model system because of their atomically flat and chemically equivalent faces which simplify both assembly and atomic merging [174, 175, 184, 188]. The strain and number of dislocations at the interface of epitaxially connected 7 nm Palladium (Pd) nanocubes capped with PVP are quantified from the HAADF-STEM images using a model-based image quantification approach implemented in the StatSTEM software [189]. After dropcasting Pd nanocubes on the substrate, we observed that they move up to hundreds of nanometers during the PVP removal with sodium borohydride ($NaBH_4$), enabling spontaneous self-assembly. We confirm that this surface mobility allows for the formation of single crystalline interfaces with strain values below 5% and no signs of dislocations. In cases where particles have larger angular misalignment, we observed a higher dislocation density and strain.

3.2. Results and discussion

Nanoparticle assembly and epitaxy has been utilized in the past to make 1D and 2D structures by stitching together small nanocrystals as the building blocks. In this work, when monocrystalline 7 nm Pd cubes (Figure 3.5 and 3.6) are treated with $NaBH_4$, the cubes migrate over substantial distances on the substrate, transforming from isolated particles to assembled clusters. The cubes self-assemble into a variety of geometries like lines, L shapes, and triangles etc. as shown in Figure 3.1-a,b. During the epitaxy step, $NaBH_4$ acts as the hydride donor which displaces the shape controlling ligands

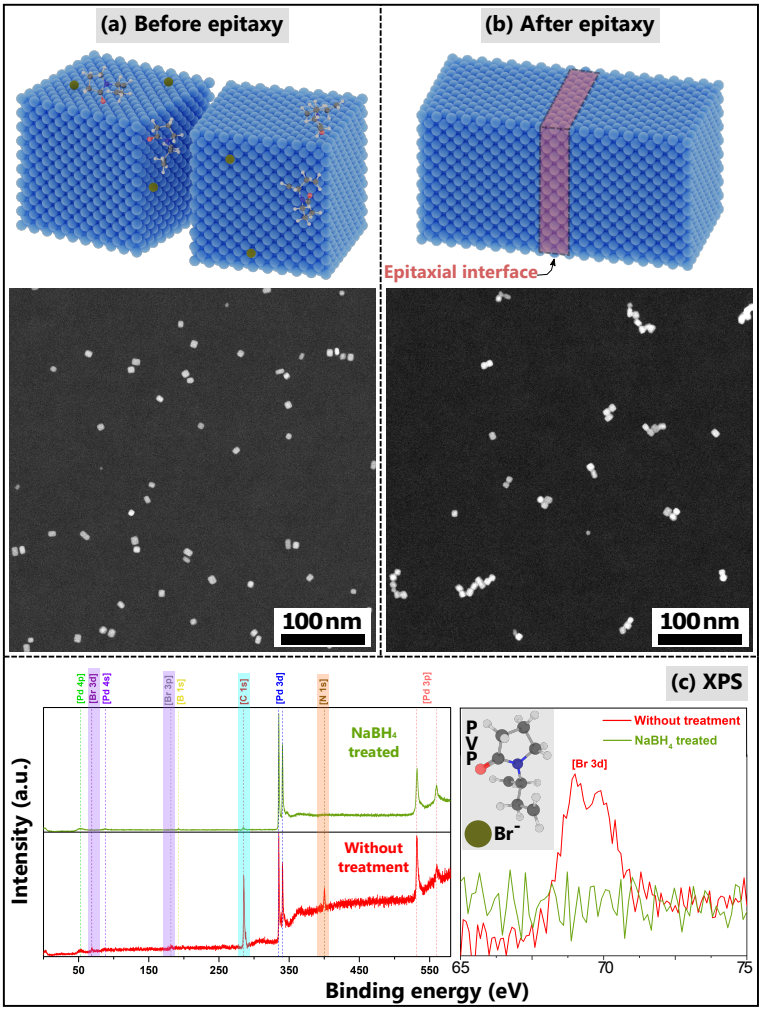

Figure 3.1: Investigation of chemical epitaxy. (a) The schematic of the randomly distributed dropcast cubes on the substrate and the corresponding HAADF-STEM image before epitaxy. The surface of the cube is populated with Br- (green) and PVP which binds either via nitrogen atom (blue) or carbonyl oxygen atom (red). In the schematic, only a few molecules of capping ligands (PVP monomer and Br-) are shown on the surface of cubes for the simplicity of illustration. (b) The schematic and the corresponding HAADF-STEM image of cubes after epitaxy (after treatment with 0.1 M $NaBH_4$ for 15 min). (c) XPS spectra showing the surface chemical composition of the cubes without (red) and after (green) $NaBH_4$ treatment. The spectrum on the right is the high-resolution scan in the range 65 to 75 eV of the main spectrum and the inset shows the schematic of the binding ligands.

Br^- and PVP from the surface of the Pd nanocubes [132, 144, 190–192]. The surface sensitive X-ray photoelectron spectroscopy (XPS) characterization data in Figure 3.1-c clearly reveal that after the $NaBH_4$ treatment, the N (orange) and Br (purple) peaks are missing. The O peak overlaps with Pd 3p and hence cannot be quantified. The major peaks in the XPS scan after epitaxy (green) are from Pd metal, with a minor peak from residual C, indicating most of the surface ligands used during synthesis are eliminated [191]. This surface ligand removal enables the high particle surface mobility and translation along the substrate, but at the same time may contribute to some particles partially losing their cubic shape (Figure 3.2 and Figure 3.7-a,b).

One striking feature of the ligand-removal process is that in the same step the connection between adjacent cubes results in atomic alignment and epitaxy leading to the formation of a single crystal (Figure 3.2 and Figure 3.7). Predominantly, nanocubes join along the {100} facets with differing degrees of orientational alignment. Thanks to their cubic shape and the presence of flat {100} facets, imaging of assembled cubes is mainly performed along a <100> zone axis without tilting our sample significantly. In Figure 3.7a, an image of an assembled couple along a <110> zone axis is also provided. From Figure 3.2-b,c, it is clear that even a 3.5° misalignment of adjacent cubes resulted in an epitaxial connection.

Epitaxy between nanocrystals with small angular misorientations has been observed previously to lead to dislocations as would be expected [184], but dislocations and strain in epitaxially connected nanocubes without angular misorientation has not been studied. Even for two nanocubes with perfect angular alignment and the same lattice constant, lateral displacements could lead to dislocations or strain. It is also possible that during epitaxy, the particles move into perfect atomic alignment in order to avoid such dislocation or strain formation, leading to the preferential formation of perfect interfaces. In order to differentiate between these two possibilities, we use nanocubes, which are characterized by six chemically equivalent and atomically flat faces, making them an ideal system for our study where the lower energy of face-to-face alignment increases the chance of perfect angular alignment. The surface

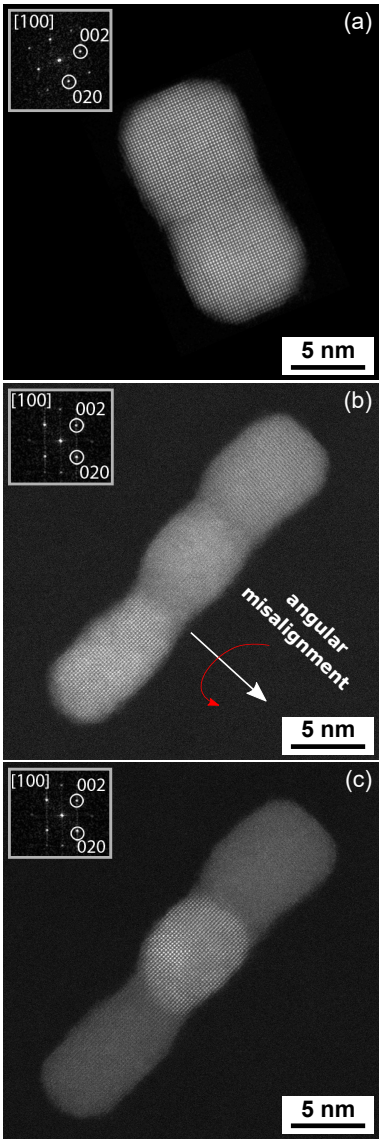

Figure 3.2: HAADF-STEM images of epitaxial assemblies (a) with perfect angular alignment and (b,c) with 3.5° angular misalignment. The micrograph in (c) was obtained by rotating the assembly in (b) 3.5° along the direction indicated by the red arrow, indicating an epitaxial connection between the cubes. The Fourier transforms of the epitaxially connected cubes are shown as insets in all the micrographs.

atom mobility and cubic shape distortion enabled by ligand removal could reduce the efficacy of the assembly. However, since we see still a high fraction of aligned clusters, this shape distortion likely occurs primarily after particle attachment and during epitaxy. Local strain and dislocations at the epitaxial nanocube interface were studied using the StatSTEM software. When two cubes come together with perfect angular alignment during epitaxy, they can merge such that there are no dislocations at the interface (Figure 3.3 and Figure 3.8, 3.9). A small angular misalignment of two-degrees can lead to an epitaxial connection with the presence of one dislocation, with locally higher strain values (Figure 3.4). We also verified that a larger angular misalignment of four-degrees leads to a higher dislocation density (Figure 3.10). Thus, in patterns assembled from perfect monocrystalline building blocks, dislocation formation is controlled by the angular misalignment. Besides enabling high surface mobility that is beneficial in reaching the ideal angular alignment, our $NaBH_4$ ligand removal process is also much faster than previous approaches. For example, relying on ligand solubility to trigger the fusing requires up to 16 hours [68, 147] while $NaBH_4$ can eliminate the surface capping ligands within one minute.

Nanocube epitaxy requires two separate steps and both depend on ligand removal. First, the cubes must overcome the van der Waals attraction with the substrate, allowing for sufficient surface mobility to enable rapid surface diffusion even at room temperature. This allows for the isolated nanocubes formed after dropcasting to come together to form the observed clusters. Such large-scale movement (~100 nm) can be explained by partial removal of the surface ligands that bind to the substrate, along with the local evolution of the hydrogen generated when $NaBH_4$ is dissolved in water [193]. During clustering, nanocubes will attempt to maximize the area of overlap between {100} faces in order to reduce the surface energy of the system, providing a driving force for angular alignment such that cubes are oriented along the same crystallographic axis. This explains the predominance of short lines and L-shapes observed after $NaBH_4$ treatment. As the nanocube cluster grows, its surface diffusion will also slow down dramatically, which can explain the small number of

cubes observed in most clusters.

Once the nanocubes have formed clusters, the atoms at the surface must also rearrange to allow for the epitaxial connection observed. Here again surface ligands play a key role, with as little as 15% removal dramatically decreasing the interparticle spacing, with the potential minimum occurring at interparticle contact [194]. At such small distances, epitaxial connections occur to minimize the free energy of the system [148, 149, 184, 188, 194, 195]. The potential for eliminating dangling bonds leads to a strong enthalpic driving force; in the case of 7 nm Pd cubes, more than one thousand atomic bridges per {100} face will be formed.

Stress and dislocation formation in perfect monocrystalline Pd particles depend on the alignment between adjacent cubes after self-assembly. With perfect angular and lateral alignment between cubes, it is verified experimentally that perfect strain- and dislocation-free connections can form. The formation of such strain- and dislocation-free interfaces is not expected only with perfect angular alignment. This is because after assembly the atoms at opposite sides of the interface should have random lateral

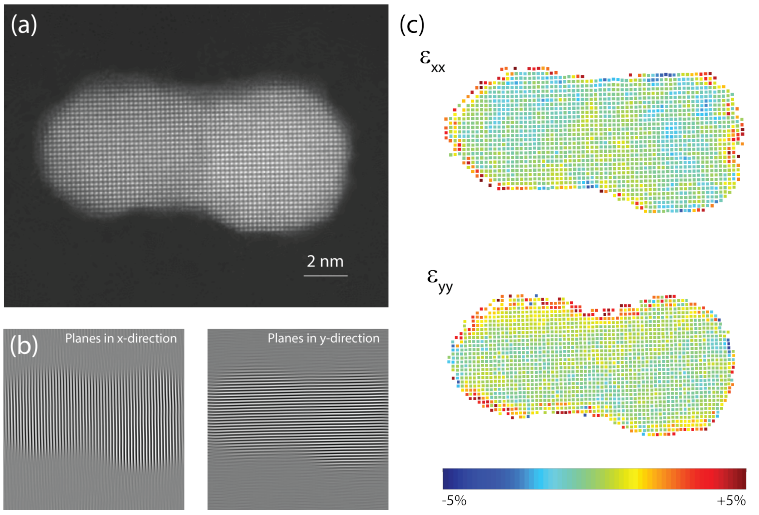

Figure 3.3: Dislocation and strain analysis of 2 epitaxial cubes with no dislocation. (a) HAADF-STEM image of the epitaxial cubes. (b) Inverse Fourier transform images showing the individual planes along the x and y directions, illustrating the absence of any dislocation. (c) Strain maps computed for x and y directions, indicating the absence of strain at the interface of the two cubes.

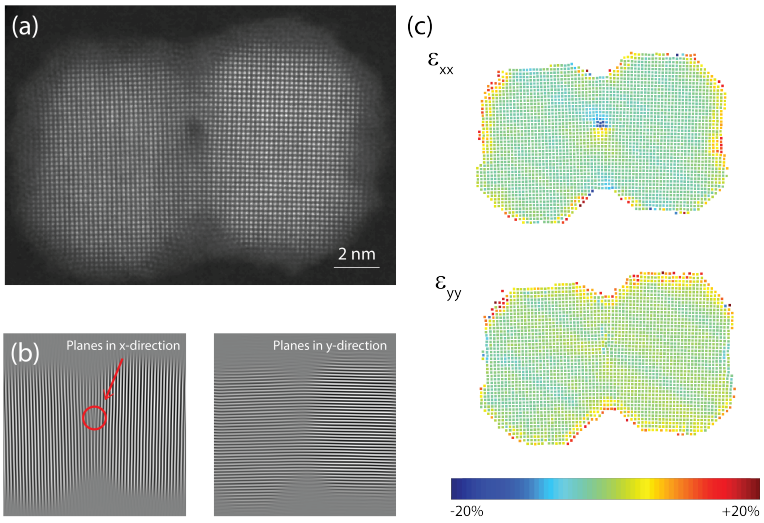

Figure 3.4: Dislocation and strain analysis of 2 epitaxial cubes with a 2° angular misalignment and one dislocation (a) HAADF-STEM image of the epitaxial cubes (b) Inverse Fourier transform images showing the individual planes along the x and y directions respectively, illustrating the presence of one dislocation, indicated by the red arrow. (c) Strain maps computed for x and y directions.

displacements, leading to a mismatch of up to half a lattice period, which must be accompanied by strain, dislocations or both. Therefore, our observation of strain- and dislocation-free epitaxial interfaces requires that nanocubes move laterally, at least over small (sub-nm) distances during the epitaxial connection process itself.

Interestingly, it is observed that the ligand removal can also form a single crystal even if the cubes are not perfectly aligned. A local movement of atoms within misaligned cubes can still lead to an epitaxial connection (Figure 3.2-b,c, Figure 3.11). The driving force for this local rearrangement of atoms, which also contributes to the change in shape of the cubes, is to avoid the strain caused by the formation of unaligned connections. This atomic surface diffusion process allows for at least a few degrees (4°) angular misalignment (Figure 3.2-b,c, Figure 3.10) between cubes without leading to a grain boundary formation. However, in the cases where local movement is still not enough to form fully strain free connections as a result of lateral or angular misalignments, the system compensates by nucleating dislocations

at the interface to accommodate the strain energy. Figure 3.4 shows an example of a pair of nanocubes with a two-degree angular misalignment, which leads to a single dislocation. Although the strain is generally close to zero throughout the epitaxial pair (except at the surface), locally around the dislocation high strain values of 10-20% exist, as expected. Although we do not have enough statistics to make a quantitative correlation between misorientation angle and dislocation density, we do observe that an epitaxial pair with a higher misorientation angle of four-degrees has substantially more (five) dislocations (Figure 3.10). This is very different from the results seen when bending single crystalline, twinned Ni nanowires with similar dimensions (1-6 nm), which were able to accommodate very large lattice rotation angles of up to 38.5 degrees (shear strain up to 34.6%) without nucleating either grain boundaries or dislocations [196]. We suspect that the drastic difference from our results, where dislocations formed already at rotation angles as little as two-degrees, arises from the difference between bending a preformed single crystal (twinned in the case of Ni nanowires) versus epitaxially connecting separate nanocubes with a rotation angle between them. In our case, the two particles start with relaxed lattices and strain or dislocations will nucleate from the interface during epitaxy, while in the preformed nanowires strain builds up continuously over a much larger area and dislocations must nucleate at the nanowire surface. In our system, the nucleation energy for dislocations appears to be lower, which seems to lead to a higher dislocation density but lower strain compared to the preformed nanowires, although further work is needed to quantify these differences. In the case of already perfectly aligned cubes, no rearrangement of atoms is needed to form strain- and dislocation-free epitaxial connections and as a result, they also retain their near cubic shape (Figure 3.2a).

3.3. Conclusions

We have studied the strain and dislocations generated at the interface of assembled and epitaxially connected 7 nm Pd cubes. Aqueous $NaBH_4$ solution plays a key role in both the spontaneous nanoparticle assembly and epitaxy steps, by promoting

the removal of the surface capping ligands at room temperature within a minute. The mobility of both the nanocubes on the substrate surface and Pd atoms on the nanocube surface enables the formation of dislocation-free single crystals when cubes show perfect angular alignment. The lack of strain and dislocations at this interface indicates that cubes must also be able to move along the substrate during the epitaxial attachment. For angular misalignment up to 4 degrees, epitaxial connections between adjacent cubes still form, but with higher strain and dislocation density. Given that the crystal quality of assembled and epitaxially connected nanocubes (or particles in oriented attachment) can be comparable to bulk single crystals, such an approach is very promising for applications.

3.4. Supporting information

3.4.1. Chemicals

Polyvinylpyrrolidone (PVP) – average mol. wt. ~55000 g/mol; L-Ascorbic acid – reagent grade, crystalline; Potassium bromide (KBr) – BioXtra, >99% purity; Potassium chloride (KCl) – BioXtra; Sodium tetrachloropalladate(II) (Na_2PdCl_4) - powder and chunks, 99.99% trace metal basis; Sodium borohydride ($NaBH_4$) – granular, 99.99% trace metals; mili-Q water (resistivity – 18 M_Ω.cm at 25 °C) taken from a commercial purifier from Merck named Simplicity Water Purification System. All the chemicals were purchased from Sigma Aldrich unless stated otherwise and used as received without any further processing.

3.4.2. TEM grids

The Silicon Nitride (Si_3N_4) grids (product no: 21505-10) were purchased from Ted Pella, Inc, USA. The grids have 50 nm Si_3N_4 thick membrane with 200 µm frame thickness and a window of 0.25 x 0.25 mm.

3.4.3. Preparation of the precursor

Na_2PdCl_4 (57 mg) was dissolved in mili-Q water (3 mL). The dissolution takes a long time so mild heating with periodic ultrasonication followed by vortexing is recommended.

3.4.4. Synthesis

The synthesis was adopted and modified from a reference [144]. In brief, PVP (105 mg), L-Ascorbic acid (60 mg), KBr (5 mg), KCl (185 mg), and mili-Q water (8 mL) were placed in a vial (20 mL) and preheated at 80 °C for 10 min in a silicone oil bath with magnetic stirring at 300 RPM. The vial was loosely caped from the top. Previously prepared Na_2PdCl_4 (3 mL) was injected in the reaction vessel and left for 3 hours; vial capped from the top with paraffin. After 3 hours, the reaction vessel was removed from the oil bath and left for air convection cooling. Post-synthesis, the solution was centrifuged at 5000 RPM for 10 mins to settle the coarse particles. The supernatant was centrifuged at 50000 RPM for 30 min in order to isolate nicely faceted ~7 nm cubic Pd particles and dispersed in ethanol.

3.4.5. Chemical epitaxy

The sample was prepared by dropcasting the colloidal solution (10 µL) on a Si_3N_4 grid. The ligand removal and epitaxy were performed by immersing the grid in $NaBH_4$ (0.0189 g in 5 mL water, 0.1 M) solution without any stirring. After 15 min, the grid was cleaned in a solution of 1:1 ratio by volume of water and ethanol for ~2 hours with stirring at 150 RPM. It should be noted that each time a fresh solution of $NaBH_4$ was used for ligand removal and epitaxy.

3.4.6. Dislocation visualization

Potential dislocations are visualized by showing the individual lattice planes in the x- and y-direction. In order to visualize these, first a Fourier transform is obtained

from the HAADF STEM image. Next, two symmetric lattice points in the x- or y-direction are masked from this Fourier transform. The inverse Fourier transform of these masked reflections results in a visualization of the potential dislocations which might appear at the interface.

3.4.7. Strain maps

The strain maps are obtained using the StatSTEM software [189]. By modeling images as a superposition of Gaussian functions located at the atomic columns, the atomic column positions can be measured with high accuracy and precision. A direct comparison of the measured column positions with the expected column positions of an ideal crystal lattice gives the displacement of the atomic columns. By using the first derivative, these measured displacement vectors can be used to compute atomically resolved strain maps.

3.4.8. Scanning transmission electron microscopy (STEM)

HAADF-STEM images were acquired using an aberration-corrected 'cubed' FEI Titan electron microscope operated at 300 kV. A probe convergence semi-angle and a detector collection inner semi-angle of 21 mrad and 55 mrad, respectively, were used for image acquisition.

3.4.9. X-ray diffraction (XRD)

XRD measurements were performed on a clean regular glass cover-slip of 200 µm thickness on the Bruker D2 Phaser in Bragg-Brentano geometry equipped with Lynx-eye detector (1 Dimensional). The X-ray source used was standard Cu - K_α with an emission energy of 8.0415 keV. A Nickel filter was used to reduce the signal contribution from Cu - K_β. All the measurements were equipped with a 1 mm knife which acts as a beam cutter to minimize unwanted scattering. The measurements were conducted in ambient air with a collection time of 12 hours to maximize the signal to

noise ratio. The scanning interval was 0.01°.

3.4.10. X-ray photoemission spectroscopy (XPS)

It was performed in a home-built ultrahigh-vacuum chamber, operating at a base pressure below 5×10^{-9} mbar. The X-ray source (Al-K_α line) used was XM1000 from Scienta Omicron with excitation at 45° angle. The system has FWHM around 430 meV with an imaging resolution of less than 10 µm. The sample holder geometry used was omicron flag sample holder. The photo-emitted electrons were detected using an R4000 HIPP-3 detector also from Scienta Omicron. The 10 x 10 mm Si substrates used for the analysis were cleaned with soap followed by acetone and IPA and were blow-dried. 100 mL of the sample was dropcasted onto the substrate and used directly for the scan before epitaxy. The same substrate was then treated with 0.1M $NaBH_4$ for 15 min and then cleaned with water and IPA mixture and then scanned for XPS.

3.4.11. Supplementary figures

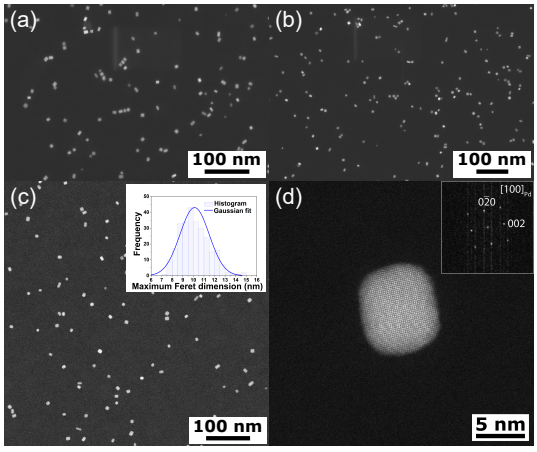

Figure 3.5: Pd cubes characterization. (a), (b), and (c) show low magnification HAADF-STEM images of the cubes used in the study. The inset in (c) shows the particle size distribution calculated based on ~300 particles. (d) High-resolution HAADF-STEM image of a Pd cube, together with the Fourier transform shown in the inset.

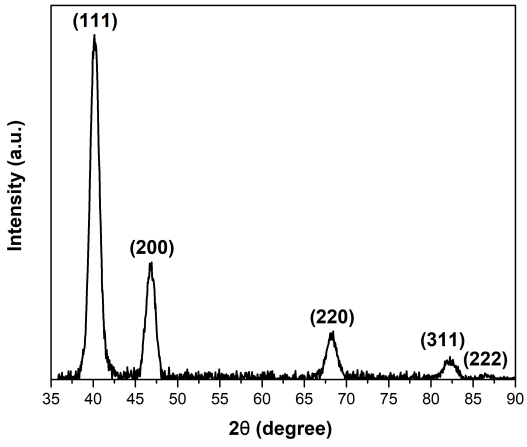

Figure 3.6: XRD scan of the as-synthesized cubes dropcasted on a glass substrate. All the peaks can be indexed to face-centered cubic (FCC) crystal structure of Pd and correspond to JCPDS card 05-0681 [197].

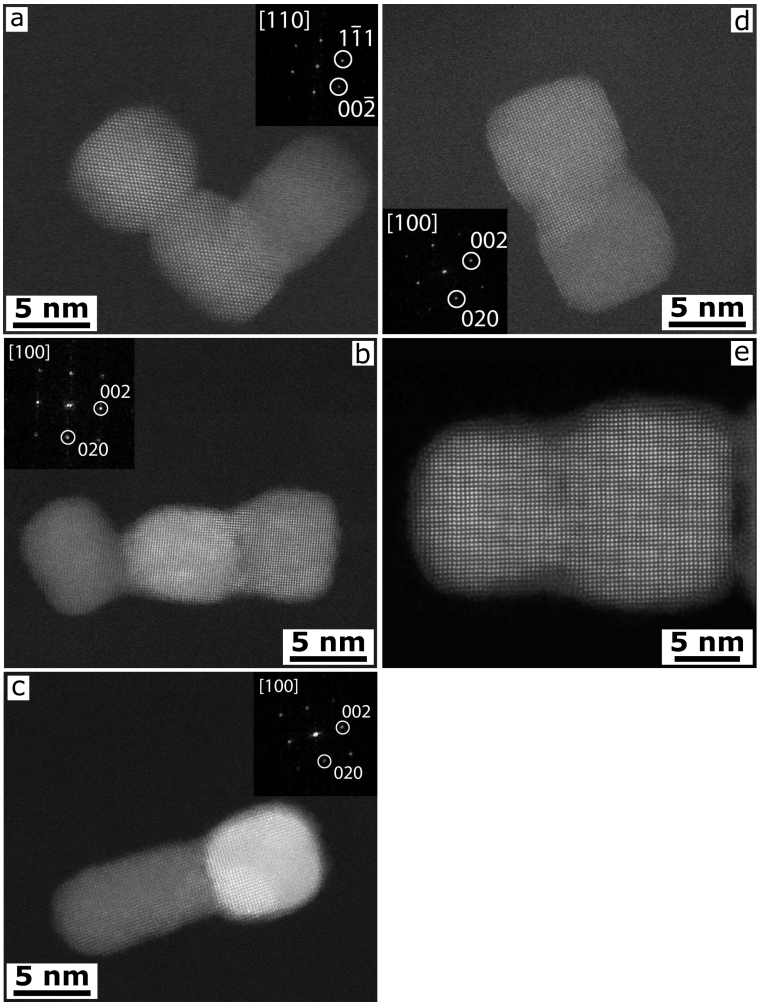

Figure 3.7: HAADF-STEM images in (a), (b), (c), (d), and (e) showing epitaxial connections at the interface of cubes as a result of $NaBH_4$ treatment. The cubes in (a) are oriented along a <110> direction on the Si_3N_4 grid but are epitaxially connected along a {100} facet.

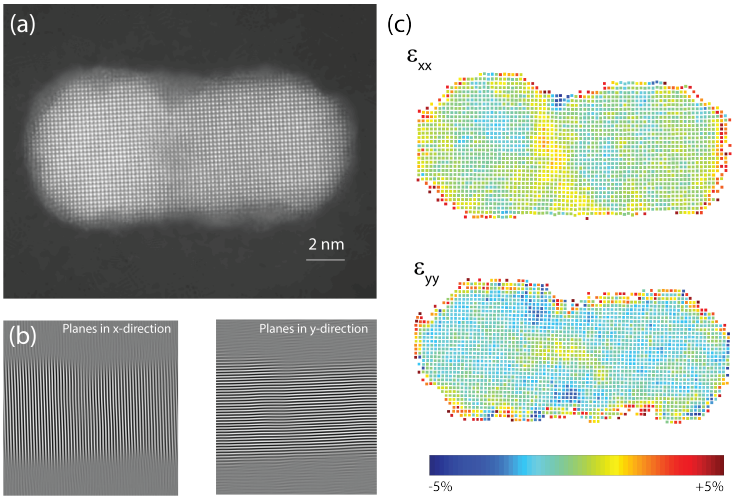

Figure 3.8: Dislocation and strain analysis of 2 epitaxial cubes with no dislocation (a) HAADF-STEM image of the epitaxial cubes (b) Inverse Fourier transform images showing the individual planes along the x and y directions respectively, illustrating the absence of any dislocation. (c) Strain maps computed for x and y directions.

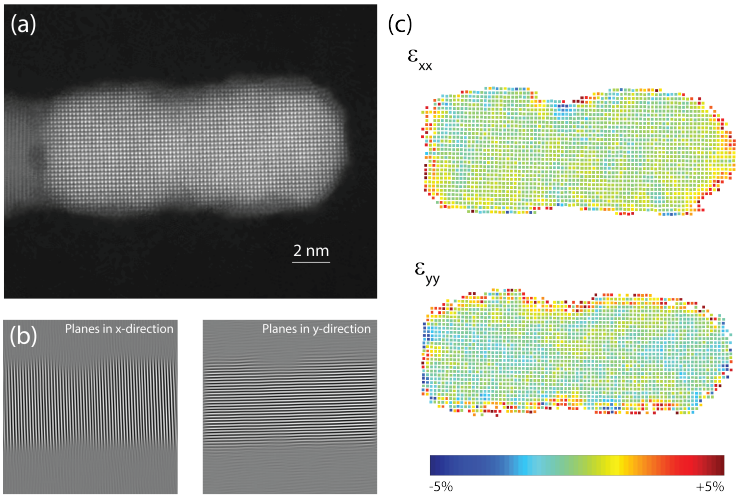

Figure 3.9: Dislocation and strain analysis of 2 epitaxial cubes with no dislocation (a) HAADF-STEM image of the epitaxial cubes (b) Inverse Fourier transform images showing the individual planes along the x and y directions respectively, illustrating the absence of any dislocation. (c) Strain maps computed for x and y directions.

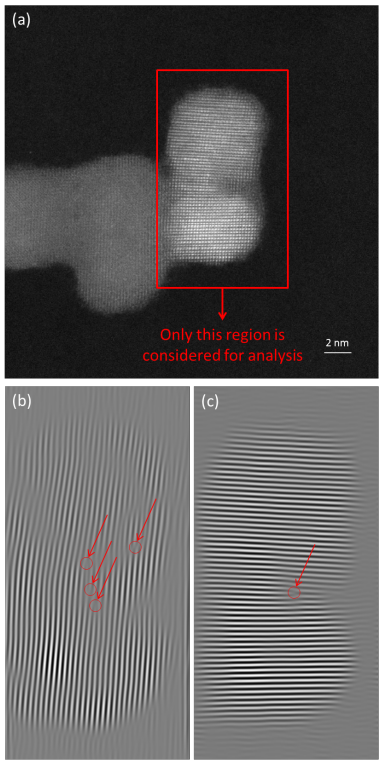

Figure 3.10: Illustration of the presence of different dislocations for large angular misalignment (4°) of the epitaxial cubes. (a) Shows the HAADF-STEM image of the epitaxial cubes. (b) and (c) Inverse Fourier transform images showing the individual planes along the x and y directions respectively, illustrating the presence of 5 dislocations at the interface of cubes, indicated by the red arrows.

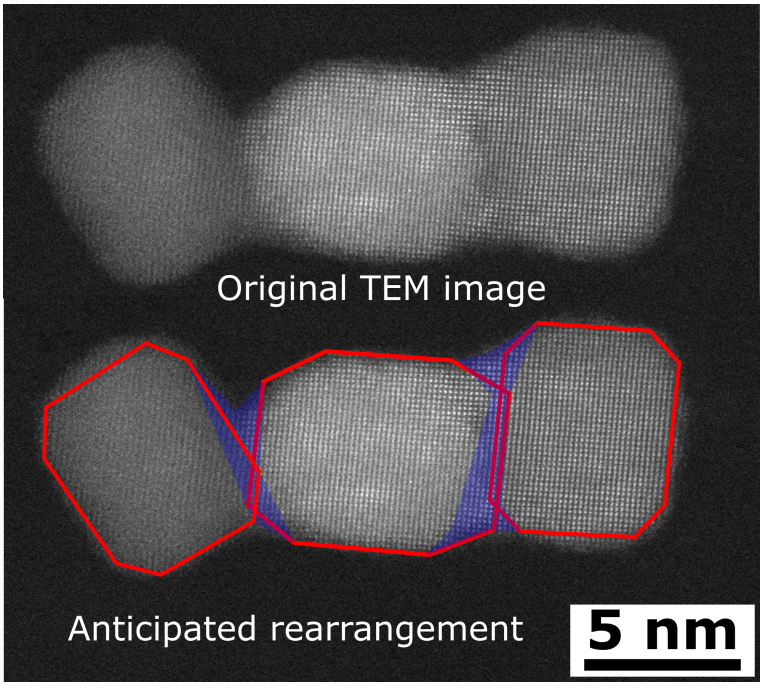

Figure 3.11: Local movement of atoms during ligand removal and epitaxy. Upper panel shows the original HRTEM image of the epitaxial cubes. The lower panel represents the qualitative anticipated outline of the cubes with orientation in red and the filled blue area represents the tentative area of atom rearrangement.

4

SOLUTION OVERGROWN PATTERNED CRYSTALS: FROM THE FUNDAMENTAL AND TECHNOLOGICAL ANGLE

A linear combination of nanocube imprint lithography and solution overgrowth can yield patterned continuous crystals and even single crystals without strain or dislocations with proper alignment. Imprint lithography contributes toward the rapid patterning of colloidal particles in various shapes. At the same time, solution growth brings in the capability of non-destructively and chemically adding the material of choice in the nanogaps (between particles), possibly at low temperatures. Also, we use nanocubes as the preferred morphology of the building blocks to make patterns via assembly and overgrowth. Thus, here is a viewpoint showing that crystals fabricated with such an implementation hold future opportunities for fundamental science as well as technological impact.

4.1. Introduction

Single crystals hold the potential to realize the ultimate performance of materials. The absence of grain boundaries in a crystal can significantly influence optical, mechanical, and electrical properties [198, 199]. The bottom-up assembly of nanocubes followed by epitaxial attachment is a cheap and straightforward way to fabricate single crystals, which is already demonstrated [75, 92]. Here, building on the previous works, we would like to take a more systematic approach to construct crystals by solution overgrowth. For example, chapter 2 demonstrates the idea of large-scale patterning, which can be explored further to make technologically relevant transparent conductors. Simultaneously, the successful fabrication of curved single crystals via nanocube-oriented assembly and chemical overgrowth gives rise to several fascinating fundamental questions.

It is possible to make a nanosized perfect single crystal because of the identical (100) faces of a nanocube (chapter 3), and it would be interesting to determine how close to "perfect metal" can be reached with this technique on a large area. One could also wonder what are the limits to reaching curved single crystals with such a method. In other words, at what radius of curvature grain boundaries start appearing. Chapter 3 already made a first step in this direction by looking at Pd nanocubes assembled and epitaxially connected with varying degrees of angular misalignment. However, the angular misalignment was not controlled in that study, making it impossible to determine a precise threshold for grain boundary formation. Fabricating crystals with variable and controlled radius of curvature is the next step needed to determine the balance between strain and grain boundary formation at the nanoscale. Here we show that Ag or Au's solution overgrowth on top of Ag cubes patterned in curves yields curved crystals with variable curvature. Making micro and nano (curved) crystals via overgrowth of assembled cubes is facile, robust and can be achieved at room temperature, as demonstrated in this work. Also, the results presented here are the preliminary stepping-stones needed to address the diverse questions posed above.

Crystal fabrication by nanocube assembly and overgrowth not only opens up in-

triguing scientific questions but also holds prospects for immediate industrial attention. One of the most common and simple devices benefiting from nanopatterning and relevant for technological applications is an optically transparent electrode [200]. Metal nanowires, for example, in the form of meshes, gratings, or hexagonal patterns, made from a highly conducting material like Au, Ag, or Cu are laid on a substrate to collect/deliver electrons in the devices. The geometric fraction of free space between the metal lines largely dictates the amount of light entering or leaving the device, highly relevant for solar cells and light-emitting diodes. While random nanowire meshes have already shown great promise [65, 70, 72], designed nanopatterns can provide multifunctional properties, for example, by increasing light coupling into specific waveguiding modes [201, 202] or controlling the angular or spectral content of reflected or emitted light [203, 204]. Both the conductivity and transmission form important figures of merit to assess the electrode's overall quality; however, these additional functions add something new to the very large body of work on random nanowire mesh transparent electrodes, while maintaining the advantages of simple, scalable, and low-temperature solution processing. Our group's previously published work showed that the epitaxial solution overgrowth of assembled Ag cubes could yield a single crystal nanowire [75]. Notably, their electrical performance is comparable to that of bulk Ag. Here, it is demonstrated that the patterned cubes can be locally grown into continuous 2D designs, like grids, on an arbitrary substrate and at low temperatures. It is further shown that the networks can be used as an optically transparent electrode. The grids with a measured pitch of 4.1 μm and 250 nm linewidth bore a sheet resistance of 110 $\Omega.\text{sq}^{-1}$ and an upper bound transmission of 89%.

4.2. Results and discussion

Micro and nanoparticles assembled on a chip to engineer patterned functional devices is an attractive research direction. We use nanocubes and an elastomeric stamp for making patterns on a substrate. Figure 4.1 shows a schematic of the process described in this chapter. Briefly, the nanocubes ink is dried to form a resist film on the desired

substrate. This thin film is rewetted with a solvent and a soft template imprints patterns in the resist. Refer to chapter 2 for complete printing details.

Once the patterns are printed, depending on the application, the patterned assemblies of cubes can be used as it is or need to be connected. For example, metamaterials or single-particle lattices find diverse applications in plasmonics like Raman spectroscopy or lattice resonances [35, 205]. While making robust macrocrystals or applications demanding high electrical conductivity, we need an uninterrupted connection between adjacent particles in the patterns [65]. For joining adjacent building blocks like nanoparticles or nanowires, diffusion of atoms triggered by thermal, optical, or plasma treatment is commonly used [67, 70]. Mechanical pressing to merge a random network of wires has also been reported [206]. In all these techniques, the amount of material before and after making the connections is practically constant and mostly relies on the local rearrangement of the atoms. In contrast, we explore the idea of solution deposition of extra material from outside in the nanogaps between adjacent cubes to form continuous structures, as shown in Figure 4.1-c,e. This additional material is in the form of atoms generated by reducing a salt precursor in solution. Thus, we overgrow the cubes in solution by depositing atoms on the predefined assemblies of cubes on the substrate to yield continuous patterns, as illustrated in Figure 4.1d.

Monocrystalline 75 nm Ag cubes, as shown in the electron microscopy image of Figure 4.4, are used as the primary building blocks for making patterns on various

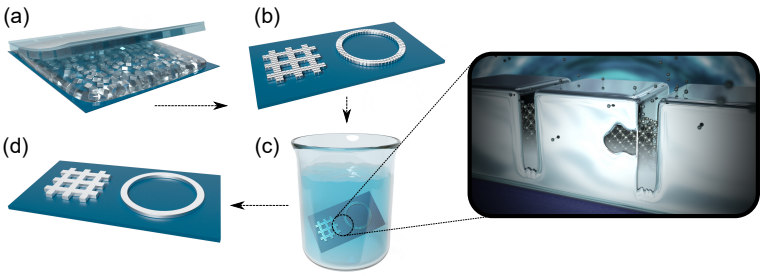

Figure 4.1: Schematic illustration of the process. (a) Imprinting on a substrate from a nanocube resist. (b) Imprinted patterns. (c) Solution overgrowth. (d) Overgrown patterns on a substrate. (e) An insight into the overgrowth mechanism. Image modified from references [75, 91]

substrates like silicon and quartz. The cubes are synthesized in solution, which results in atomically smooth and well-defined {100} faces. They are covered with a layer of polyvinylpyrrolidone (PVP) during synthesis that dictates the shape as well as protects the colloidal nature of nanocubes in solution. For bridging the adjacent cubes, the first step after printing is to strip the faces of the PVP coating; otherwise, it can hinder the external deposition of atoms during growth. Previously, it has been shown that PVP can be effectively removed from the cube's surfaces sitting on a substrate by treatment with aqueous $NaBH_4$ solution [75, 92]. Here, we use UV-ozone treatment to achieve the same. Since it is a gaseous treatment, it is a faster alternative and free from any deposition of impurities or a possible disruption of patterns from the solvent. The patterned substrate is placed in a conditioned chamber for ozone plasma treatment for burning the ligands and then immediately dipped in a vial containing the overgrowth solution (Figure 4.1c).

The overgrowth solution serves as the medium containing the precursors for material used for making the bridge between cubes. We use a mixture of Tollen's reagent and glucose. It is commonly referred to as the silver mirror reaction in which the diaminesilver(I) complex serves as a precursor for Ag and glucose as the reducing agent. The aldehyde group in glucose is oxidized and reduces the complex to generate the Ag atoms in solution. The concentration of reactants is kept minimal to preclude homogeneous nucleation of Ag as far as possible. As a result, the monocrystalline Ag cubes previously printed on the substrate, act as seeds for guiding the newly born Ag atoms for homoepitaxial overgrowth. Over time, the deposition of adatoms will result in the gradual disappearance of the gaps between adjacent cubes and eventually lead to connected patterned crystals made by the bottom-up assembly of nanocubes and chemical overgrowth (Figure 4.1d). This whole process is carried out at room temperature. Overgrown patterns are subjected to rapid thermal annealing (RTA) treatment in an Ar atmosphere (refer SI for details), which helps relax any residual stresses accrued in the structures during localized welding.

Figure 4.2 shows the curved crystals made by the aforementioned assembly and

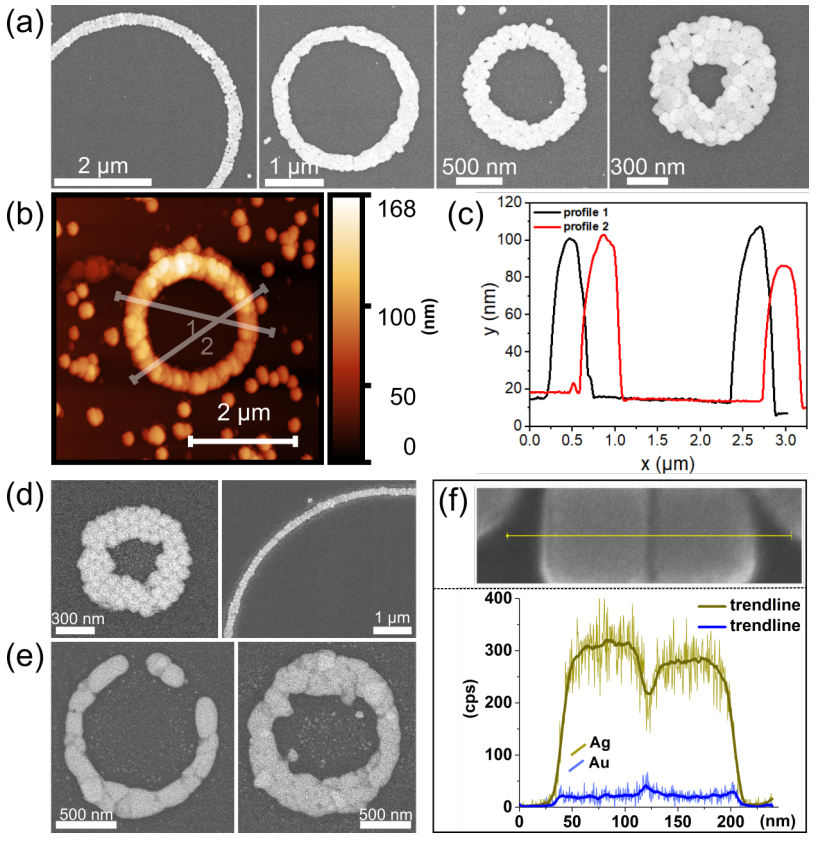

Figure 4.2: Curved patterns made by nanocube assembly and solution overgrowth. (a) SEM backscatter electron images of overgrown and annealed Ag on Ag cubes patterned with different radii of curvature. (b) AFM scan of an Ag deposited on Ag ring and the corresponding (c) height profile. BSE images of Au overgrown on patterned Ag cubes (d) without annealing and (e) after annealing. (f) EDS line scan confirming the presence of Au on top of Ag cubes.

solution overgrowth process. It is possible to fabricate curves of different radii of curvature and we have demonstrated as small as 300 nm. Figure 4.2a shows the backscattered electron (BSE) images of the patterns made by Ag overgrowth. It reveals that the adjacent faces of the cubes are merged with an occasional occurrence of a void. The corresponding secondary electrons (SE) images revealing the surface morphology of the patterns are shown in Figure 4.5. Also, there is no apparent sign of substantial homogeneous nucleation near structures. The AFM scan reveals that the average height of the welded curves is around 100 nm, as shown in Figure 4.2b,c.

After welding, the overall morphology of the patterns is retained. It is an advantage of solution overgrowth compared to techniques that rely on a local rearrangement of atoms as that can lead to shrinkage, cracks, or can even hurt patterning. Moreover, the functional (optical) performance of a device can vary depending on the environment or substrate [207, 208]. The patterning and the solution overgrowth depend mainly on the nanocube materials, so it could be worked out on several support layers.

Solution deposition has an extra advantage. It lets localized addition of even other materials (different than primary cube) with different properties on top of assembled cubes paving the way for creating a natural superlattice (heteroepitaxial core-shell multicomponent structures). As an example, Figure 4.2d,e shows BSE images of the curves made by the assembly of Ag cubes, and subsequently, Au is grown on top of the patterns in solution (SE images are shown in Figure 4.6a,b). The energy dispersive spectroscopy (EDS) line scan shown in Figure 4.2f confirms the presence of the Au layer on top of Ag cubes with pronounced Au peaks at the edges and the interface of cubes. A superimposed image of Au and Ag EDS color mapping is shown in Figure 4.6c,d. For Au growth, we followed a simple published recipe that showed galvanic replacement-free deposition of Au on Ag cubes [209]. Similarly, literature is replete with reports on the formation of hybrid nanostructures by overgrowth for many materials. For example, Pd on Pt and vice versa; Ag, Pt, and Pd on Au; Au on Ni; Cu on Pd; CdSe on CdS or CsZnS; PbSe on Cu_2Se; PbTe on CdTe; CdS on Au or Pt; PbS on Au [87, 88]. As a result, it is possible to imagine cheap and sophisticated 3D patterns/devices entirely processed from solution by colloidal synthesis, bottom-up assembly, and subsequent overgrowth of various materials. Such structures could pose a significant challenge if fabricated by pure top-down approaches.

From a lab to an industry perspective, we assembled the Ag cubes in grid patterns and then overgrew in solution via the silver mirror reaction to yield continuous networks, as shown in Figure 4.3a,b. Figure 4.3a shows the optical images of the printed grids with different pitches on a quartz substrate. Figure 4.3b shows the SE images of the connected cubes in the assembled grids on a Si substrate (BSE image are shown

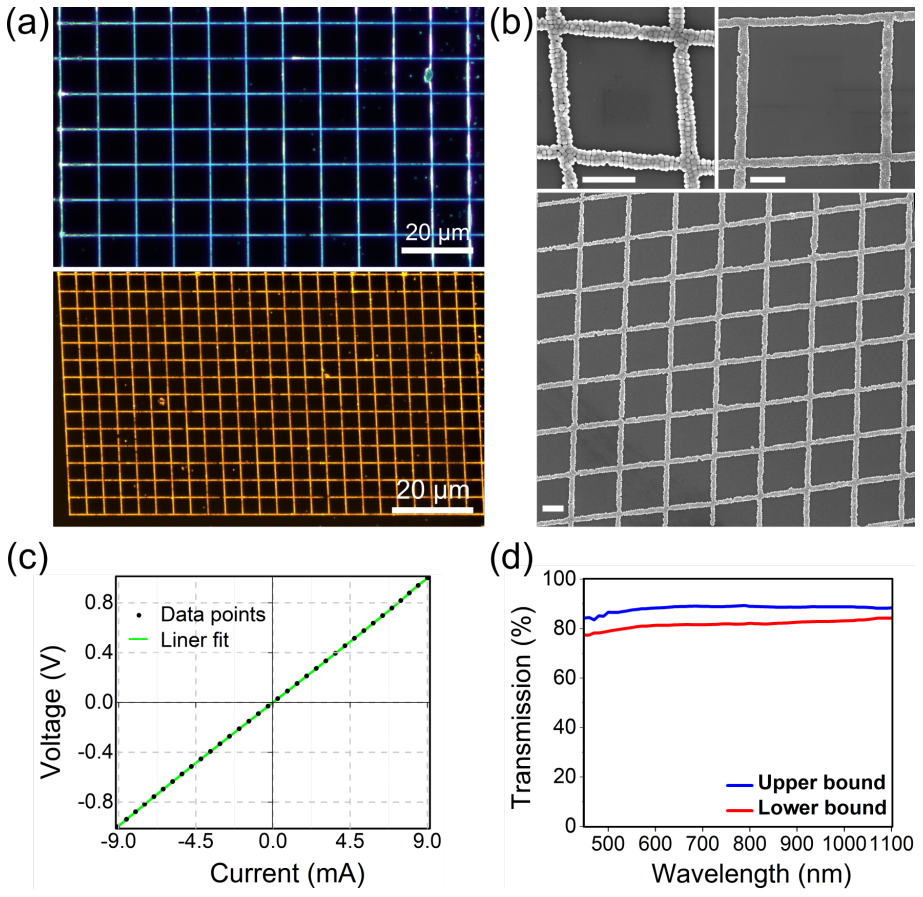

Figure 4.3: (a) Optical images of the printed grids on a quartz substrate. (b) SEM images of the large networks with Ag printed on a Si substrate. The scale bars are 1 µm in length. (c) I-V curve of a grid with a 4.1 µm pitch and 250 nm line width. (d) Transmission with respect to the wavelength of the same grid measured in (c).

in Figure 4.7a). Subsequently, Ag contacts are deposited on the opposite edges of the grids fabricated on the quartz substrate to measure the electrical performance of the grids (refer SI for details). A measured current-voltage (IV) curve is shown in Figure 4.3c. It exhibits the expected ohmic behavior confirming the successful fabrication of connected networks with a sheet resistance of 110 $\Omega.sq^{-1}$. For the same grid, Figure 4.3d depicts the lower and upper limits of optical transmission with a value of 81% and 89%, respectively at 650 nm. The actual average pitch, width, and cross-section

area of the printed crossed-lines were determined from the AFM scan shown in Figure 4.7b. Using those values, the calculated sheet resistance is about 2.5 $\Omega.sq^{-1}$ and the geometrical transmission is about 88%. The sheet resistance and optical transmission can be reduced and enhanced, respectively, for example, by making taller patterns with a reduced linewidth. There is a scope for improvement. Nonetheless, the results prove that it is possible to create devices by assembly and overgrowth of nanocubes entirely from solution, at low temperature, in a cheap way, on variable substrates, and perhaps with high-throughput.

4.3. Conclusions

It is shown that crystals with shapes like a curve and straight line can be fabricated using the patterned assembly of nanocubes and subsequent chemical overgrowth in solution. The process, for the most part, does not require a cleanroom, high vacuum or temperature, extremely expensive or specialized tools and has the potential to be engineered in series on an assembly line. The curves assembled with Ag nanocubes were overgrown into continuously connected crystals with either Ag or Au. BSE SEM images confirmed the connections formed between adjacent cubes as well as EDS line scans and color maps confirmed the presence of Au. It would be an exciting endeavor to grow curved 'single' crystals with the proposed technique. The patterns assembled in straight lines were translated into transparent conductors relevant for optoelectronics. The alignment between adjacent cubes is not always ideal or perfect and there are some voids in structures after overgrowth. While there is room for improvement, the preliminary results indicate a successful implementation of the concept of nanocubes assembly and growth in solution to make technologically significant devices like optically transparent electrodes.

4.4. Supporting information

4.4.1. Chemicals

Ascorbic acid (AA); silver nitrate ($AgNO_3$); potassium hydroxide (KOH); ammonium hydroxide (NH_4OH); glucose; chloroauric acid ($HAuCl_4$); polyvinylpyrrolidone (average MW 55000 g/mol); 1,1,1,3,3,3-Hexamethyldisilazane (HMDS); mili-Q water (resistivity – 18 MΩ.cm at 25 °C); tetramethylammonium hydroxide solution (TMAH) - 25 wt. % in water. All the chemicals were purchased from Sigma Aldrich unless stated otherwise and used as received.

4.4.2. Imprinting

Refer chapter 2 for the synthesis of Ag nanocubes; Si master fabrication; PDMS stamp making; printing experiments.

4.4.3. Overgrowth of Ag on Ag cubes

1. Preparation of the welding reagent **(A)**: Weigh 0.815 g of $AgNO_3$ and dissolve in 20 mL of mili-Q water. $AgNO_3$ is sensitive to light exposure, so it is recommended to shield the vial from light by aluminum foil. Stir the solution at 400 RPM for ~20 min. It results in a clear, colorless solution. Next, add 40 µL of 0.25M KOH in the same vial, and immediately after the addition, the solution gives brown colored precipitates of Ag_2O. Let the bottle sit overnight to make sure the precipitation is complete. To this solution, very slowly, add 1.3 mL NH_4OH dropwise. On the first addition, the solution will turn turbid brown. On further addition, it will turn into dark brown and then slowly will break the continuous color to become colorless finally. Stir the solution at 400 RPM for the whole time during the addition of NH_4OH. This process takes about an hour.

2. Preparation of the reducing agent **(B)**: Dissolve 1.71 g of glucose in 5 mL of mili-Q water.

3. Ligand removal from cubes: The UV-ozone chamber is conditioned by running empty for 120 s. Then the patterned substrate is treated in the chamber for another 60 s.

4. Overgrowth of the cubes: A vial is prepared with 5 µL of **(A)** diluted with 3 mL of water in a 5 mL glass vial. To this, add 2.5 µL of **(B)** and vortex it for 5 s. Prepare this solution while treating the substrate with ozone, and immediately after withdrawing, add the substrate to this solution. Let it stand for 10 - 60 min. The solution remains colorless throughout the welding time. Finally, withdraw the substrate and add it to the vial of fresh water. After 60 s, remove the substrate and gently blow-dry.

4.4.4. Overgrowth of Au on Ag cubes

Prepare 2 mL PVP (1 mM) in a 20 mL vial and add 0.5 mL (100 mM) AA to it and stir the solution at 150 RPM. Add 0.5 mL (200 mM) NaOH to the vial. Suspend the patterned substrate in the vial and quickly add 20 µL of $HAuCl_4$ to the mixture and let it stand for 60 min. Finally, withdraw the substrate and dip it in fresh water for 60 s and gently blow dry it.

4.4.5. Annealing

Rapid thermal annealing of the overgrown samples is performed in the Sitesa addax RM6 chamber. The substrate is placed on 2 (for quartz) or 3 (for Si) regular 1 mm microscopy glass slides on a 4" Si wafer susceptor. The chamber is purged with Ar at the rate of 5 L/min for 60 s. Then the heating lamp is switched on for 8 s while the Ar is still in circulation. The temperature setpoint is 600 °C; however, the pyrometer is not accurate below 600 °C and the temperature measured on the silicon susceptor is likely very different from what is reached at the nanowire surface. Post-annealing, the Ar assists in the cooling of the substrate and the carrier wafer.

4.4.6. Fabrication of Ag contact pads on Ag grids

The grid patterns are printed on a quartz substrate for making electrodes. To measure the resistance of the Ag network, Ag contacts are deposited at opposite ends of the grids by photolithography. The substrate is spincoated (4000 rpm, 1000 rpm/s, 45 s, closed bowl) with HMDS followed by baking at 150 °C for 60 s. HMDS serves as an adhesion layer for the photoresist. Next, Ma-N1420 is spincoated (2500 rpm, 500 rpm/s, 45 s, open bowl) followed by baking at 100 °C for 120 s. The substrate is exposed to UV light through a custom Cr on a quartz mask for 18 s at 25 mW/cm^2 with a total power of 450 mJ/cm^2. Subsequently, the substrate is developed in ma-D 533S (micro resist technology) for 90 s followed by rinsing in fresh water and N_2 blow drying. This opens a window of 200 x 200 μm^2 in the resist layer with an overlap of 25 μm on both sides of the welded grid. 5 nm Cr (0.03 nm/s) layer followed by 150 nm Ag (0.2 nm/s) thin film is deposited on the substrate by electron beam physical vapor deposition (Polyteknik Flextura M508 E) under high vacuum. Finally, a lift-off procedure is performed in acetone at RT overnight to dissolve the resist. A final agitation is necessary to remove the excess Ag to reveal the grids with Ag contacts on the substrate.

4.4.7. Sheet resistance measurements

A probe station with a source/measurement unit B2902a (Agilent) is used to measure the sheet resistance of the grids. Two tungsten needles are gently brought in contact with the Ag pads. A voltage sweep is run from -1 to 1 V and the current is measured. It results in an IV curve and the slope of the line yields the sheet resistance of the grid.

4.4.8. Transmission measurements

The transmission of the grid as a function of the wavelength is measured using a photodetector, an integrating sphere, and a Fianium laser as the light source using a home-built setup [210]. A lower and upper limit of the transmission is presented due to

practical limitations in the setup. For the lower bound measurement, the photodetector is placed carefully behind the sample, such that all the directly transmitted and some of the forward scattered light is collected. This measurement is regarded as the lower bound as part of forward scattered light was not collected by the detector. For the upper bound analysis, the grid is placed inside an integrating sphere. In this case, all the directly transmitted and forward scattered light is collected, but also some of the backscattered light is collected with the integrating sphere. As a result, this measurement represents the upper bound of light transmission. The actual transmission must lie within these limits. A clean quartz substrate is used for the reference measurements.

4.4.9. Supplementary figures

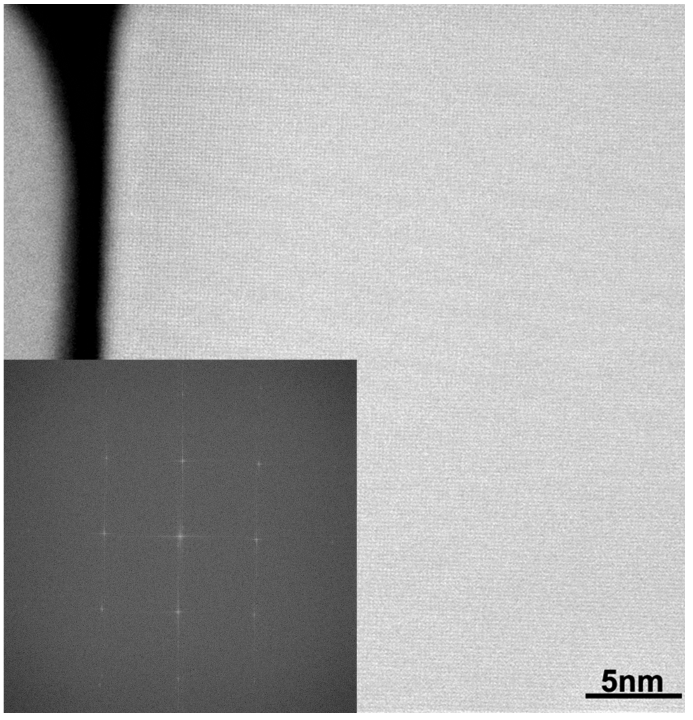

Figure 4.4: Transmission electron microscopy image of a Ag nanocube. The inset depicts the FFT of the cube.

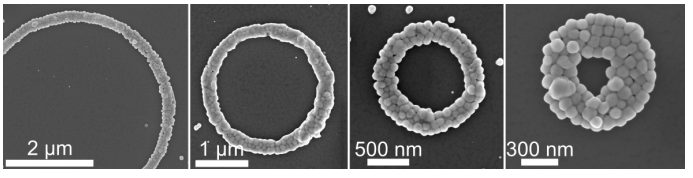

Figure 4.5: SEM (secondary electron) images of patterns with Ag overgrowth on assembled Ag cubes.

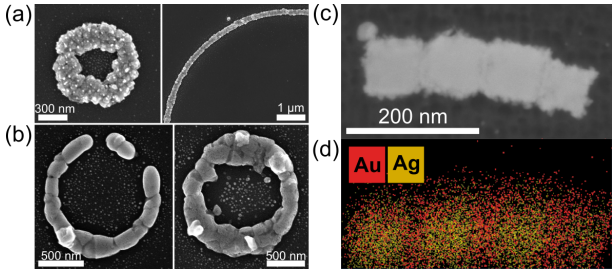

Figure 4.6: Backscatter electron images of Au overgrown on patterned Ag cubes (a) without annealing and (b) after annealing. (c) STEM image of Ag cubes overgrown with Au and the corresponding (d) EDS layered image of different elements.

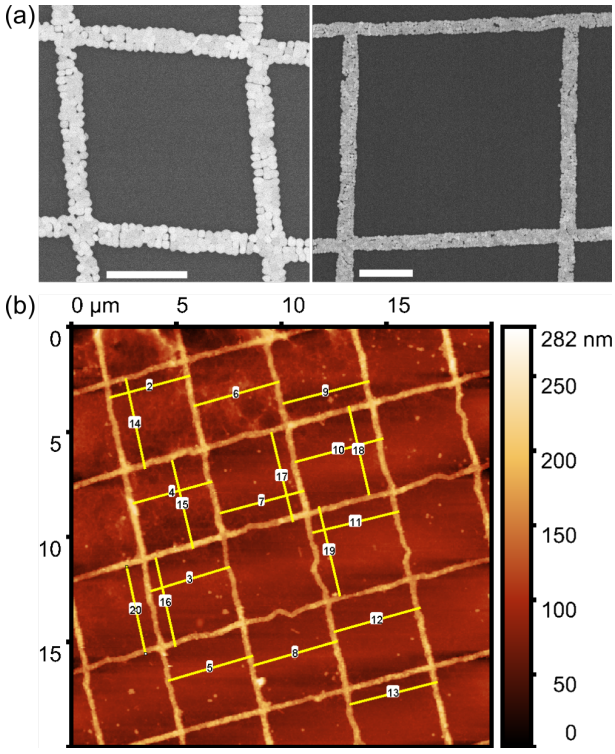

Figure 4.7: (a) Backscatter electron images of the overgrown grids with Ag printed on a Si substrate. (b) AFM scan of a grid printed on a quartz substrate used for the calculation of average pitch and cross-section area of the patterns.

5

CLOSE-PACKED ULTRASMOOTH SELF-ASSEMBLED MONOLAYER OF PEROVSKITE NANOCUBES

The use of colloidal self-assembly to form complex multiscale patterns in many optoelectronic devices has been a long-standing dream of the nanoscience community. While great progress has been made using charged colloids in polar solvents, controlled assembly from nonpolar solvents is much more challenging. The major challenge is colloidal clustering caused by strong van der Waals (vdW) attraction between long-chain surface capping ligands passivating the surface of nanocrystals. Such clustering degrades ordering in packing during the self-assembly process. While ligand exchange to provide colloidal stability in polar phases is often an option, this is not the case for the exciting new class of halide perovskites due to the material's solubility in essentially all polar solvents. Here, we report surface-functionalized self-assembly of luminescent $CsPbBr_3$ perovskite nanocubes by partially replacing long-chain oleyl groups (18 carbon chain) with short-chain thiocyanate (SCN^-). This enables the fabrication of ultrasmooth monolayer thin films of nanocubes with a root-mean-square (RMS) roughness of around 4 Å. This ultrasmooth large area self-assembled layer could act as high-efficiency optoelectronic devices like solar cells, light-emitting diodes (LEDs), transistors, etc. We correlate our experimental results with simulations showing reduced free energy for cubes grafted with short-chain thiocyanate compared to long-chain oleyl groups, thus facilitating better self-assembly.

5.1. Introduction

Self-assembly of nanomaterials to form complex 2D and 3D patterns with control from nanometer to centimeter length scale has been a longstanding challenge for the nanoscience community [33, 168, 211–215]. The prospect of engineering complex functional devices by simple wet chemistry and self-assembly has largely been inspired by nature, where hierarchical ordering and reproducible complex pattern formation are achieved at or near room temperature in an aqueous environment [7, 216]. Although there has been tremendous progress in bioinspired and colloidal self-assembly, most work has been conducted either in polar solvents with charged colloids [212] or at the interface between polar and nonpolar solvents [217]. In polar solvents, surface charges on nanoparticles provide excellent colloidal stability ensuring facile monolayer 2D [170, 218] and 3D [212] self-assembly and patterning via capillary assembly [37] or electrophoretic deposition [44]. In nonpolar solvents, they can be stabilized using soluble organic surface capping ligands [219] and self-assembly proceeds, for example, via solvent evaporation [29, 172, 213, 220–223] and nanoimprinting [124]. However, the colloidal aggregation due to strong van der Waals (vdW) interactions [224, 225] between organic chains prevents controlled assembly into single-crystalline monolayers. The role of capping ligands therefore is not only to ensure stability but also to guide self-assembly into ordered or disordered structures.

There is an emerging class of materials, namely the halide perovskite nanocrystals [226–228], which has outstanding optoelectronic properties. The most stable inorganic perovskite $CsPbBr_3$ nanostructures [136, 153, 226, 229–231] are stabilized by long-chain oleyl groups as surface capping ligands. Nanocubes of $CsPbBr_3$ have a tendency to fuse into single crystals [173, 232–234], making them ideally suited for a self-assembled thin film and luminescent nanopatterned devices. However, the major problem behind their self-assembly is that due to their ionic nature they readily dissolve in a polar environment, while in a nonpolar solvent, they have a tendency to cluster [235] due to strong vdW attractions between the long capping ligands. Therefore, preventing colloidal aggregation to enable close-packed monolayer thin films

remains an open challenge. Here, we demonstrate that besides improving the optical quality [236], short-chain thiocyanate ligands also lead to a substantial reduction in cube-cube interactions, greatly improving self-assembly. This enables the formation of monolayer thin films with root-mean-square (RMS) roughness of 4 Å.

5.2. Results and discussion

We synthesize monodisperse $CsPbBr_3$ nanocubes using a modified literature report [136] and perform surface modification to achieve better control in self-assembly. In short, lead bromide ($PbBr_2$), octadecene (ODE), oleic acid (OAc) and oleylamine (OAm) are heated at 200 °C in a three-necked round bottom flask. Cesium oleate is injected and 5 seconds after the injection the temperature is decreased to 160 °C.

The reaction mixture is then annealed at 160 °C for 10 min. Annealing at this stage is essential to obtain monodispersed cubes with sharp facets, which is crucial for a long-range, defect-free, and close-packed ordering of cubes. After that, long-chain oleyl groups on the nanocube surfaces are partially exchanged with shorter chain thiocyanate. The thiocyanate capped cubes dispersed in toluene are dropcast

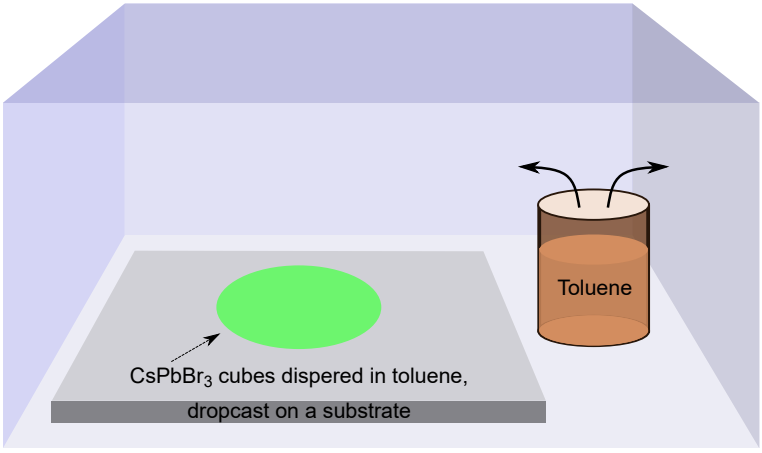

Figure 5.1: Schematic presentation of droplet evaporation perfomed in a closed chamber to get a closed-pack self-assembled monolayer.

on a silicon (Si) substrate, with slow evaporation of toluene (Figure 5.1) leading to a beautiful monolayer assembly of cubes with uniform packing, as shown in Figure 5.2a.

A low resolution SEM image of the film is shown in Figure 5.2b (also in Figure 5.5) showing large area continuous assembly on a Si substrate. The assembled layer is truly a monolayer shown in Figure 5.6 observed from the fact that the cleaning procedure (gently rinse one time with methyl acetate solution) used to avoid charging effects during SEM led to partial delamination in a few places. The AFM images in Figure 5.2-c,d reveal that the surface of assembled monolayer is ultra-smooth, with measured RMS roughness of 4 Å. The surface of the nanocubes is atomically flat; the 4 Å roughness can be attributed to residual ligands crystallized on the surface after solvent evaporation and size dispersion of the nanocubes. Assemblies of the as-synthesized (without thiocyanate exchange) cubes result in short-ranged domains,

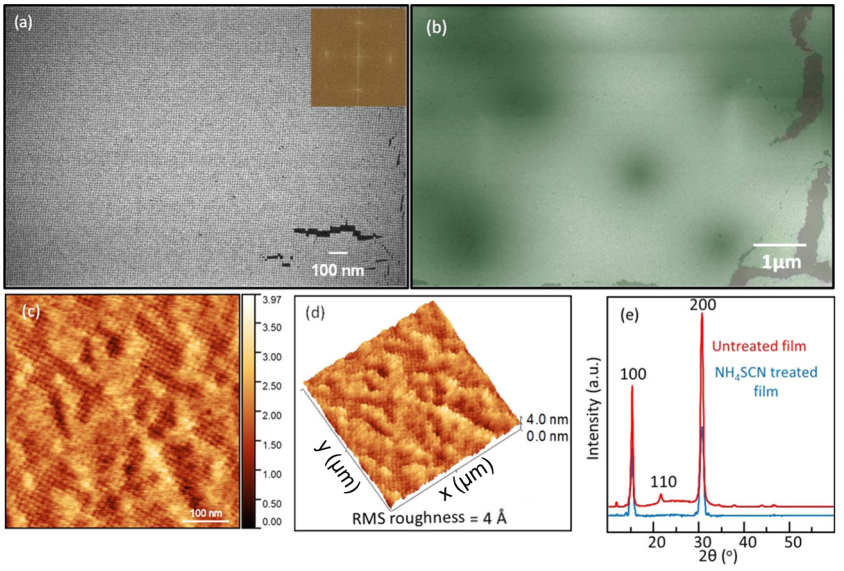

Figure 5.2: (a) High-resolution SEM image of the monolayer; inset of (a) shows FFT pattern of the monolayer film. (b) Low-resolution SEM image of the nanocube monolayer. Light green false color is used in the SEM image to indicate the nanocube monolayer on Si (black area). (c) Atomic force microscopy (AFM) image of a monolayer film. (d) 3D view of the area in (c) and measured RMS roughness value. (e) X-ray diffraction (XRD) pattern of monolayer (NH_4SCN treated film) and multilayer (untreated with NH_4SCN) nanocube assembly.

mostly with multilayer stacking, as shown in Figure 5.7. Quantitative measurement of the height profile from AFM of different layers stacking is shown in Figure 5.8. We have analyzed the crystallographic orientation of close-packed monolayer films and multilayer stacked films using XRD, presented in Figure 5.2e. In both cases, the peak corresponding to the [100] direction is the strongest, but thiocyanate capped nanocube films only have [100] and its equivalent peak contributions which can be attributed to the fact that these cubes are aligned along the same [100] crystallographic orientations to form a close-packed film. This is also clear from the SEM images where even before ligand exchange (Figure 5.7) there is reasonably good ordering, though often multilayers rather than monolayers, which prevent perfect ordering. This imperfect ordering leads to the substantial 110 reflection shown in the untreated sample (Figure 5.2e), which is absent after thiocyanate exchange, demonstrating the improved assembly and perfect orientation.

Although exchanging the long chain ligands with thiocyanate improves the assembly in the large area monolayer case, one concern with such postsynthetic ligand exchange is always the accompanying changes in material properties [237–239]. The absorption and photoluminescence (PL) spectra of $CsPbBr_3$ are identical before and after treatment (Figure 5.9). However, a significant increase in the PL quantum yield (PLQY) from 72.9% to 90.9% is observed after thiocyanate treatment, which is consistent with the literature [236]. Thiocyanate is not completely soluble in toluene but partially interacts with the surface of the cubes forming Cs/Pb-SCN bonds [237] which

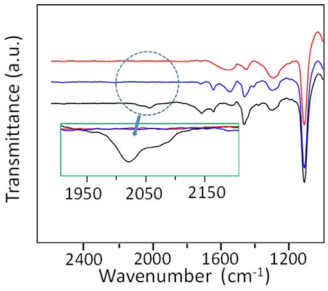

Figure 5.3: FTIR spectra of bare silicon (red), without thiocyanate treatment (blue) and thiocyanate treated $CsPbBr_3$ nanocubes (black).

is confirmed by Fourier Transform Infrared Spectroscopy (FTIR) spectroscopy shown in Figure 5.3. The inset of Figure 5.3 shows a broad peak around 2060 cm^{-1} which represents C≡N vibrational mode of SCN. This clearly indicates that thiocyanate binds at the surface of nanocubes and replaces some of the long hydrocarbon chains from the surface of the cubes which is essentially the key factor for the controlled self-assembly.

We compute the free energy of assembly for a 4 x 4 two dimensional square lattice with variable lattice constant (a_{nn}) and cube size ranging from 13 unit cells (N13-7.63 nm cube edge length) to 2 unit cells (N2-1.17 nm cube edge length) following previous methods [224]. Thiocyanate shows a slightly weaker attraction compared to oleyl chains for N13, as shown in Figure 5.4. The same trends are also observed for N11, N9, N7 and N2 (not shown). In equilibrium, the system is dry (free of any toluene), and the minimum bonding free energy results from a competition between the attractive enthalpic vdW attraction and the repulsive entropic chain packing. The bonding free energy is 40% stronger with oleyl chains than with thiocyanate (-1514k_BT vs. -920k_BT for 7.63 nm cube). In both cases the strong attractive forces are holding the cubes together. This points to a finer assembly control as the thiocyanate nanocubes only get pulled together strongly when they are already close to the proper orientation for ideal packing, whereas the former starts to have strong long range attractive interactions for less ideal binding configurations. This is related to the strength of the vdW forces that increase very significantly with larger chains, leading

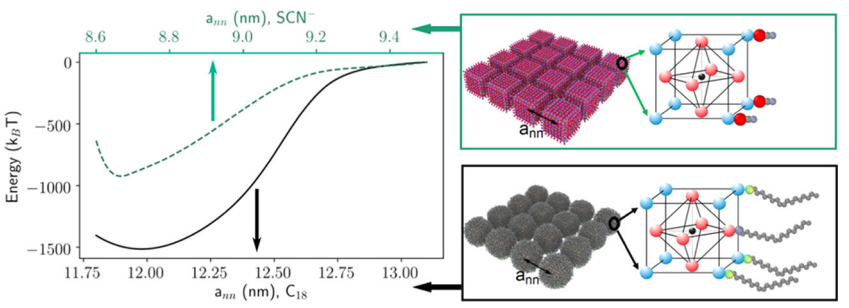

Figure 5.4: Free energy plots of N13 perovskite nanocubes grafted with long oleyl chains and thiocyanate. For oleyl chains, equilibrium distance (r_0) = 11.79 nm, minimum bonding free energy (F_0) = -1514k_BT while for thiocyanate r_0 = 8.66 nm, F_0 = -920k_BT.

to a "cascade effect" where longer ligands may wrap around the nanocrystals. This suggest that the shorter chains facilitate better monolayer assembly.

5.3. Conclusions

In conclusion, by modifying the surface of $CsPbBr_3$ perovskite nanocubes we have described a novel route to control the interactions for self-assembly, where the long chain hydrocarbon ligands are replaced by a shorter thiocyanate moiety. This enables high quality nanocube self-assembly into close-packed monolayers. The monolayer films could also act as seed layers to create halide perovskite single-crystalline thin films for better performance in optoelectronic devices.

5.4. Supporting information

5.4.1. Chemicals

Cesium carbonate (Cs_2CO_3, 99.9%), lead bromide ($PbBr_2$, 99.9%), octadecene (ODE, 90%), oleyl amine (OAm, 90%), oleic acid (OA, 90%), ammonium thiocyanate (NH_4SCN, 90%) are purchased from Sigma Aldrich. All the chemicals are used as received.

5.4.2. Experimental

Preparation of cesium oleate

Typically, a 0.814 g of Cs_2CO_3 is loaded into a 100 mL 3-neck flask along with 40 mL of ODE and 2.5 mL of OA, dried for 1 h at 120 °C, and then heated under N_2 to 150 °C until all Cs_2CO_3 reacts with OA. Preheating of cesium oleate to 100 °C before injection is necessary as it precipitates out from ODE at room temperature.

Synthesis of $CsPbBr_3$ nanocubes

In a typical synthesis, 0.188 mmol of $PbBr_2$ with 5 mL of ODE, 0.5 mL of OAm and 0.5 mL of OA is loaded into a three-neck round bottom flask and dried under vacuum at 120 °C for an hour. Then, the reaction atmosphere is made inert by passing N_2. After complete solubilization of $PbBr_2$, the temperature is raised to 200 °C and 0.4 mL of the preheated cesium oleate is injected into the three-neck flask. After the injection, the color of the solution turns from colorless to greenish yellow, indicating the formation of perovskite cubes. Then, we lower the temperature to 160 °C and anneal the solution at that temperature for 10 min to get uniform size dispersion of the cubes. After that, we cool down the solution using ice water bath for further use.

Isolation and purification of $CsPbBr_3$ cubes

After the synthesis, we use two step centrifugation to collect the cubes for self-assembly. First, we take 1 mL from the stock solution just after the synthesis and centrifuge at 8000 rpm for 20 min to collect all $CsPbBr_3$ particles from the solution. We discard the supernatant, wash gently the inner wall of the tube using tissue paper, and add 2 mL of toluene to disperse the whole $CsPbBr_3$ solid. Then, we perform the second step of centrifugation at 2000 rpm for 5 min to get rid of all the large particles. Now, from the supernatant, we have 2 mL of toluene containing $CsPbBr_3$ nanocubes.

Surface modification of $CsPbBr_3$ nanocubes

To get well-controlled self-assembly, we performed surface modification of the cubes from long hydrocarbon oleyl chain to short thiocyanate. We use NH_4SCN as a source of thiocyanate. About 50 mg of the NH_4SCN powder is added in excess into 2 mL perovskite cube solution in toluene in a 4 mL vial containing a magnetic bar. The solution is stirred for 30 min inside a glovebox. To get rid of the insoluble NH_4SCN, we centrifuge the solution at 2000 rpm for 2 min and use the supernatant for self-assembly study. NH_4SCN is insoluble in toluene but replaces some of the oleate ligands from the surfaces of the cubes, as confirmed from FTIR spectroscopy.

Monolayer self-assembly

We make close-packed monolayer of nanocubes by controlled evaporation of toluene droplets on a Si substrate of about 5 x 5 mm in a closed chamber. First, the Si substrate is cleaned using soap solution and then ultrasonically in IPA solution. After that, the substrate is cleaned using ozone plasma for 30 s. Then, the substrate is soaked with toluene for 10 min by dipping it into toluene to get a nice wetting of nanocubes solution. Subsequently, the substrate is used for making monolayer self-assembly. 10 µL of the cube solution is dropcast on the silicon substrate and a beaker containing toluene has been placed near it. The whole system is then covered immediately with a glass container. The excess toluene vapor inside the chamber will lead to slow drying of the solvent essential for the high quality of self-assembly.

Photoluminescence quantum yield

We measure the photoluminescence quantum yield (PLQY) by using a custom modified GPS-033-SL integrating sphere built by LabSphere [240]. A laser diode (Thorlabs, L405P20, 405 nm) is used as an excitation source, passing through an optical chopper (Thorlabs, MC2000B-EC), hitting into the integrating sphere. The incident intensity is controlled with neutral density filters (Thorlabs). The beam hits the sample within a cylindrical cuvette. Light leaving the exit port of the sphere, fitted with a baffle to prevent direct reflections, hits onto a low-noise Newport 818-SL calibrated photodetector, which is connected to a Stanford Research Systems SR830 lock-in amplifier. We measure the excitation and emission separately using a short-pass filter (Thorlabs FESH0450) and long-pass filter (Thorlabs FELH0450) in front of the photodetector. The comparison of the emission and excitation results in the quantum yield. The sensitivity as a function of wavelength is calibrated with the spectral responsivity of the photodetector.

Modelling of $CsPbBr_3$ nanocubes

The nanocube core consists of a perovskite with chemical composition $CsPbBr_3$ structure. The following molecules (-COO^-, -NH_4^+, -SCN^-) are modeled as rigid bodies.

The molecules oleyl ammonium (OAm^+), oleate (OA^-), SCN^- contain some flexible elements. We consider two different types of nanocubes, with and without oleyl chains. The ligands are bound electrostatically to the perovskite core through the Br^- and Cs^+ ions. The core consists of many perovskite unit cells with a 0.587 nm lattice constant, and it is built as a rigid cube with the same mass and moment of inertia of the $CsPbBr_3$ bulk atom constituents. The bulk atoms are not simulated since we consider a hollow core, but with the equivalent mass and moment of inertia. The force field parameters are taken from the OPLS force field, resorting to CHARMM when unavailable [241, 242].

Free energy calculations

Following a previous work [224], the free energy is calculated by the integration of pressure over volume, where the cubes are held stable by placing extra harmonic springs connecting their centers. We run NVT simulations for the superlattice starting from lattice constant a_{nn}^{max} much larger than r_0, the equilibrium distance that is a minimum of the free energy, to a lattice constant a_{nn}^{min}<r_0. Note that the lattice constant of the simple square lattice is the same as the center-to-center distance of neighboring nanocubes. We collect the pressure at each lattice constant and obtain the equation of state (P(V)) through a polynomial fit, which is integrated versus the volume to obtain the free energy, as described in literature [224]. The equilibrium distance r_0 (between nanocube centers) is the lattice constant (of the superlattice) that minimizes the free energy, which occurs when the pressure becomes zero.

5.4.3. Supplementary figures

Figure 5.5: SEM image of the self-assembly of $CsPbBr_3$ nanocubes

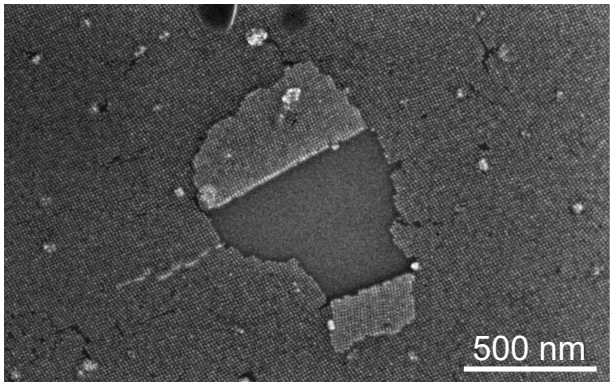

Figure 5.6: The cleaning procedure used to avoid charging effects during SEM led to partial delamination in a few places clearly indicating that the assembled film is a monolayer.

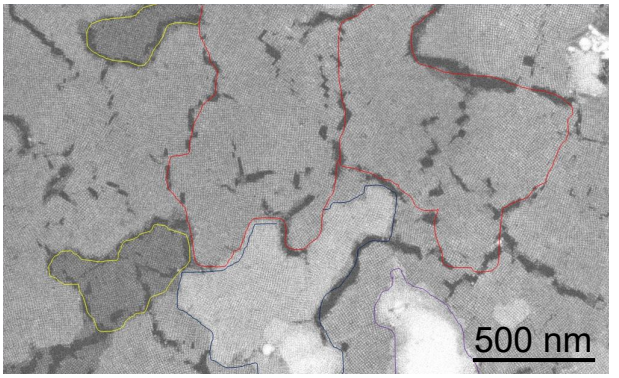

Figure 5.7: SEM image of multiple layers self-assembly of as synthesized perovskite nanocubes taken using an in-Column Detector (ICD). Contrast differences in the different areas indicate the multiple layer stacking of nanocube assembly. Yellow area show single layer, red area show double layer, blue area show triple layer, and purple area show multiple layer stacking of nanocube assembly.

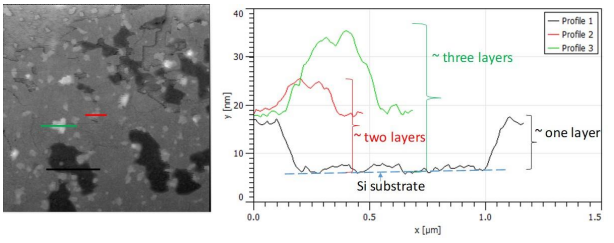

Figure 5.8: AFM image of the multiple layers stacking of nanocube assembly (left panel). Right panel shows height profile and the estimated number of layers.

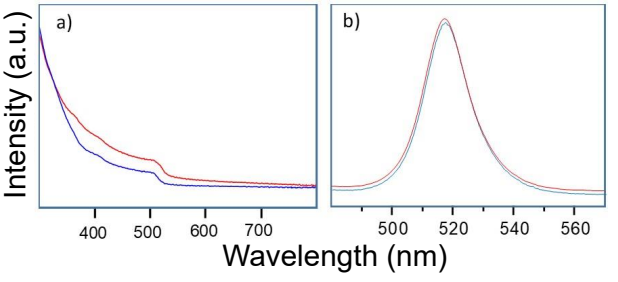

Figure 5.9: a) UV-VIS absorption and b) PL spectra of the as synthesized (red) and the thiocyanate treated (blue) sample.

BIBLIOGRAPHY

1. M. A. Boles, M. Engel, and D. V. Talapin, *Self-Assembly of Colloidal Nanocrystals: From Intricate Structures to Functional Materials,* Chem. Rev. **116**, 11220 (2016).
2. G. M. Whitesides, *Self-Assembly at All Scales,* Science **295**, 2418 (2002).
3. *https://www.vegastudio.it,* (accessed: 25.06.2020).
4. K. Liu and L. Jiang, *Bio-inspired design of multiscale structures for function integration, Nano Today*, **6**, 155 (2011).
5. M. Srinivasarao, *Nano-Optics in the Biological World: Beetles, Butterflies, Birds, and Moths,* Chem. Rev. **99**, 1935 (1999).
6. H. Fudouzi, *Tunable structural color in organisms and photonic materials for design of bioinspired materials,* Sci. Technol. Adv. Mater. **12**, 064704 (2011).
7. E. S. A. Goerlitzer, R. N. Klupp Taylor, and N. Vogel, *Bioinspired Photonic Pigments from Colloidal Self-Assembly,* Adv. Mater. **30**, 1706654 (2018).
8. P. Vukusic and J. R. Sambles, *Photonic structures in biology,* Nature **424**, 852 (2003).
9. L. Addadi and S. Weiner, *A pavement of pearl,* Nature **389**, 912 (1997).
10. L. Feng, Y. Zhang, J. Xi, Y. Zhu, N. Wang, F. Xia, and L. Jiang, *Petal effect: A superhydrophobic state with high adhesive force,* Langmuir **24**, 4114 (2008).
11. G. Mayer, *Rigid Biological Systems as Models for Synthetic Composites,* Science **310**, 1144 (2005).
12. R. Fujii, *Int. Rev. Cytol.*, Vol. 143 (Academic Press, 1993) pp. 191–255.
13. K. Mathew, A. K. Singh, J. J. Gabriel, K. Choudhary, S. B. Sinnott, A. V. Davydov, F. Tavazza, and R. G. Hennig, *MPInterfaces: A Materials Project based Python tool for high-throughput computational screening of interfacial systems,* Comput. Mater. Sci. **122**, 183 (2016).
14. M. A. Boles, D. Ling, T. Hyeon, and D. V. Talapin, *The surface science of nanocrystals,* Nat. Mater. **15**, 141 (2016).
15. Y. Xia, Y. Xiong, B. Lim, and S. E. Skrabalak, *Shape-Controlled Synthesis of Metal Nanocrystals: Simple Chemistry Meets Complex Physics?* Angew. Chemie Int. Ed. **48**, 60 (2009).

16. B. Lim, M. Jiang, J. Tao, P. H. C. Camargo, Y. Zhu, and Y. Xia, *Shape-Controlled Synthesis of Pd Nanocrystals in Aqueous Solutions,* Adv. Funct. Mater. **19**, 189 (2009).

17. A. Ruditskiy and Y. Xia, *The Science and Art of Carving Metal Nanocrystals,* ACS Nano **11**, 23 (2017).

18. A. Heuer-Jungemann, N. Feliu, I. Bakaimi, M. Hamaly, A. Alkilany, I. Chakraborty, A. Masood, M. F. Casula, A. Kostopoulou, E. Oh, K. Susumu, M. H. Stewart, I. L. Medintz, E. Stratakis, W. J. Parak, and A. G. Kanaras, *The role of ligands in the chemical synthesis and applications of inorganic nanoparticles,* Chem. Rev. **119**, 4819 (2019).

19. G. FRENS, *Controlled Nucleation for the Regulation of the Particle Size in Monodisperse Gold Suspensions,* Nat. Phys. Sci. **241**, 20 (1973).

20. C. J. Murphy, *Materials Science: Nanocubes and Nanoboxes,* Science **298**, 2139 (2002).

21. V. F. Puntes, K. M. Krishnan, and A. P. Alivisatos, *Colloidal nanocrystal shape and size control: The case of cobalt,* Science **291**, 2115 (2001).

22. X. Peng, L. Manna, W. Yang, J. Wickham, E. Scher, A. Kadavanich, and A. P. Alivisatos, *Shape control of CdSe nanocrystals,* Nature **404**, 59 (2000).

23. S. Ithurria, M. D. Tessier, B. Mahler, R. P. Lobo, B. Dubertret, and A. L. Efros, *Colloidal nanoplatelets with two-dimensional electronic structure,* Nat. Mater. **10**, 936 (2011).

24. Y. Sun, *Shape-Controlled Synthesis of Gold and Silver Nanoparticles,* Science **298**, 2176 (2002).

25. Z. Niu and Y. Li, *Removal and Utilization of Capping Agents in Nanocatalysis,* Chem. Mater. **26**, 72 (2014).

26. J.-H. Choi, H. Wang, S. J. Oh, T. Paik, P. Sung, J. Sung, X. Ye, T. Zhao, B. T. Diroll, C. B. Murray, and C. R. Kagan, *Exploiting the colloidal nanocrystal library to construct electronic devices,* Science **352**, 205 (2016).

27. Y. Shirasaki, G. J. Supran, M. G. Bawendi, and V. Bulović, *Emergence of colloidal quantum-dot light-emitting technologies,* Nat. Photonics **7**, 13 (2013).

28. C. Dang, J. Lee, C. Breen, J. S. Steckel, S. Coe-Sullivan, and A. Nurmikko, *Red, green and blue lasing enabled by single-exciton gain in colloidal quantum dot films,* Nat. Nanotechnol. **7**, 335 (2012).

29. B. Xin, Y. Pak, S. Mitra, D. Almalawi, N. Alwadai, Y. Zhang, and I. S. Roqan, *Self-Patterned $CsPbBr_3$ Nanocrystals for High-Performance Optoelectronics,* ACS Appl. Mater. Interfaces **11**, 5223 (2019).

30. K. J. M. Bishop, C. E. Wilmer, S. Soh, and B. A. Grzybowski, *Nanoscale Forces and Their Uses in Self-Assembly,* Small **5**, 1600 (2009).

31. X. Ye, J. E. Collins, Y. Kang, J. Chen, D. T. Chen, A. G. Yodh, and C. B. Murray, *Morphologically controlled synthesis of colloidal upconversion nanophosphors and their shape-directed self-assembly,* Proc. Natl. Acad. Sci. **107**, 22430 (2010).

32. V. Lotito and T. Zambelli, *Self-Assembly of Single-Sized and Binary Colloidal Particles at Air/Water Interface by Surface Confinement and Water Discharge,* Langmuir **32**, 9582 (2016).

33. M. Grzelczak, J. Vermant, E. M. Furst, and L. M. Liz-Marzán, *Directed self-assembly of nanoparticles,* ACS Nano **4**, 3591 (2010).

34. A. Tao, P. Sinsermsuksakul, and P. Yang, *Tunable plasmonic lattices of silver nanocrystals,* Nat. Nanotechnol. **2**, 435 (2007).

35. H. Zhang, C. Kinnear, and P. Mulvaney, *Fabrication of Single-Nanocrystal Arrays,* Adv. Mater. **32**, 1904551 (2020).

36. Y. Xia and G. M. Whitesides, *Soft Lithography,* Annu. Rev. Mater. Sci. **28**, 153 (1998).

37. S. Ni, L. Isa, and H. Wolf, *Capillary assembly as a tool for the heterogeneous integration of micro- and nanoscale objects,* Soft Matter **14**, 2978 (2018).

38. T. Kraus, L. Malaquin, H. Schmid, W. Riess, N. D. Spencer, and H. Wolf, *Nanoparticle printing with single-particle resolution,* Nat. Nanotechnol. **2**, 570 (2007).

39. V. Flauraud, M. Mastrangeli, G. D. Bernasconi, J. Butet, D. T. L. Alexander, E. Shahrabi, O. J. F. Martin, and J. Brugger, *Nanoscale topographical control of capillary assembly of nanoparticles,* Nat. Nanotechnol. **12**, 73 (2017).

40. M. Juodėnas, T. Tamulevičius, J. Henzie, D. Erts, and S. Tamulevičius, *Surface Lattice Resonances in Self-Assembled Arrays of Monodisperse Ag Cuboctahedra,* ACS Nano **13**, 9038 (2019).

41. N. J. Greybush, M. Saboktakin, X. Ye, C. Della Giovampaola, S. J. Oh, N. E. Berry, N. Engheta, C. B. Murray, and C. R. Kagan, *Plasmon-Enhanced Upconversion Luminescence in Single Nanophosphor–Nanorod Heterodimers Formed through Template-Assisted Self-Assembly,* ACS Nano **8**, 9482 (2014).

42. J. Henzie, S. C. Andrews, X. Y. Ling, Z. Li, and P. Yang, *Oriented assembly of polyhedral plasmonic nanoparticle clusters,* Proc. Natl. Acad. Sci. **110**, 6640 (2013).

43. J. N. Lee, C. Park, and G. M. Whitesides, *Solvent Compatibility of Poly(dimethylsiloxane)-Based Microfluidic Devices,* Anal. Chem. **75**, 6544 (2003).

44. H. Zhang, J. Cadusch, C. Kinnear, T. James, A. Roberts, and P. Mulvaney, *Direct Assembly of Large Area Nanoparticle Arrays,* ACS Nano **12**, 7529 (2018).

45. J. E. Stern, B. D. Terris, H. J. Mamin, and D. Rugar, *Deposition and imaging*

of localized charge on insulator surfaces using a force microscope, Appl. Phys. Lett. **53**, 2717 (1988).

46. H. O. Jacobs and A. Stemmer, *Measuring and modifying the electric surface potential distribution on a nanometre scale: a powerful tool in science and technology,* Surf. Interface Anal. **27**, 361 (1999).

47. H. O. Jacobs, *Submicrometer Patterning of Charge in Thin-Film Electrets,* Science **291**, 1763 (2001).

48. P. Mesquida and A. Stemmer, *Attaching Silica Nanoparticles from Suspension onto Surface Charge Patterns Generated by a Conductive Atomic Force Microscope Tip,* Adv. Mater. **13**, 1395 (2001).

49. C. Kinnear, J. Cadusch, H. Zhang, J. Lu, T. D. James, A. Roberts, and P. Mulvaney, *Directed Chemical Assembly of Single and Clustered Nanoparticles with Silanized Templates,* Langmuir **34**, 7355 (2018).

50. B. Yan, A. Thubagere, W. R. Premasiri, L. D. Ziegler, L. D. Negro, and B. M. Reinhard, *Engineered SERS substrates with multiscale signal enhancement: nanoparticle cluster arrays,* ACS Nano **3**, 1190 (2009).

51. M. Giersig and P. Mulvaney, *Preparation of ordered colloid monolayers by electrophoretic deposition,* Langmuir **9**, 3408 (1993).

52. P. Moutet, L. M. Lacroix, A. Robert, M. Impéror-Clerc, G. Viau, and L. Ressier, *Directed assembly of single colloidal gold nanowires by AFM nanoxerography,* Langmuir **31**, 4106 (2015).

53. Q. Y. Lin, Z. Li, K. A. Brown, M. N. O'Brien, M. B. Ross, Y. Zhou, S. Butun, P. C. Chen, G. C. Schatz, V. P. Dravid, K. Aydin, and C. A. Mirkin, *Strong Coupling between Plasmonic Gap Modes and Photonic Lattice Modes in DNA-Assembled Gold Nanocube Arrays,* Nano Lett. **15**, 4699 (2015).

54. Q.-Y. Lin, J. A. Mason, Z. Li, W. Zhou, M. N. O'Brien, K. A. Brown, M. R. Jones, S. Butun, B. Lee, V. P. Dravid, K. Aydin, and C. A. Mirkin, *Building superlattices from individual nanoparticles via template-confined DNA-mediated assembly,* Science **359**, 669 (2018).

55. S. Surana, A. R. Shenoy, and Y. Krishnan, *Designing DNA nanodevices for compatibility with the immune system of higher organisms,* Nat. Nanotechnol. **10**, 741 (2015).

56. A. Gopinath, E. Miyazono, A. Faraon, and P. W. K. Rothemund, *Engineering and mapping nanocavity emission via precision placement of DNA origami,* Nature **535**, 401 (2016).

57. M. Bathe and P. W. Rothemund, *DNA Nanotechnology: A foundation for Programmable Nanoscale Materials,* MRS Bull. **42**, 882 (2017).

58. J. L. Wilbur, A. Kumar, E. Kim, and G. M. Whitesides, *Microfabrication by microcontact printing of self-assembled monolayers,* Adv. Mater. **6**, 600 (1994).

59. X. Zhou, F. Boey, F. Huo, L. Huang, and H. Zhang, *Chemically Functionalized Surface Patterning,* Small **7**, 2273 (2011).

60. X. Liu, L. Fu, S. Hong, V. P. Dravid, and C. A. Mirkin, *Arrays of Magnetic Nanoparticles Patterned via "Dip-pen" Nanolithography,* Adv. Mater. **14**, 231 (2002).

61. A. Kumar, H. A. Biebuyck, and G. M. Whitesides, *Patterning Self-Assembled Monolayers: Applications in Materials Science,* Langmuir **10**, 1498 (1994).

62. J. Gargiulo, I. L. Violi, S. Cerrota, L. Chvátal, E. Cortés, E. M. Perassi, F. Diaz, P. Zemánek, and F. D. Stefani, *Accuracy and Mechanistic Details of Optical Printing of Single Au and Ag Nanoparticles,* ACS Nano **11**, 9678 (2017).

63. S. Nedev, A. S. Urban, A. A. Lutich, and J. Feldmann, *Optical Force Stamping Lithography,* Nano Lett. **11**, 5066 (2011).

64. A. S. Urban, A. A. Lutich, F. D. Stefani, and J. Feldmann, *Laser Printing Single Gold Nanoparticles,* Nano Lett. **10**, 4794 (2010).

65. Y. Zhang, S.-W. Ng, X. Lu, and Z. Zheng, *Solution-Processed Transparent Electrodes for Emerging Thin-Film Solar Cells,* Chem. Rev. **120**, 2049 (2020).

66. Y. Chen, Z. Ouyang, M. Gu, and W. Cheng, *Mechanically Strong, Optically Transparent, Giant Metal Superlattice Nanomembranes From Ultrathin Gold Nanowires,* Adv. Mater. **25**, 80 (2013).

67. J. H. M. Maurer, L. González-García, B. Reiser, I. Kanelidis, and T. Kraus, *Sintering of Ultrathin Gold Nanowires for Transparent Electronics,* ACS Appl. Mater. Interfaces **7**, 7838 (2015).

68. J. L. Peters, T. Altantzis, I. Lobato, M. A. Jazi, C. Van Overbeek, S. Bals, D. Vanmaekelbergh, and S. B. Sinai, *Mono- and Multilayer Silicene-Type Honeycomb Lattices by Oriented Attachment of PbSe Nanocrystals: Synthesis, Structural Characterization, and Analysis of the Disorder,* Chem. Mater. **30**, 4831 (2018).

69. L. Hu, H. S. Kim, J.-Y. Lee, P. Peumans, and Y. Cui, *Scalable Coating and Properties of Transparent, Flexible, Silver Nanowire Electrodes,* ACS Nano **4**, 2955 (2010).

70. E. C. Garnett, W. Cai, J. J. Cha, F. Mahmood, S. T. Connor, M. Greyson Christoforo, Y. Cui, M. D. McGehee, and M. L. Brongersma, *Self-limited plasmonic welding of silver nanowire junctions,* Nat. Mater. **11**, 241 (2012).

71. J.-H. Kim, S.-R. Kim, H.-j. Kil, Y.-c. Kim, and J.-w. Park, *Highly Conformable, Transparent Electrodes for Epidermal Electronics,* Nano Lett. **18**, 4531 (2018).

72. J.-Y. Lee, S. T. Connor, Y. Cui, and P. Peumans, *Solution-Processed Metal Nanowire Mesh Transparent Electrodes,* Nano Lett. **8**, 689 (2008).

73. C.-L. Kim, J.-Y. Lee, D.-G. Shin, J.-S. Yeo, and D.-E. Kim, *Mechanism of Heat-Induced Fusion of Silver Nanowires,* Sci. Rep. **10**, 9271 (2020).

74. J. Kang, C.-G. Park, S.-H. Lee, C. Cho, D.-G. Choi, and J.-Y. Lee, *Fabrication of high aspect ratio nanogrid transparent electrodes via capillary assembly of Ag nanoparticles,* Nanoscale **8**, 11217 (2016).

75. B. Sciacca, A. Berkhout, B. J. M. Brenny, S. Z. Oener, M. A. van Huis, A. Polman, and E. C. Garnett, *Monocrystalline Nanopatterns Made by Nanocube Assembly and Epitaxy,* Adv. Mater. **29**, 1701064 (2017).

76. M. L. Lee, E. A. Fitzgerald, M. T. Bulsara, M. T. Currie, and A. Lochtefeld, *Strained Si, SiGe, and Ge Channels for High-mobility Metal-oxide-semiconductor Field-effect Transistors,* J. Appl. Phys. **97**, 011101 (2005).

77. B. Wei, K. Zheng, Y. Ji, Y. Zhang, Z. Zhang, and X. Han, *Size-Dependent Bandgap Modulation of ZnO Nanowires by Tensile Strain,* Nano Lett. **12**, 4595 (2012).

78. C. W. Liu and L. J. Chen, *Encyclopedia of Nanoscience and Nanotechnology*, edited by H. S. Nalwa, Vol. 9 (American Scientific Publishers, 2004) Chap. SiGe/Si Heterostructures, pp. 1–18.

79. J. R. Watling and D. J. Paul, *A study of the impact of dislocations on the thermoelectric properties of quantum wells in the Si/SiGe materials system,* J. Appl. Phys. **110**, 114508 (2011).

80. N. Yamamoto, H. Itoh, V. Grillo, S. F. Chichibu, S. Keller, J. S. Speck, S. P. DenBaars, U. K. Mishra, S. Nakamura, and G. Salviati, *Cathodoluminescence characterization of dislocations in gallium nitride using a transmission electron microscope,* J. Appl. Phys. **94**, 4315 (2003).

81. T. Hino, S. Tomiya, T. Miyajima, K. Yanashima, S. Hashimoto, and M. Ikeda, *Characterization of threading dislocations in GaN epitaxial layers,* Appl. Phys. Lett. **76**, 3421 (2000).

82. S. Nakamura, *The Roles of Structural Imperfections in InGaN-Based Blue Light-Emitting Diodes and Laser Diodes,* Science **281**, 956 (1998).

83. A. Osinsky, S. Gangopadhyay, R. Gaska, B. Williams, M. A. Khan, D. Kuksenkov, and H. Temkin, *Low Noise p-π-n GaN Ultraviolet Photodetectors,* Appl. Phys. Lett. **71**, 2334 (1997).

84. S. Nakamura, *Background Story of the Invention of Efficient InGaN Blue-Light-Emitting Diodes (Nobel Lecture),* Angew. Chemie Int. Ed. **54**, 7770 (2015).

85. K. Hartman, M. Bertoni, J. Serdy, and T. Buonassisi, *Dislocation density reduction in multicrystalline silicon solar cell material by high temperature annealing,* Appl. Phys. Lett. **93**, 122108 (2008).

86. M. V. Kelso, N. K. Mahenderkar, Q. Chen, J. Z. Tubbesing, and J. A. Switzer, *Spin Coating Epitaxial Films,* Science **364**, 166 (2019).

87. C. Tan, J. Chen, X.-J. Wu, and H. Zhang, *Epitaxial Growth of Hybrid Nanostructures,* Nat. Rev. Mater. **3**, 17089 (2018).

88. J. Liu and J. Zhang, *Nanointerface Chemistry: Lattice-Mismatch-Directed Synthesis and Application of Hybrid Nanocrystals,* Chem. Rev. **120**, 2123 (2020).

89. H. C. Peng, J. Park, L. Zhang, and Y. Xia, *Toward a Quantitative Understanding of Symmetry Reduction Involved in the Seed-Mediated Growth of Pd Nanocrystals,* J. Am. Chem. Soc. **137**, 6643 (2015).

90. W. Niu, L. Zhang, and G. Xu, *Shape-controlled Synthesis of Single-crystalline Palladium Nanocrystals,* ACS Nano **4**, 1987 (2010).

91. H. Agrawal and E. C. Garnett, *Nanocube Imprint Lithography,* ACS Nano **14**, 11009 (2020).

92. H. Agrawal, B. K. Patra, T. Altantzis, A. De Backer, and E. C. Garnett, *Quantifying Strain and Dislocation Density at Nanocube Interfaces after Assembly and Epitaxy,* ACS Appl. Mater. Interfaces **12**, 8788 (2020).

93. B. K. Patra, H. Agrawal, J.-Y. Zheng, X. Zha, A. Travesset, and E. C. Garnett, *Close-Packed Ultrasmooth Self-assembled Monolayer of $CsPbBr_3$ Perovskite Nanocubes,* ACS Appl. Mater. Interfaces **12**, 31764 (2020).

94. K. Wang, G. Xing, Q. Song, and S. Xiao, *Micro- and Nanostructured Lead Halide Perovskites: From Materials to Integrations and Devices,* Adv. Mater. , 2000306 (2020).

95. B. Jeong, H. Han, and C. Park, *Micro- and Nanopatterning of Halide Perovskites Where Crystal Engineering for Emerging Photoelectronics Meets Integrated Device Array Technology,* Adv. Mater. , 2000597 (2020).

96. A. Pimpin and W. Srituravanich, *Review on Micro- and Nanolithography Techniques and their Applications,* Eng. J. **16**, 37 (2012).

97. C. R. Kagan, E. Lifshitz, E. H. Sargent, and D. V. Talapin, *Building devices from colloidal quantum dots,* Science **353**, aac5523 (2016).

98. A. Kumar and G. M. Whitesides, *Features of gold having micrometer to centimeter dimensions can be formed through a combination of stamping with an elastomeric stamp and an alkanethiol "ink" followed by chemical etching,* Appl. Phys. Lett. **63**, 2002 (1993).

99. P. Yang, L. Zhang, D. J. Kang, R. Strahl, and T. Kraus, *High-Resolution Inkjet Printing of Quantum Dot Light-Emitting Microdiode Arrays,* Adv. Opt. Mater. **8**, 1901429 (2020).

100. S. Liu, R. Maoz, and J. Sagiv, *Planned nanostructures of colloidal gold via self-assembly on hierarchically assembled organic bilayer template patterns with in-situ generated terminal amino functionality,* Nano Lett. **4**, 845 (2004).

101. R. Garcia, A. W. Knoll, and E. Riedo, *Advanced scanning probe lithography,* Nat. Nanotechnol. **9**, 577 (2014).

102. S. Y. Chou, P. R. Krauss, and P. J. Renstrom, *Imprint Lithography with 25-Nanometer Resolution,* Science **272**, 85 (1996).

103. S. Y. Chou and P. R. Krauss, *Imprint lithography with sub-10 nm feature size and high throughput,* Microelectron. Eng. **35**, 237 (1997).

104. M. D. Austin, H. Ge, W. Wu, M. Li, Z. Yu, D. Wasserman, S. A. Lyon, and S. Y. Chou, *Fabrication of 5nm linewidth and 14nm pitch features by nanoimprint lithography,* Appl. Phys. Lett. **84**, 5299 (2004).

105. S. Y. Chou, C. Keimel, and J. Gu, *Ultrafast and direct imprint of nanostructures in silicon,* Nature **417**, 835 (2002).

106. J. Henzie, J. E. Barton, C. L. Stender, and T. W. Odom, *Large-area nanoscale patterning: Chemistry meets fabrication,* Acc. Chem. Res. **39**, 249 (2006).

107. M. A. Verschuuren, M. Megens, Y. Ni, H. van Sprang, and A. Polman, *Large area nanoimprint by substrate conformal imprint lithography (SCIL),* Adv. Opt. Technol. **6**, 243 (2017).

108. H. Tan, *Roller nanoimprint lithography,* J. Vac. Sci. Technol. B Microelectron. Nanom. Struct. **16**, 3926 (1998).

109. S. H. Ahn and L. J. Guo, *High-speed roll-to-roll nanoimprint lithography on flexible plastic substrates,* Adv. Mater. **20**, 2044 (2008).

110. S. H. Ahn and L. J. Guo, *Large-Area Roll-to-Roll and Roll-to-Plate Nanoimprint Lithography: A Step toward High-Throughput Application of Continuous Nanoimprinting,* ACS Nano **3**, 2304 (2009).

111. R. Kothari, M. R. Beaulieu, N. R. Hendricks, S. Li, and J. J. Watkins, *Direct Patterning of Robust One-Dimensional, Two-Dimensional, and Three-Dimensional Crystalline Metal Oxide Nanostructures Using Imprint Lithography and Nanoparticle Dispersion Inks,* Chem. Mater. **29**, 3908 (2017).

112. E. King, Y. Xia, X.-M. Zhao, and G. M. Whitesides, *Solvent-assisted microcontact molding: A convenient method for fabricating three-dimensional structures on surfaces of polymers,* Adv. Mater. **9**, 651 (1997).

113. M. R. Beaulieu, N. R. Hendricks, and J. J. Watkins, *Large-Area Printing of Optical Gratings and 3D Photonic Crystals Using Solution-Processable Nanoparticle/Polymer Composites,* ACS Photonics **1**, 799 (2014).

114. W. Li, Y. Zhou, I. R. Howell, Y. Gai, A. R. Naik, S. Li, K. R. Carter, and J. J. Watkins, *Direct Imprinting of Scalable, High-Performance Woodpile Electrodes for Three-Dimensional Lithium-Ion Nanobatteries,* ACS Appl. Mater. Interfaces **10**, 5447 (2018).

115. M. H. Lee, M. D. Huntington, W. Zhou, J.-C. Yang, and T. W. Odom, *Programmable Soft Lithography: Solvent-Assisted Nanoscale Embossing,* Nano Lett. **11**, 311 (2011).

116. T. W. Odom, J. C. Love, D. B. Wolfe, K. E. Paul, and G. M. Whitesides,

Improved pattern transfer in soft lithography using composite stamps, Langmuir **18**, 5314 (2002).

117. I.-K. Ding, J. Zhu, W. Cai, S.-J. Moon, N. Cai, P. Wang, S. M. Zakeeruddin, M. Grätzel, M. L. Brongersma, Y. Cui, and M. D. McGehee, *Plasmonic Dye-Sensitized Solar Cells,* Adv. Energy Mater. **1**, 52 (2011).

118. P. Spinelli, M. Verschuuren, and A. Polman, *Broadband omnidirectional antireflection coating based on subwavelength surface Mie resonators,* Nat. Commun. **3**, 692 (2012).

119. X. He, P. Liu, H. Zhang, Q. Liao, J. Yao, and H. Fu, *Patterning Multicolored Microdisk Laser Arrays of Cesium Lead Halide Perovskite,* Adv. Mater. **29**, 1604510 (2017).

120. H. Zhang, Q. Liao, Y. Wu, Z. Zhang, Q. Gao, P. Liu, M. Li, J. Yao, and H. Fu, *2D Ruddlesden-Popper Perovskites Microring Laser Array,* Adv. Mater. **30**, 1706186 (2018).

121. C. Matricardi, C. Hanske, J. L. Garcia-Pomar, J. Langer, A. Mihi, and L. M. Liz-Marzán, *Gold Nanoparticle Plasmonic Superlattices as Surface-Enhanced Raman Spectroscopy Substrates,* ACS Nano **12**, 8531 (2018).

122. J. van de Groep, D. Gupta, M. A. Verschuuren, M. M. Wienk, R. A. J. Janssen, and A. Polman, *Large-area soft-imprinted nanowire networks as light trapping transparent conductors,* Sci. Rep. **5**, 11414 (2015).

123. B. Sciacca, J. van de Groep, A. Polman, and E. C. Garnett, *Solution-Grown Silver Nanowire Ordered Arrays as Transparent Electrodes,* Adv. Mater. **28**, 905 (2016).

124. J. H. M. Maurer, L. González-García, B. Reiser, I. Kanelidis, and T. Kraus, *Templated Self-Assembly of Ultrathin Gold Nanowires by Nanoimprinting for Transparent Flexible Electronics,* Nano Lett. **16**, 2921 (2016).

125. J. H. M. Maurer, L. González-García, I. K. Backes, B. Reiser, S. M. Schlossberg, and T. Kraus, *Direct Nanoimprinting of a Colloidal Self-Organizing Nanowire Ink for Flexible, Transparent Electrodes,* Adv. Mater. Technol. **2**, 1700034 (2017).

126. S. H. Ko, I. Park, H. Pan, C. P. Grigoropoulos, A. P. Pisano, C. K. Luscombe, and J. M. J. Fréchet, *Direct Nanoimprinting of Metal Nanoparticles for Nanoscale Electronics Fabrication,* Nano Lett. **7**, 1869 (2007).

127. M. Alam and D. Cameron, *Investigation of annealing effects on sol–gel deposited indium tin oxide thin films in different atmospheres,* Thin Solid Films **420-421**, 76 (2002).

128. A. Kamyshny and S. Magdassi, *Conductive Nanomaterials for Printed Electronics,* Small **10**, 3515 (2014).

129. H. J. Yang, S. Y. He, H. L. Chen, and H. Y. Tuan, *Monodisperse copper*

nanocubes: Synthesis, self-assembly, and large-area dense-packed films, Chem. Mater. **26**, 1785 (2014).

130. A. P. Lagrow, B. Ingham, S. Cheong, G. V. Williams, C. Dotzler, M. F. Toney, D. A. Jefferson, E. C. Corbos, P. T. Bishop, J. Cookson, and R. D. Tilley, *Synthesis, alignment, and magnetic properties of monodisperse nickel nanocubes,* J. Am. Chem. Soc. **134**, 855 (2012).

131. A. R. Tao, S. Habas, and P. Yang, *Shape control of colloidal metal nanocrystals,* Small **4**, 310 (2008).

132. K. M. Koczkur, S. Mourdikoudis, L. Polavarapu, and S. E. Skrabalak, *Polyvinylpyrrolidone (PVP) in nanoparticle synthesis,* Dalt. Trans. **44**, 17883 (2015).

133. J.-E. Park, Y. Lee, and J.-M. Nam, *Precisely Shaped, Uniformly Formed Gold Nanocubes with Ultrahigh Reproducibility in Single-Particle Scattering and Surface-Enhanced Raman Scattering,* Nano Lett. **18**, 6475 (2018).

134. H. A. Macpherson and C. R. Stoldt, *Iron Pyrite Nanocubes: Size and Shape Considerations for Photovoltaic Application,* ACS Nano **6**, 8940 (2012).

135. C.-H. Kuo, C.-H. Chen, and M. H. Huang, *Seed-Mediated Synthesis of Monodispersed Cu_2O Nanocubes with Five Different Size Ranges from 40 to 420 nm,* Adv. Funct. Mater. **17**, 3773 (2007).

136. L. Protesescu, S. Yakunin, M. I. Bodnarchuk, F. Krieg, R. Caputo, C. H. Hendon, R. X. Yang, A. Walsh, and M. V. Kovalenko, *Nanocrystals of Cesium Lead Halide Perovskites ($CsPbX_3$, X = Cl, Br, and I): Novel Optoelectronic Materials Showing Bright Emission with Wide Color Gamut,* Nano Lett. **15**, 3692 (2015).

137. H.-S. Chen, S.-C. Wu, and M. H. Huang, *Direct synthesis of size-tunable PbS nanocubes and octahedra and the pH effect on crystal shape control,* Dalt. Trans. **44**, 15088 (2015).

138. S.-B. Wang, Y.-L. Min, and S.-H. Yu, *Synthesis and Magnetic Properties of Uniform Hematite Nanocubes,* J. Phys. Chem. C **111**, 3551 (2007).

139. F. Dang, K.-i. Mimura, K. Kato, H. Imai, S. Wada, H. Haneda, and M. Kuwabara, *Growth of monodispersed $SrTiO_3$ nanocubes by thermohydrolysis method,* CrystEngComm **13**, 3878 (2011).

140. H.-X. Mai, L.-D. Sun, Y.-W. Zhang, R. Si, W. Feng, H.-P. Zhang, H.-C. Liu, and C.-H. Yan, *Shape-Selective Synthesis and Oxygen Storage Behavior of Ceria Nanopolyhedra, Nanorods, and Nanocubes,* J. Phys. Chem. B **109**, 24380 (2005).

141. U. A. Joshi, J. S. Jang, P. H. Borse, and J. S. Lee, *Microwave synthesis of single-crystalline perovskite $BiFeO_3$ nanocubes for photoelectrode and photocatalytic applications,* Appl. Phys. Lett. **92**, 242106 (2008).

142. S. Yang and L. Gao, *Controlled Synthesis and Self-Assembly of CeO_2 Nanocubes,* J. Am. Chem. Soc. **128**, 9330 (2006).

143. V. G. Kravets, A. V. Kabashin, W. L. Barnes, and A. N. Grigorenko, *Plasmonic Surface Lattice Resonances: A Review of Properties and Applications,* Chem. Rev. **118**, 5912 (2018).

144. T. Chen, Y. Zhang, and W. Xu, *Size-dependent catalytic kinetics and dynamics of Pd nanocubes: a single-particle study,* Phys. Chem. Chem. Phys. **18**, 22494 (2016).

145. W. H. Evers, B. Goris, S. Bals, M. Casavola, J. de Graaf, R. van Roij, M. Dijkstra, and D. Vanmaekelbergh, *Low-Dimensional Semiconductor Superlattices Formed by Geometric Control over Nanocrystal Attachment,* Nano Lett. **13**, 2317 (2013).

146. Z. Tang, N. A. Kotov, and M. Giersig, *Spontaneous Organization of Single CdTe Nanoparticles into Luminescent Nanowires,* Science **297**, 237 (2002).

147. W. J. Baumgardner, K. Whitham, and T. Hanrath, *Confined-but-connected quantum solids via controlled ligand displacement,* Nano Lett. **13**, 3225 (2013).

148. C. S. Sandeep, J. M. Azpiroz, W. H. Evers, S. C. Boehme, I. Moreels, S. Kinge, L. D. Siebbeles, I. Infante, and A. J. Houtepen, *Epitaxially connected PbSe quantum-dot films: Controlled neck formation and optoelectronic properties,* ACS Nano **8**, 11499 (2014).

149. K. Whitham, D. M. Smilgies, and T. Hanrath, *Entropic, Enthalpic, and Kinetic Aspects of Interfacial Nanocrystal Superlattice Assembly and Attachment,* Chem. Mater. **30**, 54 (2018).

150. Y. Nakagawa, H. Kageyama, Y. Oaki, and H. Imai, *Formation of Monocrystalline 1D and 2D Architectures via Epitaxial Attachment: Bottom-Up Routes through Surfactant-Mediated Arrays of Oriented Nanocrystals,* Langmuir **31**, 6197 (2015).

151. K. S. Cho, D. V. Talapin, W. Gaschler, and C. B. Murray, *Designing PbSe nanowires and nanorings through oriented attachment of nanoparticles,* J. Am. Chem. Soc. **127**, 7140 (2005).

152. C. Schliehe, B. H. Juarez, M. Pelletier, S. Jander, D. Greshnykh, M. Nagel, A. Meyer, S. Foerster, A. Kornowski, C. Klinke, and H. Weller, *Ultrathin PbS Sheets by Two-Dimensional Oriented Attachment,* Science **74**, 550 (2010).

153. Y. Tong, B. J. Bohn, E. Bladt, K. Wang, P. Müller-Buschbaum, S. Bals, A. S. Urban, L. Polavarapu, and J. Feldmann, *From Precursor Powders to $CsPbX_3$ Perovskite Nanowires: One-Pot Synthesis, Growth Mechanism, and Oriented Self-Assembly,* Angew. Chemie Int. Ed. **56**, 13887 (2017).

154. S. Sarkar, S. Acharya, A. Chakraborty, and N. Pradhan, *Zinc blende 0D quantum dots to wurtzite 1D quantum wires: The oriented attachment and phase change in ZnSe nanostructures,* J. Phys. Chem. Lett. **4**, 3292 (2013).

155. L. C. Kao, Y. Ye, Y.-S. Liu, C. L. Dong, J. Guo, and S. Y. H. Liou, *A facile route for the synthesis of heterogeneous crystal structures in hierarchical architectures with vacancy-driven defects via the oriented attachment growth mechanism,* J. Mater. Chem. A **6**, 10663 (2018).

156. H. Y. Jung, J. Joo, M. P. Hyun, S. I. Baik, W. K. Young, C. K. Sung, and T. Hyeon, *Synthesis of quantum-sized cubic ZnS nanorods by the oriented attachment mechanism,* J. Am. Chem. Soc. **127**, 5662 (2005).

157. V. M. Yuwono, N. D. Burrows, J. A. Soltis, and R. L. Penn, *Oriented Aggregation: Formation and Transformation of Mesocrystal Intermediates Revealed,* J. Am. Chem. Soc. **132**, 2163 (2010).

158. A. Figuerola, I. R. Franchini, A. Fiore, R. Mastria, A. Falqui, G. Bertoni, S. Bals, C. Van Tendeloo, S. Kudera, R. Cingolani, and L. Manna, *End-to-end assembly of shape-controlled nanocrystals via a nanowelding approach mediated by gold domains,* Adv. Mater. **21**, 550 (2009).

159. C. Hanske, E. H. Hill, D. Vila-Liarte, G. González-Rubio, C. Matricardi, A. Mihi, and L. M. Liz-Marzán, *Solvent-Assisted Self-Assembly of Gold Nanorods into Hierarchically Organized Plasmonic Mesostructures,* ACS Appl. Mater. Interfaces **11**, 11763 (2019).

160. T. Kister, J. H. M. Maurer, L. González-García, and T. Kraus, *Ligand-Dependent Nanoparticle Assembly and Its Impact on the Printing of Transparent Electrodes,* ACS Appl. Mater. Interfaces **10**, 6079 (2018).

161. M. P. Boneschanscher, W. H. Evers, J. J. Geuchies, T. Altantzis, B. Goris, F. T. Rabouw, S. A. P. Van Rossum, H. S. J. Van Der Zant, L. D. A. Siebbeles, G. Van Tendeloo, I. Swart, J. Hilhorst, A. V. Petukhov, S. Bals, and D. Vanmaekelbergh, *Long-range orientation and atomic attachment of nanocrystals in 2D honeycomb superlattices,* Science **344**, 1377 (2014).

162. C. Van Overbeek, J. L. Peters, S. A. Van Rossum, M. Smits, M. A. Van Huis, and D. Vanmaekelbergh, *Interfacial Self-Assembly and Oriented Attachment in the Family of PbX (X = S, Se, Te) Nanocrystals,* J. Phys. Chem. C **122**, 12464 (2018).

163. M. V. Kovalenko, L. Protesescu, and M. I. Bodnarchuk, *Properties and potential optoelectronic applications of lead halide perovskite nanocrystals,* Science **358**, 745 (2017).

164. C. Kuemin, L. Nowack, L. Bozano, N. D. Spencer, and H. Wolf, *Oriented Assembly of Gold Nanorods on the Single-Particle Level,* Adv. Funct. Mater. **22**, 702 (2012).

165. A. R. Tao, J. Huang, and P. Yang, *Langmuir - Blodgettry of Nanocrystals and Nanowires,* Acc. Chem. Res. **41**, 1662 (2008).

166. J. Lee, I. Lee, T.-S. Kim, and J.-Y. Lee, *Efficient Welding of Silver Nanowire Networks without Post-Processing,* Small **9**, 2887 (2013).

167. Z. Zhong, H. Lee, D. Kang, S. Kwon, Y.-M. Choi, I. Kim, K.-Y. Kim, Y. Lee, K. Woo, and J. Moon, *Continuous Patterning of Copper Nanowire-Based Transparent Conducting Electrodes for Use in Flexible Electronic Applications,* ACS Nano **10**, 7847 (2016).

168. K. Miszta, J. De Graaf, G. Bertoni, D. Dorfs, R. Brescia, S. Marras, L. Ceseracciu, R. Cingolani, R. Van Roij, M. Dijkstra, and L. Manna, *Hierarchical self-assembly of suspended branched colloidal nanocrystals into superlattice structures,* Nat. Mater. **10**, 872 (2011).

169. P. Vogt, P. De Padova, C. Quaresima, J. Avila, E. Frantzeskakis, M. C. Asensio, A. Resta, B. Ealet, and G. Le Lay, *Silicene: Compelling Experimental Evidence for Graphenelike Two-Dimensional Silicon,* Phys. Rev. Lett. **108**, 155501 (2012).

170. J. J. Geuchies, C. van Overbeek, W. H. Evers, B. Goris, A. de Backer, A. P. Gantapara, F. T. Rabouw, J. Hilhorst, J. L. Peters, O. Konovalov, A. V. Petukhov, M. Dijkstra, L. D. A. Siebbeles, S. van Aert, S. Bals, and D. Vanmaekelbergh, *In situ study of the formation mechanism of two-dimensional superlattices from PbSe nanocrystals,* Nat. Mater. **15**, 1248 (2016).

171. M. Takasaki, Y. Oaki, and H. Imai, *Switchable oriented attachment and detachment of calcite nanocrystals,* CrystEngComm **18**, 8999 (2016).

172. L. Wang, B. Liu, X. Zhao, H. V. Demir, H. Gu, and H. Sun, *Solvent-Assisted Surface Engineering for High-Performance All-Inorganic Perovskite Nanocrystal Light-Emitting Diodes,* ACS Appl. Mater. Interfaces **10**, 19828 (2018).

173. L. Gomez, J. Lin, C. de Weerd, L. Poirier, S. C. Boehme, E. von Hauff, Y. Fujiwara, K. Suenaga, and T. Gregorkiewicz, *Extraordinary Interfacial Stitching between Single All-Inorganic Perovskite Nanocrystals,* ACS Appl. Mater. Interfaces **10**, 5984 (2018).

174. D. Li, M. M. H. Nielsen, J. J. R. I. Lee, C. Frandsen, J. F. Banfield, and J. J. De Yoreo, *Direction-Specific Interactions Control Crystal Growth by Oriented Attachment,* Science **336**, 1014 (2012).

175. M. A. Van Huis, L. T. Kunneman, K. Overgaag, Q. Xu, G. Pandraud, H. W. Zandbergen, and D. Vanmaekelbergh, *Low-temperature nanocrystal unification through rotations and relaxations probed by in situ transmission electron microscopy,* Nano Lett. **8**, 3959 (2008).

176. C. Zhu, S. Liang, E. Song, Y. Zhou, W. Wang, F. Shan, Y. Shi, C. Hao, K. Yin, T. Zhang, J. Liu, H. Zheng, and L. Sun, *In-situ liquid cell transmission electron microscopy investigation on oriented attachment of gold nanoparticles,* Nat. Commun. **9**, 421 (2018).

177. S. F. Tan, S. Raj, G. Bisht, H. V. Annadata, C. A. Nijhuis, P. Král,

and U. Mirsaidov, *Nanoparticle Interactions Guided by Shape-Dependent Hydrophobic Forces,* Adv. Mater. **1707077**, 1 (2018).

178. W. Lv, W. He, X. Wang, Y. Niu, H. Cao, J. H. Dickerson, and Z. Wang, *Understanding the oriented-attachment growth of nanocrystals from an energy point of view: a review,* Nanoscale **6**, 2531 (2014).

179. W. Lv, Y. Zhu, Y. Niu, W. Huo, K. Li, G. Zhu, Y. Liang, W. Wu, and W. He, *Assembly of anisotropic one dimensional Ag nanostructures through orientated attachment: on-axis or off-axis growth?* RSC Adv. **5**, 20783 (2015).

180. W. Lv, W. Huo, Y. Niu, Y. Zhu, Y. Xie, X. Guo, and W. He, *Oriented-attachment dimensionality build-up via van der Waals interaction,* CrystEngComm **17**, 729 (2015).

181. F. Hofmann, B. Abbey, W. Liu, R. Xu, B. F. Usher, E. Balaur, and Y. Liu, *X-ray micro-beam characterization of lattice rotations and distortions due to an individual dislocation,* Nat. Commun. **4**, 2774 (2013).

182. J. C. Ondry, M. R. Hauwiller, and A. P. Alivisatos, *Dynamics and Removal Pathway of Edge Dislocations in Imperfectly Attached PbTe Nanocrystal Pairs: Toward Design Rules for Oriented Attachment,* ACS Nano **12**, 3178 (2018).

183. M. H. Tsai, S. Y. Chen, and P. Shen, *Imperfect Oriented Attachment: Accretion and Defect Generation of Nanosize Rutile Condensates,* Nano Lett. **4**, 1197 (2004).

184. R. L. Penn and J. F. Banfield, *Imperfect Oriented Attachment: Dislocation Generation in Defect-Free Nanocrystals,* Science **281**, 969 (1998).

185. L. Yang, M. T. Bulsara, K. E. Lee, and E. A. Fitzgerald, *Compositionally-graded InGaAs–InGaP Alloys and GaAsSb Alloys for Metamorphic InP on GaAs,* J. Cryst. Growth **324**, 103 (2011).

186. J. Y. Tsao, J. Han, R. H. Haitz, and P. M. Pattison, *The Blue LED Nobel Prize: Historical context, current scientific understanding, human benefit,* Ann. Phys. **527**, A53 (2015).

187. E. A. Fitzgerald, Y. Xie, M. L. Green, D. Brasen, A. R. Kortan, J. Michel, Y. Mii, and B. E. Weir, *Totally relaxed Ge_xSi_{1-x} Layers with Low Threading Dislocation Densities Grown on Si Substrates,* Appl. Phys. Lett. **59**, 811 (1991).

188. M. A. Boles and D. V. Talapin, *Connecting the dots,* Science **344**, 1340 (2014).

189. A. De Backer, K. van den Bos, W. Van den Broek, J. Sijbers, and S. Van Aert, *StatSTEM: An efficient approach for accurate and precise model-based quantification of atomic resolution electron microscopy images,* Ultramicroscopy **171**, 104 (2016).

190. S. M. Ansar, F. S. Ameer, W. Hu, S. Zou, C. U. Pittman, and D. Zhang, *Removal of Molecular Adsorbates on Gold Nanoparticles Using Sodium Borohydride in Water,* Nano Lett. **13**, 1226 (2013).

191. N. Nalajala, W. F. Gooty Saleha, B. P. Ladewig, and M. Neergat, *Sodium Borohydride Treatment: A Simple and Effective Process for the Removal of Stabilizer and Capping Agents from Shape-controlled Palladium Nanoparticles.* Chem. Commun. **50**, 9365 (2014).

192. *https://nanocomposix.eu,* (accessed: 24.02.2020).

193. J. Ma, N. A. Choudhury, and Y. Sahai, *A comprehensive review of direct borohydride fuel cells,* Renew. Sustain. Energy Rev. **14**, 183 (2010).

194. P. Schapotschnikow, R. Pool, and T. J. H. Vlugt, *Molecular Simulations of Interacting Nanocrystals,* Nano Lett. **8**, 2930 (2008).

195. P. Schapotschnikow, M. A. van Huis, H. W. Zandbergen, D. Vanmaekelbergh, and T. J. H. Vlugt, *Morphological Transformations and Fusion of PbSe Nanocrystals Studied Using Atomistic Simulations,* Nano Lett. **10**, 3966 (2010).

196. L. Wang, P. Liu, P. Guan, M. Yang, J. Sun, Y. Cheng, A. Hirata, Z. Zhang, M. Evan, M. Chen, and X. Han, *In situ atomic-scale observation of continuous and reversible lattice deformation beyond the elastic limit,* Nat. Commun. **4**, 2413 (2013).

197. Y. Xiong, H. Cai, B. J. Wiley, J. Wang, M. J. Kim, and Y. Xia, *Synthesis and Mechanistic Study of Palladium Nanobars and Nanorods,* J. Am. Chem. Soc. **129**, 3665 (2007).

198. Y. C. Cho, S. Lee, M. Ajmal, W.-K. Kim, C. R. Cho, S.-Y. Jeong, J. H. Park, S. E. Park, S. Park, H.-K. Pak, and H. C. Kim, *Copper Better than Silver: Electrical Resistivity of the Grain-Free Single-Crystal Copper Wire,* Cryst. Growth Des. **10**, 2780 (2010).

199. P. Spittle, *Gas turbine technology,* Phys. Educ. **38**, 504 (2003).

200. K. Ellmer, *Past achievements and future challenges in the development of optically transparent electrodes,* Nat. Photonics **6**, 809 (2012).

201. R. A. Pala, J. White, E. Barnard, J. Liu, and M. L. Brongersma, *Design of Plasmonic Thin-Film Solar Cells with Broadband Absorption Enhancements,* Adv. Mater. **21**, 3504 (2009).

202. J. van de Groep, P. Spinelli, and A. Polman, *Transparent Conducting Silver Nanowire Networks,* Nano Lett. **12**, 3138 (2012).

203. F. Uleman, V. Neder, A. Cordaro, A. Alù, and A. Polman, *Resonant Metagratings for Spectral and Angular Control of Light for Colored Rooftop Photovoltaics,* ACS Appl. Energy Mater. **3**, 3150 (2020).

204. N. Lassaline, R. Brechbühler, S. J. W. Vonk, K. Ridderbeek, M. Spieser, S. Bisig, B. le Feber, F. T. Rabouw, and D. J. Norris, *Optical Fourier surfaces,* Nature **582**, 506 (2020).

205. W. Zhou, Z. Liu, Z. Huang, H. Lin, D. Samanta, Q.-y. Lin, K. Aydin,

and C. A. Mirkin, *Device-quality, Reconfigurable Metamaterials from Shape-directed Nanocrystal Assembly,* Proc. Natl. Acad. Sci. , 21052 (2020).

206. T. Tokuno, M. Nogi, M. Karakawa, J. Jiu, T. T. Nge, Y. Aso, and K. Suganuma, *Fabrication of silver nanowire transparent electrodes at room temperature,* Nano Res. **4**, 1215 (2011).

207. X. Liu, W. Liu, and B. Yang, *Highly ordered 3D-silver nanoring arrays (3D-AgNRAs) for refractometric sensing,* J. Mater. Chem. C **7**, 7681 (2019).

208. L. Novotny and B. Hecht, *Princ. Nano-Optics*, Vol. 9781107005 (Cambridge University Press, Cambridge, 2012) pp. 1–564.

209. Y. Yang, J. Liu, Z. W. Fu, and D. Qin, *Galvanic replacement-free deposition of au on ag for core-shell nanocubes with enhanced chemical stability and SERS activity,* J. Am. Chem. Soc. **136**, 8153 (2014).

210. S. A. Mann, B. Sciacca, Y. Zhang, J. Wang, E. Kontoleta, H. Liu, and E. C. Garnett, *Integrating Sphere Microscopy for Direct Absorption Measurements of Single Nanostructures,* ACS Nano **11**, 1412 (2017).

211. S.-Y. Zhang, M. D. Regulacio, and M.-Y. Han, *Self-assembly of colloidal one-dimensional nanocrystals,* Chem. Soc. Rev. **43**, 2301 (2014).

212. N. Vogel, M. Retsch, C.-A. Fustin, A. del Campo, and U. Jonas, *Advances in Colloidal Assembly: The Design of Structure and Hierarchy in Two and Three Dimensions,* Chem. Rev. **115**, 6265 (2015).

213. G. Rainò, M. A. Becker, M. I. Bodnarchuk, R. F. Mahrt, M. V. Kovalenko, and T. Stöferle, *Superfluorescence from lead halide perovskite quantum dot superlattices,* Nature **563**, 671 (2018).

214. V. K. Ravi, R. A. Scheidt, J. Dubose, and P. V. Kamat, *Hierarchical Arrays of Cesium Lead Halide Perovskite Nanocrystals through Electrophoretic Deposition,* J. Am. Chem. Soc. **140**, 8887 (2018).

215. A. Singh, C. Coughlan, F. Laffir, and K. M. Ryan, *Assembly of* $CuIn_{1-x}Ga_xS_2$ *nanorods into highly ordered 2D and 3D superstructures,* ACS Nano **6**, 6977 (2012).

216. W. L. Noorduin, A. Grinthal, L. Mahadevan, and J. Aizenberg, *Rationally designed complex, hierarchical microarchitectures,* Science **340**, 832 (2013).

217. A. Dong, Y. Jiao, and D. J. Milliron, *Electronically coupled nanocrystal superlattice films by in situ ligand exchange at the liquid-air interface,* ACS Nano **7**, 10978 (2013).

218. F. Pietra, F. T. Rabouw, W. H. Evers, D. V. Byelov, A. V. Petukhov, C. de Mello Donegá, and D. Vanmaekelbergh, *Semiconductor Nanorod Self-Assembly at the Liquid/Air Interface Studied by in Situ GISAXS and ex Situ TEM,* Nano Lett. **12**, 5515 (2012).

219. T. Kister, D. Monego, P. Mulvaney, A. Widmer-Cooper, and T. Kraus, *Colloidal*

Stability of Apolar Nanoparticles: The Role of Particle Size and Ligand Shell Structure, ACS Nano **12**, 5969 (2018).

220. W. Wei, Y. Wang, J. Ji, S. Zuo, W. Li, F. Bai, and H. Fan, *Fabrication of Large-Area Arrays of Vertically Aligned Gold Nanorods,* Nano Lett. **18**, 4467 (2018).

221. D. Baranov, S. Toso, M. Imran, and L. Manna, *Investigation into the Photoluminescence Red Shift in Cesium Lead Bromide Nanocrystal Superlattices,* J. Phys. Chem. Lett. **10**, 655 (2019).

222. J. S. Van Der Burgt, J. J. Geuchies, B. Van Der Meer, H. Vanrompay, D. Zanaga, Y. Zhang, W. Albrecht, A. V. Petukhov, L. Filion, S. Bals, I. Swart, and D. Vanmaekelbergh, *Cuboidal Supraparticles Self-Assembled from Cubic $CsPbBr_3$ Perovskite Nanocrystals,* J. Phys. Chem. C **122**, 15706 (2018).

223. S. K. Mehetor, H. Ghosh, and N. Pradhan, *Blue-Emitting $CsPbBr_3$ Perovskite Quantum Rods and Their Wide-Area 2D Self-Assembly,* ACS Energy Lett. **4**, 1437 (2019).

224. X. Zha and A. Travesset, *Stability and Free Energy of Nanocrystal Chains and Superlattices,* J. Phys. Chem. C **122**, 23153 (2018).

225. C. Waltmann, N. Horst, and A. Travesset, *Capping Ligand Vortices as "Atomic Orbitals" in Nanocrystal Self-Assembly,* ACS Nano **11**, 11273 (2017).

226. X. He, Y. Qiu, and S. Yang, *Fully-Inorganic Trihalide Perovskite Nanocrystals: A New Research Frontier of Optoelectronic Materials,* Adv. Mater. **29**, 1700775 (2017).

227. Q. A. Akkerman, G. Rainò, M. V. Kovalenko, and L. Manna, *Genesis, challenges and opportunities for colloidal lead halide perovskite nanocrystals,* Nat. Mater. **17**, 394 (2018).

228. J. Shamsi, A. S. Urban, M. Imran, L. De Trizio, and L. Manna, *Metal Halide Perovskite Nanocrystals: Synthesis, Post-Synthesis Modifications, and Their Optical Properties,* Chem. Rev. **119**, 3296 (2019).

229. D. Zhang, Y. Yu, Y. Bekenstein, A. B. Wong, A. P. Alivisatos, and P. Yang, *Ultrathin Colloidal Cesium Lead Halide Perovskite Nanowires,* J. Am. Chem. Soc. **138**, 13155 (2016).

230. L. Dou, M. Lai, C. S. Kley, Y. Yang, C. G. Bischak, D. Zhang, S. W. Eaton, N. S. Ginsberg, and P. Yang, *Spatially resolved multicolor $CsPbX_3$ nanowire heterojunctions via anion exchange,* Proc. Natl. Acad. Sci. **114**, 7216 (2017).

231. J. Shamsi, Z. Dang, P. Bianchini, C. Canale, F. Di Stasio, R. Brescia, M. Prato, and L. Manna, *Colloidal Synthesis of Quantum Confined Single Crystal $CsPbBr_3$ Nanosheets with Lateral Size Control up to the Micrometer Range,* J. Am. Chem. Soc. **138**, 7240 (2016).

232. J.-K. Sun, S. Huang, X.-Z. Liu, Q. Xu, Q.-H. Zhang, W.-J. Jiang, D.-J. Xue, J.-C. Xu, J.-Y. Ma, J. Ding, Q.-Q. Ge, L. Gu, X.-H. Fang, H.-Z. Zhong, J.-

S. Hu, and L.-J. Wan, *Polar Solvent Induced Lattice Distortion of Cubic CsPbI 3 Nanocubes and Hierarchical Self-Assembly into Orthorhombic Single-Crystalline Nanowires,* J. Am. Chem. Soc. **140**, 11705 (2018).

233. Y. Nagaoka, K. Hills-Kimball, R. Tan, R. Li, Z. Wang, and O. Chen, *Nanocube Superlattices of Cesium Lead Bromide Perovskites and Pressure-Induced Phase Transformations at Atomic and Mesoscale Levels,* Adv. Mater. **29**, 1606666 (2017).

234. B. Hudait, S. K. Dutta, A. Patra, D. Nasipuri, and N. Pradhan, *Facets Directed Connecting Perovskite Nanocrystals,* J. Am. Chem. Soc. **142**, 7207 (2020).

235. Y. Yang, J. T. Lee, T. Liyanage, and R. Sardar, *Flexible Polymer-Assisted Mesoscale Self-Assembly of Colloidal $CsPbBr_3$ Perovskite Nanocrystals into Higher Order Superstructures with Strong Inter-Nanocrystal Electronic Coupling,* J. Am. Chem. Soc. **141**, 1526 (2019).

236. B. A. Koscher, J. K. Swabeck, N. D. Bronstein, and A. P. Alivisatos, *Essentially Trap-Free $CsPbBr_3$ Colloidal Nanocrystals by Postsynthetic Thiocyanate Surface Treatment,* J. Am. Chem. Soc. **139**, 6566 (2017).

237. Z. Liu, Y. Bekenstein, X. Ye, S. C. Nguyen, J. Swabeck, D. Zhang, S. T. Lee, P. Yang, W. Ma, and A. P. Alivisatos, *Ligand Mediated Transformation of Cesium Lead Bromide Perovskite Nanocrystals to Lead Depleted Cs_4PbBr_6 Nanocrystals,* J. Am. Chem. Soc. **139**, 5309 (2017).

238. S. K. Balakrishnan and P. V. Kamat, *Ligand Assisted Transformation of Cubic $CsPbBr_3$ Nanocrystals into Two-Dimensional $CsPb_2Br_5$ Nanosheets,* Chem. Mater. **30**, 74 (2018).

239. T. Udayabhaskararao, L. Houben, H. Cohen, M. Menahem, I. Pinkas, L. Avram, T. Wolf, A. Teitelboim, M. Leskes, O. Yaffe, D. Oron, and M. Kazes, *A Mechanistic Study of Phase Transformation in Perovskite Nanocrystals Driven by Ligand Passivation,* Chem. Mater. **30**, 84 (2018).

240. J. C. de Mello, H. F. Wittmann, and R. H. Friend, *An improved experimental determination of external photoluminescence quantum efficiency,* Adv. Mater. **9**, 230 (1997).

241. W. L. Jorgensen, D. S. Maxwell, and J. Tirado-Rives, *Development and Testing of the OPLS All-Atom Force Field on Conformational Energetics and Properties of Organic Liquids,* J. Am. Chem. Soc. **118**, 11225 (1996).

242. B. R. Brooks, R. E. Bruccoleri, B. D. Olafson, D. J. States, S. Swaminathan, and M. Karplus, *CHARMM: A program for macromolecular energy, minimization, and dynamics calculations,* J. Comput. Chem. **4**, 187 (1983).

SUMMARY

Playing Legos with nanocubes

Today, technology drives humans. We rely on it from simple tasks like warming food to more sophisticated ones like launching a satellite. We are continually striving to make faster and more energy-efficient devices. Miniaturization has played a vital role in driving innovation and making smaller as well as compact gadgets. We can already do a lot and have industrialized nanotechnology. At the same time, there is still more that we cannot. For a simple perspective, observe nature. Gorgeous, multifunctional, and complex patterned architectures exist around us, self-assembled from solutions at near room temperature (RT). It would not be an overstatement to say we are nowhere close to nature in terms of capabilities.

For the creation of next-generation electronics, the following points can serve as design guidelines. (a) "Patterning" will continue to play an essential role in further downsizing. (b) "Materials quality" must also be taken into account to boost the device efficiencies additionally. (c) Another lesson that we have to adopt from nature is to be able to "process devices (entirely) from solution" lighting the path for simultaneous cheap, low temperature, and less environmental sensitive fabrication. Thus, to achieve this and eventually make robust and high-efficiency 3D devices, we propose using a smart combination of top-down and bottom-up strategies. We also propose using tiny building blocks, especially colloidal monocrystalline nanocubes.

Years of research in chemical synthesis has enabled intricately shaped colloidal nanocrystals. It is also possible to make these crystals in solution in large quantities. We picked the simple cubic morphology. The creation of tiny, atomically smooth, and monocrystalline cubes for various materials has already reached a high degree of

control. However, another critical piece is to be able to position the colloidal particles with nanoscale precision and then connect them (pertaining to the application) to yield a macroscopic crystal in custom-made shapes. For the former, in chapter 2, we developed a generalized bottom-up assembly technique. The concepts were borrowed from an already mature field of imprint lithography.

In nanocube imprint lithography, we cover the aspect of patterning. Monocrystalline 75 nm Ag cubes capped with PVP and dispersed in ethanol are used to print a variety of shapes on a substrate. It is shown that the use of nanocubes can practically yield void-free structures. A film of cubes is dried (resit) on the substrate, and a soft PDMS template imprints patterns out of nanocubes in the resist film. The use of a flexible material for making the template facilitates clean printing, and the desired patterns are predefined in the stamp in the form of nanotrenches via top-down lithography. 1D, 2D, and 3D patterning of cubes with high aspect ratio lines are demonstrated.

Next, the focus is shifted to material quality. Constructing patterns purely using nanocubes can yield truly monocrystalline structures (without grain boundaries). It is principally possible because of its isotropic shape with chemically equivalent 100 faces on all sides. As a result, for a face-to-face aligned pair of cubes, the crystallographic orientation is ideal for epitaxial attachment with a seamless connection. Thus, in chapter 3, we experimentally probe the quality of the interface of two joined nanocubes. For this, dropcast 7 nm Pd cubes, also capped with PVP is treated with a $NaBH_4$ solution. The hydride ion eliminates the PVP and frees the surface of the cubes. The naked cubes migrate substantial distances (microns) to form clusters of cubes. We studied the formed dimers of cubes with 300 kV scanning transmission electron microscopy to prove that it is indeed possible to make perfect single crystals using nanocubes as the building blocks. We also quantified the strain and dislocation density at the interfaces of dimers that underwent epitaxial attachment with some angular misorientation.

Chapter 4 delves into the concept of crystal overgrowth and solution processing mentioned earlier. The solution synthesized Ag cubes are printed in curves and

crossed lines on substrates like Si and quartz. Subsequently, it is shown that the cubes in the assembled patterns can be used as seeds to deposit different materials on top, locally, again in solution. For demonstration, curved crystals are made by overgrowing Ag or Au on top of Ag cubes. These crystals can be used to explore fundamental questions. Additionally, assemblies of cubes are also converted by Ag overgrowth into a patterned crystal featuring a connected network of intersecting parallel periodic lines. It is further illustrated that such a network can work as a realtime transparent electrode. Broadly speaking, this small demonstration can be developed into far-reaching technological applications with dedicated optimizations.

Processes relying on fewer parameters could be easier for technological commercial translation with high-throughout. The patterning and the local overgrowth are largely not dependent on the support substrate. Also, the merging of Ag or Pd cubes is demonstrated at RT. At the same time, the whole process uses very little ink. Thus, it is indeed possible to process patterned crystals at room temperature, in a cheaper way and on various substrates, including flexible and thermally sensitive ones. Nevertheless, to make a full-scale working device, apart from patterning, it is also equally central to make high-quality, void-free, and large unbroken layers of different materials, for example, dielectrics or semiconductors.

With this aim in mind, chapter 5 describes a way to make semiconductor monolayers of perovskite nanocubes at room temperature simply by dropcasting. 10 nm $CsPbBr_3$ cubes dispersed in toluene are used to assemble compact and continuous monolayers with perfect face-to-face packing. AFM scans reveal that the layer is very smooth, with a root-mean-square roughness of only 4 Å. Ligand exchange is used to partially replace long-chain (18 carbon) hydrocarbon ligands with short thiocyanates. It essentially helps to tune the interparticle attractions, and the supporting simulations also warrant it.

In the end, with this high level of control, the ideal dream would be to start at the surface and construct complex 3D and possibly fully monocrystalline structures/devices processed from solution. The high quality of the fabricated crystals will

enable ultra-high efficiencies for technological applications. It can also be used for fundamental studies. In this thesis, the necessary steps are demonstrated in parts. Now, the way forward would be to combine all the steps into a single monocrystalline functional device. Using cubes smaller than 75 nm will give access to even higher resolution and smaller/compact devices. The central theme of this thesis is the bottom-up assembly of monocrystalline nanocubes to build nanostructures. The idea of using nanocubes as the building blocks is analogous to using atoms for building a lattice. The literature suggests tremendous strides have already been made, but more work is required to engineer greater control and program matter at the nanoscale for useful purposes. I hope this record can provide some insights and brings us at least one step closer to realizing that goal.

SAMENVATTING

Nanoblokjes als legostenen

Vandaag de dag dient technologie de mens. We vertrouwen erop, voor eenvoudige taken als het opwarmen van voedsel, tot meer geavanceerde taken zoals het lanceren van een satelliet. We streven er voortdurend naar om snellere en energiezuinigere apparaten te maken. Miniaturisatie heeft een cruciale rol gespeeld bij het stimuleren van innovatie en bij het maken van zowel kleinere als compacte gadgets. We kunnen al veel doen en hebben nanotechnologie geïndustrialiseerd. Tegelijkertijd is er nog altijd meer dat we niet kunnen. De natuur is een goed voorbeeld om het menselijk kunnen in perspectief te plaatsen. Om ons heen bestaan prachtige, multifunctionele en complexe architecturen van fijne patronen, die zichzelf hebben samengesteld uit oplossingen bij kamertemperatuur (KT). Het zou niet overdreven zijn om te zeggen dat we qua capaciteiten niet eens in de buurt komen van wat de natuur kan.

Voor het creëren van de volgende generatie elektronica kunnen de volgende punten als ontwerprichtlijnen dienen. (a) Het maken van gedetaillerde patronen ("patterning") zal een essentiële rol blijven spelen bij verdere miniaturisatie. (b) “Materiaalkwaliteit” moet gewaarborgd worden om de efficiëntie in toepassingen extra te verhogen. (c) Een andere les die we uit de natuur moeten trekken, is de mogelijkheid om structuren volledig in oplossing te fabriceren, waardoor het mogelijk wordt om goedkoop, minder milieu gevoelig en bij lage temperaturen te produceren. Om dit te bereiken en uiteindelijk robuuste en zeer efficiënte 3D-apparaten te maken, stellen we in dit proefschrift voor om een slimme combinatie van top-down en bottom-up strategieën te gebruiken. We stellen ook voor om kleine bouwstenen te gebruiken, met name colloïdale monokristallijne nanokubussen.

Jaren van onderzoek naar chemische synthese hebben het fabriceren van ingewikkeld gevormde colloïdale nanokristallen mogelijk gemaakt. Het is ook mogelijk om deze kristallen in grote hoeveelheden in oplossing te maken. Wij kozen voor de simpele kubische morfologie. Het maakprocess voor kleine, atomair gladde en monokristallijne kubussen van verschillende materialen heeft al een hoge mate van controle bereikt. Een ander cruciaal onderdeel is echter om de colloïdale deeltjes met precisie op nanoschaal te kunnen positioneren en ze vervolgens (afhankelijk van de toepassing) te verbinden om een macroscopisch kristal in de gewenste vorm te verkrijgen. Voor het eerstgenoemde hebben we in hoofdstuk 2 een gegeneraliseerde bottom-up assemblagetechniek ontwikkeld. De concepten zijn ontleend aan een reeds volwassen vakgebied van opdruklithografie.

In nanokubus-opdruklithografie behandelen we het aspect van patroonvorming. Monokristallijne 75 nm Ag-blokjes bedekt met PVP en gedispergeerd in ethanol worden gebruikt om een verscheidenheid aan vormen op een substraat te printen. We tonen aan dat het gebruik van nanokubussen structuren met vrijwel geen ontbrekende deeltjes kan opleveren. Een film van kubussen wordt op het substraat gedroogd (resist) en een zachte PDMS-stempel drukt patronen gemaakt van nanokubussen in de resistlaag. Het gebruik van een flexibel materiaal voor het maken van de stempel vergemakkelijkt een nette afdruk, en de gewenste patronen worden vooraf in de stempel gedefinieerd in de vorm van nanogleufjes via top-down lithografie. 1D-, 2D- en 3D-patronen van kubussen met lijnen met een grote hoogte-breedteverhouding worden gedemonstreerd.

Vervolgens wordt de focus verlegd naar materiaalkwaliteit. Het construeren van patronen met enkel nanokubussen kan volledig monokristallijne structuren opleveren (zonder korrelgrenzen). Dit is voornamelijk mogelijk vanwege de isotrope vorm van de nanokubus, welke aan alle kanten chemisch equivalente (100) vlakken heeft. Dit resulteert erin dat twee naast elkaar uitgelijnde kubussen de ideale kristallografische oriëntatie hebben om een naadloze epitaxiale verbinding aan te gaan. Daarom onderzoeken we in hoofdstuk 3 experimenteel de kwaliteit van het raakvlak tussen de twee

samengevoegde nanokubussen. Hiervoor worden op een substraat gedruppelde Pd-blokjes van 7 nm groot, ook afgedekt met PVP, behandeld met een $NaBH_4$-oplossing. Het hydride-ion elimineert de PVP en maakt het oppervlak van de kubussen vrij. De naakte kubussen migreren aanzienlijke afstanden (micrometers) om clusters van kubussen te vormen. We bestudeerden de gevormde paren van kubussen met 300 kV scanning-transmissie-elektronenmicroscopie om te bewijzen dat het inderdaad mogelijk is om perfecte enkelvoudige kristallen te maken met nanokubussen als bouwstenen. We kwantificeerden ook de rek- en dislocatiedichtheid aan de grensvlakken van dimeren die epitaxiale verbinding aangingen onder een kleine hoek.

Hoofdstuk 4 gaat in op het eerder genoemde concept van kristalovergroei en verwerking in oplossing. De in oplossing gesynthetiseerde Ag-kubussen worden in bochten en gekruiste lijnen gedrukt op substraten zoals silicium en kwarts. Vervolgens wordt aangetoond dat de blokjes in de geassembleerde patronen gebruikt kunnen worden als startpunt om lokaal verscheidene materialen aan te brengen, wederom in oplossing. Ter demonstratie worden gebogen kristallen gemaakt door Ag of Au over Ag-blokjes te laten groeien. Deze kristallen kunnen worden gebruikt om fundamentele vragen te onderzoeken. Daarnaast worden assemblages van kubussen, door middel van Ag-overgroei, ook omgezet in een monokristallijn patroon, bestaande uit een netwerk van elkaar kruisende, periodieke lijnen. Verder wordt geïllustreerd dat een dergelijk netwerk kan werken als een transparante elektrode. Deze kleine demonstratie kan met specifieke optimalisaties worden ontwikkeld tot verreikende technologische toepassingen.

Processen die van minder parameters afhankelijk zijn, zouden gemakkelijker kunnen zijn voor technologische commerciële vertalingen met hoge doorvoer. De patroonvorming en de lokale overgroeiing zijn grotendeels onafhankelijk van het onderliggende substraat. Ook wordt het samenvoegen van Ag- of Pd-kubussen gedemonstreerd bij KT. Tegelijkertijd verbruikt het hele proces heel weinig inkt. Het is dus inderdaad mogelijk om kristallen met met fijne patronen bij KT, op een goedkopere manier en op verschillende substraten, waaronder flexibele en thermisch gevoelige

substraten, te fabriceren. Niettemin, om een volledig werkend apparaat te maken, is het naast patroonvorming even belangrijk om hoogwaardige, holtevrije en grote ononderbroken lagen van verschillende materialen te maken, bijvoorbeeld diëlektrica of halfgeleiders.

Met dit doel voor ogen, beschrijft hoofdstuk 5 een manier om halfgeleider monolagen van perovskiet nanokubussen op KT te maken door eenvoudig opdruppelen. 10 nm $CsPbBr_3$-kubussen gedispergeerd in tolueen worden gebruikt om compacte en continue monolagen te assembleren met een perfecte zij-aan-zij aansluiting. AFM-scans laten zien dat de laag erg glad is, met een gemiddelde oppervlakteruwheid van slechts 4 Å. Liganduitwisseling wordt gebruikt om koolwaterstofliganden met een lange keten (18 koolstofatomen) gedeeltelijk te vervangen door korte thiocyanaten. Het helpt om de aantrekkingskracht tussen de deeltjes af te stemmen, wat wordt onderschreven door ondersteunende simulaties.

Uiteindelijk, met dit hoge niveau van controle, zou de ideale droom zijn om op het oppervlak te beginnen en complexe 3D en mogelijk volledig monokristallijne structuren / apparaten te construeren die vanuit de oplossing worden ontwikkeld. De hoge kwaliteit van de gefabriceerde kristallen maakt ultrahoge efficiëntie voor technologische toepassingen mogelijk. Het kan ook worden gebruikt voor fundamentele studies. In dit proefschrift worden de noodzakelijke stappen in delen gedemonstreerd. Een vervolg zou nu zijn om alle stappen te combineren in een enkel monokristallijn functioneel apparaat. Het gebruik van kubussen kleiner dan 75 nm maakt nog hogere resolutie en kleinere / compacte apparaten mogelijk. Het centrale thema van dit proefschrift is de bottom-up assemblage van monokristallijne nanokubussen om nanostructuren te bouwen. Het idee om nanokubussen te gebruiken als bouwstenen is equivalent aan het gebruik van atomen voor het bouwen van een rooster. De literatuur suggereert dat er al enorme vooruitgang is geboekt, maar er is meer werk nodig om meer controle te verkrijgen en materie op nanoschaal te programmeren voor nuttige doeleinden. Ik hoop dat dit werk wat inzichten kan bieden en ons in ieder geval een stap dichter bij het realiseren van dat doel brengt.

PICTURE GALLERY

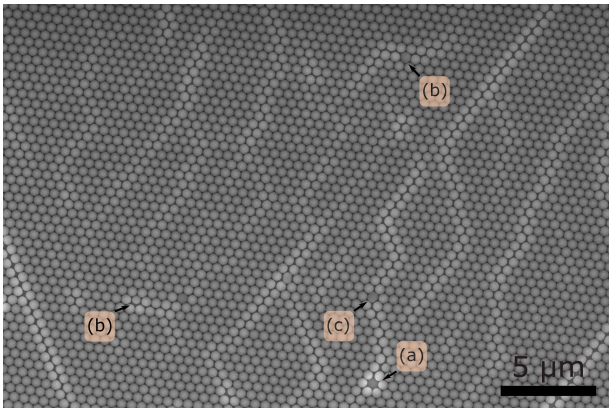

Close-packed monolayer of 500 nm polystyrene beads. Defects caused due to (a) vacancy, (b) particle size or (c) shape dispersion.

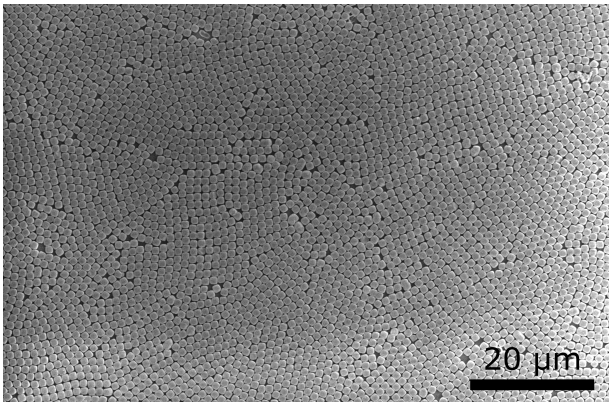

Convective assembly of hollow SiO_2 cubes. Cubes courtesy: Janne-Mieke Meijer.

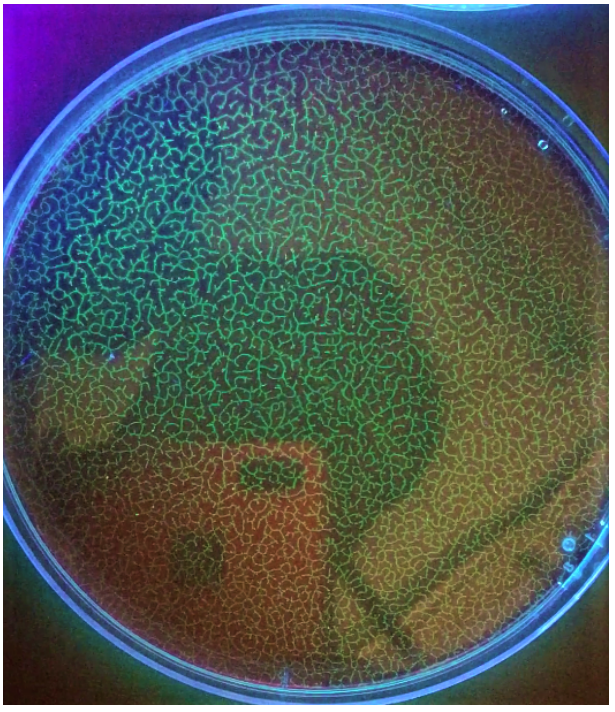

$CsPbBr_3$ cubes suspended on the water surface in a Petri dish.

PUBLICATIONS

This thesis is based on the following publications:

1. Harshal Agrawal, Erik C. Garnett, *Nanocube Imprint Lithography*, ACS Nano, 14, 11009-11016, 2020. (**Chapter 2**)

2. Harshal Agrawal, Biplab K. Patra, Thomas Altantzis, Annick De Backer, Erik C. Garnett, *Quantifying Strain and Dislocation Density at Nanocube Interfaces after Assembly and Epitaxy*, ACS Appl. Mater. Interfaces, 12, 8788-8794, 2020. (**Chapter 3**)

3. Harshal Agrawal *et.al.*, *Solution Overgrown Patterned Crystals: From the Fundamental and Technological Angle.* (**Chapter 4**, manuscript under preparation)

4. Biplab K. Patra*, Harshal Agrawal*, Jian-Yao Zheng, Xun Zha, Alex Travesset, Erik C. Garnett, *Close-packed Ultra-smooth Self-assembled Monolayers of $CsPbBr_3$ Perovskite Nanocubes*, ACS Appl. Mater. Interfaces, 12, 31764-31769, 2020. (**Chapter 5**, *equal contribution)

Other publications by the author:

- *Using Hot-electrons and Hot-holes for Simultaneous Cocatalyst Deposition on Plasmonic Nanostructures*, Evgenia Kontoleta, Alexandra Tsoukala, Sven Askes, Erwin Zoethout, Eitan Oksenberg, Harshal Agrawal, Erik C. Garnett, ACS Appl. Mater. Interfaces, 12, 35986-35994, 2020.

- *Phase-resolved Surface Plasmon Scattering Probed by Cathodoluminescence Holography*, Nick Schilder, Harshal Agrawal, Erik C. Garnett, Albert Polman, ACS Photonics, 7, 1476-1482, 2020.

- *Spatial Resolution of Coherent Cathodoluminescence Super-Resolution Microscopy*, Joris Schefold, Sophie Meuret, Nick Schilder, Toon Coenen, Harshal Agrawal, Erik C. Garnett, Albert Polman, ACS Photonics, 6, 1067-1072, 2019.

- *In situ Age Hardening and Grain Refinement in As-sprayed Al-Sc Binary Alloy Deposits*, Nadimpalli Raghukiran, Ravindran Sujith, Harshal Agrawal, Rajashekhara Shabadi, Ravi Kumar, Journal of Alloys and Compounds, 735, 1596-1602, 2018.

- *Evaluation of Self-Healing Behaviour of AISI 304 Stainless Steel*, Harshal Agrawal, Pranshu Sharma, Piyush Tiwari, R. V. Taiwade, R. K. Dayal, Trans Indian Inst Met, 68, 501-511, 2015.

- *Directional Emission of Quantum Dots Soft-stamped on Si Mie Resonators*, Tom Veeken, Benjamin Daiber, Harshal Agrawal, Mark Aarts, Esther Alarcón Lladó, Erik C. Garnett, Bruno Ehrler, Albert Polman. (under preparation)

ACKNOWLEDGEMENTS

AMOLF is an excellent place to pursue a Ph.D. It resonates with vibrant and positive energy. It provides a setting where internationals like me can get adjusted within no time. It is equipped with a wonderful design department, a high-tech workshop and equally skilled staff, and an efficient ICT department. The offices and desks are always tidy because of the dedication of the well-organized facilities personnel. We also have a flexible purchase and finance division along with a cheerful human resource team. The cheery on the cake is the army of expert technicians always available for help. All these fringe benefits permit the researcher to focus on research and make our life very pleasant and comfortable during our term at AMOLF. Besides, one can listen to eminent researchers and interact with them regularly merely by being part of the public colloquium and student slots. I am genuinely grateful to have experienced such an ecosystem. When I am writing this part, I am trying to relive all the four years in my mind within the span of an hour. It gives me a rapid rush of excitement with the memories that are forever etched in my mind.

It was possible to become part of AMOLF because Erik gave me an opportunity to work on his VIDI proposal. I want to thank him for trusting and guiding me during my Ph.D. I am grateful for all the feedback you gave while colloquiums, group meetings, and writing manuscripts. Thanks for all the group outings, short funny anecdotes - be it from your Ph.D., grant interview, family vacation, or about cooking lentils. Things that I admire about you are your openness to criticism, love for science, optimism, and a strong will of learning. You have a lot of knowledge and experience about nanofabrication and know a great deal about photonics; it is impressive as well as encouraging. One thing that stands out for me is that you were always available to discuss. I could simply walk to your office and you would put an instant pause to your things and start talking with a smile on your face. I have always enjoyed the liberty of free and open communication with you. Please keep it up with all the following group members. I valued your supervision and would carry forward all the lessons learnt here in our Nanoscale Solar Cells group. I look forward to following the group updates and let's keep in touch.

All this is complemented well by the wonderful group members. I want to acknowledge all the present and previous group members. Thanks, Marc, for being so instrumental in the chemical lab and all the stories you told about AMOLF during our lunch breaks and the table tennis matches. I will miss them. Thanks, Jian-Yao, for sharing all the valuable suggestions, papers you come across, stories from Ireland, and saying words of motivation whenever I needed them. Thanks, Forrest, for all the

interesting discussions during your wild card visits at AMOLF. Thanks, Eitan, for the fun times during the trip to Boston and working together on different projects. I am sure you will bring them to nice logical ends. Thanks, Hongyu, for all the intriguing discussions we had in our office on China or India or B-plans. Thanks, Sven, for being the gym partner and fun-filled chatter all the time. Thanks, Julia, for helping with the transmission measurements and translating the summary of the thesis. Thanks, Susan, for all the fun times as the office mate and during our 'TT' sessions. Thanks, Matthijs, for sharing your game collection with me. Thank Mateo, Roxy, Donal for the snacks and cheerful jokes in the office and during coffee. Sarah and Jeroen, you both made the office a fun place for me. I would certainly miss all the jokes and laughing all the time. Thanks to all the other members for your feedback, discussion, and pleasant times during lunch, coffee breaks, outings, etc. I would like to acknowledge the contributions from Beniamino for setting the project of nanocube assembly in motion; Biplab and Sudeshna for all the cooking we did together, hilarious stories from your Ph.D., and intense discussion about India, Netherlands, or science.

Although I am guilty of not always being part of it, the coffee culture at 10.45 am is an easy way to get to know existing and new people. It is hard not to think about collaboration when subjected to friendly conditions like at AMOLF. I thank Nick for making me part of his experiments, answering all my annoying questions and humorous conversations we had during borrels. I learnt a lot while optimizing QDs stamping and it was very rewarding, thanks Tom. Moreover, Bas for letting me use your lab for imprinting experiments. Also, outside AMOLF, Sara Bals, Thomas Altantzis, and Annick De Backer for the successful collaboration on HRTEM imaging of Pd cubes; Xun Zha and Alex Travesset for doing all the calculations for the perovskite cubes.

Talking to other group leaders at AMOLF is as easy as talking to your office mate or a friend. I want to thank Albert, Femius, Bruno, Esther, Wim, Ewold, and Said for creating such an open and inviting atmosphere. Surprisingly, I picked up more photonics than I expected during the Nanophotonics colloquium, so kudos to the organizers and speakers for the same.

I want to extend special thanks to the members of the 'Works Council', including Huib and Paula for switching to English every single time for all the meetings. Being part of the international panel, I got a sneak peek behind the scenes. It has allowed me to get a closer look at how the policies are implemented and made me realize a ton of thinking from many people goes into making even the smallest decisions. I hope I was able to play my role in serving the AMOLF community adequately. I also want to thank the members of the Amsterdam Science Magazine for giving me a chance to be a member of the editorial board. It was a great learning experience, and I wish, I should have joined much earlier.

I am sincerely thankful to Wiebe for fixing my outlook issue every time and suggesting his favourite dark songs. Jorijn for writing the software for my capillary assembly setup. Henk-Jan for designing beautiful graphics all the time on short notices and refreshing conversations about India. Ricardo for making fantastic schematics. Jan for helping me with all the work from the workshop. Mark for dicing the wafer, life advice, conversations in Hindi, and suggesting Nepali restaurants. Niels for being

ever ready to help me with Instron and ways to improve my setup. Dion for making the setup for imprinting and useful suggestions. Petra for making me a part of the 'Life at AMOLF' video, discussing the recipe of paneer butter masala, and engaging interactions. Juliette for greeting every single day in the morning with a lovely smile. Ad for taking care of all the missed attendance. Grace for being a good friend. Clyde for telling endless comical stories and all the parties. Hans, Andries (I missed you for the friendly banter we exchanged all the time), Dimitry, Bob, Johan, and Igor for the countless no of times I have called you with questions, and you were almost always available to answer. I am truly indebted to these people who made the journey so smooth in the last four years.

Hans – thanks for all the adventures we did together. That camping trip and the road trip is still fresh in my mind. I am so glad that you are one of my paranymphs and will always cherish the friendship I have with you. Send me a postcard from wherever you go after the Ph.D. Arno – all the movie nights, cooking sessions, museum visits were just incredible. Thanks for helping me with various small things, organize parties, and it would have been so challenging to get by in Amsterdam without you. We should keep in touch. Nikhil - you still have to cook that 'sambhar' for me, thanks for all the friendly interactions and troubleshooting with the thesis. Marco V. – thanks for being so encouraging and gifting me backstreet boys. We should take that trip to Columbia; I am asking you for ages and is still pending. Dominic – thanks for being so lovely and witty all the time. I missed you in the office when you were gone. Ariane – those deep conversations about 'The Magicians', teleportation, and relationships were just mind-blowing. We still have to take a picture together with the T-shirt you designed for both of us. Rahul – thanks for telling me all the laughable stories about TIFR and tea breaks. Somen and Johnefh - the TT matches and following extensive discussion about the shots, spin, and speed is memorable. Mareike – thanks for cooking those Indian dishes and inviting me for dinner. Andrea and Giorgia - thanks for sharing the best pizza places in Amsterdam, teaching me Italian slangs, and many entertaining chitchats in the corridors of AMOLF. Isabelle – I am always amazed by your energy level on the dance floor and enjoyed every bit of the time we danced at the parties and I hope we can do it again. Annemarie – it is so refreshing and energizing talking to you, thanks. Marloes – the trip to GRC with you was a lot of fun. Thanks Deba, Ruslan, Matthias, Nasim, Sangeetha, Silvia, Loreta, Lucie, Christian, Benjamin, Mark, Jorick, Jannis, and Shanti for a remarkable journey in the past years. I am sure that I have missed talking about some folks. This is a drawback of mentioning names; however, I did not want to lose the opportunity to acknowledge those who have made a difference while I was in Amsterdam.

Eventually, I would like to thank my parents and brother for being nothing but supportive in all walks of my life. I feel blessed.

About the Author

Harshal Agrawal was born on the 8^{th} of August, 1991 in the district of Amravati in the state of Maharashtra in India. He holds a Bachelor's degree in Metallurgical and Materials Engineering from the Visvesvaraya National Institute of Technology, Nagpur (India). Later, he moved to Germany to get a Master's degree in Materials Science from the University of Stuttgart. He worked with Prof. Sabine Ludwigs during the master's thesis which was focused on measuring the mobility of a donor-acceptor copolymer by means of organic field-effect transistors. The timeline was continued in Amsterdam at AMOLF pursuing a Ph.D. working with Prof. Erik C. Garnett and the results are presented in this thesis. Harshal likes to play badminton, table tennis, cricket, carrom etc. He also likes to spend his time designing vector graphics, reading about technical gadgets and upcoming tech, YouTubing, watching TV series and movies. He enjoys stand-up comedy, cooking, dancing, karaoke and outings with friends.